

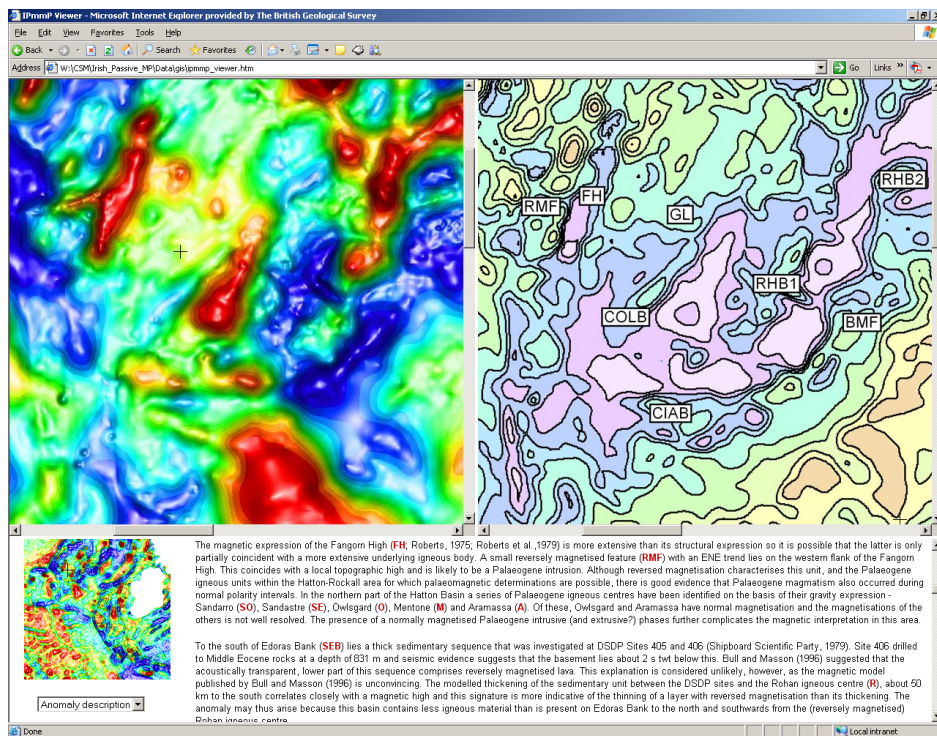


The Irish Passive Margin Modelling Project (IPmmP)

Final Report

ISPSG Project No. IS03/14

BGS Marine, Coastal and Hydrocarbons Programme
Commissioned Report CR/05/102



BRITISH GEOLOGICAL SURVEY

MARINE, COASTAL AND HYDROCARBONS PROGRAMME

COMMISSIONED REPORT CR/05/102

The Irish Passive Margin Modelling Project (IPmmP)

Final Report

ISPSG Project No. IS03/14

G S Kimbell, J D Ritchie, A F Henderson

Keywords

Atlantic margin, Ireland, gravity, magnetic, modelling.

Front cover

Screenshot of the IPmmP Viewer

Bibliographical reference

KIMBELL, G S, RITCHIE, J D, AND HENDERSON, A F. 2005. The Irish Passive Margin Modelling Project. Final Report. *British Geological Survey Commissioned Report*, CR/05/102. 95pp.

The copyright of materials produced by the Irish Passive Margins Modelling Project is owned by PIPCo RSG, except where derived from data or information provided by the Department of Communications, Marine and Natural Resources (DCMNR), in which case it is vested in DCMNR. The copyright of materials supplied by the British Geological Survey, and which existed before commencement of the project, is owned by the Natural Environment Research Council (NERC).

Commercial in confidence

PIPICO RSG Ltd Contract No. 01.14.2004

Keyworth, Nottingham British Geological Survey 2005

BRITISH GEOLOGICAL SURVEY

The full range of Survey publications is available from the BGS Sales Desks at Nottingham, Edinburgh and London; see contact details below or shop online at www.geologyshop.com

The London Information Office also maintains a reference collection of BGS publications including maps for consultation.

The Survey publishes an annual catalogue of its maps and other publications; this catalogue is available from any of the BGS Sales Desks.

The British Geological Survey carries out the geological survey of Great Britain and Northern Ireland (the latter as an agency service for the government of Northern Ireland), and of the surrounding continental shelf, as well as its basic research projects. It also undertakes programmes of British technical aid in geology in developing countries as arranged by the Department for International Development and other agencies.

The British Geological Survey is a component body of the Natural Environment Research Council.

British Geological Survey offices

Keyworth, Nottingham NG12 5GG

☎ 0115-936 3241 Fax 0115-936 3488
e-mail: sales@bgs.ac.uk
www.bgs.ac.uk
Shop online at: www.geologyshop.com

Murchison House, West Mains Road, Edinburgh EH9 3LA

☎ 0131-667 1000 Fax 0131-668 2683
e-mail: scotsales@bgs.ac.uk

London Information Office at the Natural History Museum (Earth Galleries), Exhibition Road, South Kensington, London SW7 2DE

☎ 020-7589 4090 Fax 020-7584 8270
☎ 020-7942 5344/45 email: bgs london@bgs.ac.uk

Forde House, Park Five Business Centre, Harrier Way, Sowton, Exeter, Devon EX2 7HU

☎ 01392-445271 Fax 01392-445371

Geological Survey of Northern Ireland, Colby House, Stranmillis Court, Belfast, BT9 5BF

☎ 028-9038 8462 Fax 028-9038 8461

Macleon Building, Crowmarsh Gifford, Wallingford, Oxfordshire OX10 8BB

☎ 01491-838800 Fax 01491-692345

Sophia House, 28 Cathedral Road, Cardiff, CF11 9LJ

☎ 029-2066 0147 Fax 029-2066 0159

Parent Body

Natural Environment Research Council, Polaris House, North Star Avenue, Swindon, Wiltshire SN2 1EU

☎ 01793-411500 Fax 01793-411501
www.nerc.ac.uk

Contents

Contents.....	i
Summary	vi
1 Introduction	1
2 Geophysical data	1
2.1 Geophysical data sources.....	1
2.2 Geophysical data processing	1
3 Well data	3
4 Structural data sources.....	5
4.1 Structural element maps	5
4.2 Sediment thickness data.....	5
5 GIS development	6
5.1 Overview	6
5.2 ArcMap version	6
5.3 ArcView 3.x version.....	7
5.4 ArcReader version	7
5.5 The IPmmp Viewer	7
6 Rock properties	8
6.1 Introduction	8
6.2 Densities	8
6.3 Velocities.....	8
6.4 An attempt to quantify denudation	9
6.5 Volcanic units	11
7 Model construction.....	11
7.1 Introduction	11
7.2 Thermal effects	12
7.3 Initial model for the cover sequence.....	13
7.4 Construction of an optimised 3D model.....	15
7.5 Flexural modelling.....	16
7.6 Magnetic modelling.....	16
8 Discussion of the modelling results.....	17
8.1 Regional setting	17
8.2 Overview of the optimised 3D model.....	17
8.3 Flexural modelling.....	20
8.4 Magnetic modelling.....	22
8.5 A review of model features	23

9	Conclusions and recommendations	30
Appendix 1	Geophysical images.....	31
Appendix 2	Base data and structural data within the GIS	33
Appendix 3	Model data within the GIS.....	34
Appendix 4	Velocity-depth relationships	36
Appendix 5	Alphabetical list of model features.....	39
References	41

FIGURES

Figure 1	The Irish Passive Margin Modelling Project (IPmmP) study area, showing the locations of the structural element maps of Naylor et al. (1999, 2002), and the approximate extensions of the main basins outside the areas covered by these maps (black dashed lines). Red line indicates the Irish Designated Area.....	46
Figure 2	Colour shaded-relief image of the free-air gravity anomaly. Equal colour area; illumination from the north.....	47
Figure 3	Colour shaded-relief image of the isostatically-corrected Bouguer gravity anomaly. Equal colour area; illumination from the north.	48
Figure 4	Colour shaded-relief image of the total magnetic field. Equal colour area; illumination from the north.	49
Figure 5	Topographic map of the IPmmP study area.....	50
Figure 6	Colour shaded-relief topographic image. Illumination is from the north.....	51
Figure 7	The IPmmP Viewer in (a) list mode, and (b) text mode.....	52
Figure 8	Density logs from wells west of Ireland. The red curve is the normal compaction curve for shale of Sclater and Christie (1980). Depths are relative to sea bed.....	53
Figure 9	Density logs from wells south of Ireland. The red curve is the normal compaction curve for shale of Sclater and Christie (1980). Depths are relative to sea bed.....	54
Figure 10	Comparison of an empirical velocity depth curve with wireline density logs and velocity models from wide-angle experiments in the Rockall Basin.	55
Figure 11	Velocity logs from wells west of Ireland. The red curve is the empirical (normal compaction) curve shown in Figure 10 and discussed in the text. Depths are relative to sea bed.	56
Figure 12	Velocity logs from wells south of Ireland. The red curve is the empirical (normal compaction) curve shown in Figure 8 and discussed in the text. Depths are relative to sea bed.	57
Figure 13	Simple model of thermal contrasts across a continent-ocean boundary 55 Ma and 105 Ma after ocean opening. Temperature contours at 100°C intervals. The continent-ocean boundary is at 500 km and the oceanic lithosphere lies to the left of this.....	58
Figure 14	Age of ocean crust assumed in the thermal modelling (after Müller et al. 1997). Thick purple line is the interpreted continent-ocean boundary.	59
Figure 15	Thickness of Cenozoic (post-lava) sedimentary rocks assumed in the initial model.	60
Figure 16	Thickness of lava in the Hatton-Rockall area assumed in the initial model.....	61
Figure 17	Variation in the denudation of pre-Cenozoic sedimentary rocks assumed when calculating the effect of overcompaction on the density of these rocks.....	62
Figure 18	Thickness of pre-Cenozoic sedimentary rocks assumed in the initial model.	63
Figure 19	Thickness of pre-Cenozoic sedimentary rocks after model optimisation (continental areas).....	64
Figure 20	Total cover sequence thickness in the optimised model.....	65
Figure 21	Thickness of crystalline crust in the optimised model.....	66
Figure 22	Depth to Moho in the optimised model.	67

Figure 23	Colour shaded-relief image of the computed free-air gravity anomaly over the optimised model. The imaging parameters are identical to those used in the display of the observed field in Figure 2. Computed values have been shifted by +15 mGal to allow for background field assumed during model optimisation.....	68
Figure 24	Residual gravity anomaly over the optimised model.....	69
Figure 25	Load anomaly of the optimised model.	70
Figure 26	Apparent extension factor of the optimised model. Note that extreme values can arise because of instability in the gravity inversion (see Section 8.2.2 and Figure 30).....	71
Figure 27	Cross-section through the optimised model along the RAPIDS 32 profile (upper panel). The lower panel shows the main interfaces from the 3D model (sedimentary and Moho) superimposed on the velocity model for this profile of Mackenzie et al. (2002a). ...	72
Figure 28	Cross-section through the optimised model along the RAPIDS 33 profile (upper panel). The lower panel shows the main interfaces from the 3D model (sedimentary and Moho) superimposed on the velocity model for this profile of Mackenzie et al. (2002a). ...	73
Figure 29	Cross-section through the optimised model along the RAPIDS 34 profile (upper panel). The lower panel shows the main interfaces from the 3D model (sedimentary and Moho) superimposed on the velocity model for this profile of Mackenzie et al. (2002a). ...	74
Figure 30	Cross-section through the optimised model along the RAPIDS 1/2 (Transverse) profile (upper panel). The lower panel shows the main interfaces from the 3D model (cover sequence and Moho) in red superimposed on the RAPIDS interpretation of Vogt et al. (1998; western part) and O'Reilly et al (1998; eastern part). The lower sedimentary layer of O'Reilly et al. (1998) is shaded.	75
Figure 31	Comparison of computed gravity field over flexural models based on the initial cover sequence model and different assumptions about the strength of the lithosphere. Indicated values of effective elastic thickness are assumed throughout the deposition of the cover sequence.....	76
Figure 32	Load anomalies over the optimised model compared with those over the flexural models testing the influence of lithospheric strength during deposition of the cover sequence (Figure 31).	77
Figure 33	Comparison of observed free-air gravity anomalies with computed fields over flexural models based on the initial cover sequence model. The effective elastic thickness indicated was assumed to apply during deposition of the Cenozoic (post-lava) sedimentary rocks, and the lithosphere was assumed to be weak prior to this. Display parameters as in Figure 2.....	78
Figure 34	Load anomalies over the optimised model compared with those over the flexural models testing the influence of lithospheric strength during Cenozoic sedimentary loading (Figure 33).	79
Figure 35	Computed magnetic field over the optimised model assuming the crystalline basement has a uniform induced magnetisation of 1 A/m and the lavas in the Hatton-Rockall area a reversed magnetisation of 3 A/m. The imaging parameters are identical to those used in the display of the observed field in Figure 4.	80
Figure 36	Computed magnetic field over the initial model assuming the crystalline basement has a uniform induced magnetisation of 1 A/m and the lavas in the Hatton-Rockall area a reversed magnetisation of 3 A/m. Model based on initial cover sequence model and crustal thickness based on local isostasy. The imaging parameters are identical to those used in the display of the observed field in Figure 4.	81

Figure 37 Colour shaded-relief image of free-air gravity anomalies over the north-east Atlantic region. The black rectangle is the IPmmP study area. An IPmmP image has been superimposed on an image based on BGS and open-file data (colour scales differ). Illumination is from the north. White lines are the lineaments of Kimbell et al. (2005): ADL = Anton Dohrn lineament zone; SHL = South Hatton Lineament. 82

Figure 38 Colour shaded-relief image of total field magnetic anomalies over the north-east Atlantic region. An IPmmP image has been superimposed on an image based on BGS and open-file data (colour scales differ). Illumination is from the north. The black rectangle is the IPmmP study area. White lines are the lineaments of Kimbell et al. (2005): ADL = Anton Dohrn lineament zone; SHL = South Hatton Lineament. The purple line (IS) is the Iapetus Suture, based on the interpretation of Kimbell and Quirk (1999) in the east, and extended westwards on the basis of the magnetic anomaly pattern..... 83

Figure 39 Annotated features superimposed on the total cover sequence thickness model (see text for details)..... 84

TABLES

Table 1 Wells used in the Irish Passive Margin Modelling Project..... 3

Table 2 Nominal denudation estimates based on differences between log data and assumed normal compaction trends. Log sections less than 50 m in length have been omitted..... 10

Table 3 Average density and velocity from wireline logs through volcanic sequences in ODP boreholes 642E (Vøring margin) and 917A (East Greenland margin)..... 11

Summary

This report describes the Irish Passive Margin Modelling Project (IPmmP), a regional modelling study commissioned by the Irish Shelf Petroleum Studies Group (ISPSG). A range of data sources was assembled for the project, including gravity, magnetic and topographic grids, digital wireline logs and existing interpretations of sediment thickness variations across the region. A project GIS has been constructed and populated with geophysical images, cultural and structural data and the results of the modelling. The GIS is provided in a range of formats to ensure that it can be accessed by all the ISPSG members. An interface has been developed which supplements normal GIS functionality by allowing detailed correlation between different user-defined images in a 'side-by-side' viewer.

Analysis of the wireline log data provides evidence of the influence of uplift and denudation on rock densities and velocities within the cover sequence, and this was incorporated into the modelling by sub-dividing the cover sequence into Cenozoic and pre-Cenozoic components and adopting a different velocity and density models for each. The Cenozoic sequence was split into a normally-compacted sedimentary unit and a volcanic unit, with the latter only covering the Hatton-Rockall area and having a very simplified geometry. Properties within the pre-Cenozoic unit were based on the assumed normal compaction curve offset by a nominal depth at each model grid node to represent the overcompaction resulting from uplift and erosion. Initial structural models were constructed for each cover sequence component from the available structural data, with structure maps that were only available in two-way time converted to depth using the above scheme.

The initial model for the thickness and density of the cover sequence was incorporated into an isostatic model that included estimates of the effect on upper mantle densities of lateral heat transfer between the continental and oceanic upper mantle. The thickness of the crystalline crust and sedimentary layer were modified to improve the match between calculated and observed gravity anomalies. The resulting optimised model typically predicts Moho depths to within about 2 km of those estimated by deep seismic experiments. There is some evidence that Moho depths are overestimated adjacent to the Hatton Margin and underestimated in the south of the study area, which could reflect the influence of lateral changes in the upper mantle not incorporated in the model, although this needs to be kept under review as more deep seismic control becomes available.

Flexural modelling was used to investigate how the strength of the lithosphere has influenced the evolution of the sedimentary basins in the study area. Overall, the results confirm the generally weak nature of the lithosphere, as inferred by previous authors, but they do provide evidence of finite strength during more recent sediment loading in the Rockall and Porcupine basins. Flexural backstripping using the available structural data indicates that the observations over the Porcupine Basin cannot be explained simply by lithospheric strength during sediment loading in the Cenozoic, and it is inferred that the strength developed throughout the 'sag' phase following Late Jurassic – Early Cretaceous rifting. The averaged effective elastic thickness in these basins is difficult to quantify accurately, because the current structural model does not include an interface at the appropriate (c. base Cretaceous) level, but values of the order of 10 km appear appropriate.

Three-dimensional magnetic modelling, based on the geometries defined by gravity modelling, indicates that the broad magnetic anomaly pattern over the Rockall and Porcupine basins can be explained by the thinning of relatively magnetic crystalline crust beneath these basins. To the north of the area influenced by the Barra Volcanic Ridge System the subtle magnetic anomalies observed over the Rockall Basin are well replicated by the magnetic field computed from the 3D model. The observed magnetic anomalies over the Hatton Basin are, however, far more intense

than those generated by the forward magnetic modelling. This is because of the multiple magnetic sources in this region including both reversely and normally magnetised Palaeogene igneous units, magnetic crystalline basement and (possibly) igneous rocks associated with the Cretaceous event responsible for the Barra Volcanic Ridge System.

The model optimisation process has led to relatively detailed predictions for the geometries for many basins on the Irish margin for which there was only limited previous information. A pre-Cenozoic component for the Hatton Basin is predicted which is characterised by a series of broadly NE-trending depocentres offset by transfer structures. The modelling results over this basin may well be distorted as a result of inaccuracies in defining the shallower structure, particularly the top and base of the Palaeogene lavas, but the available seismic data also suggest rapid variations in the thickness of the basal unit of the cover sequence. Several basins are identified on the Rockall High which have not been detected by previous seismic surveys, presumably because of the masking effects of overlying lavas, and in other cases (e.g. the Conall and Ciarán basins) insights are provided into the geometries of basins that had been proved seismically but with only very limited lateral control. On the Porcupine High, basins are resolved which appear to have been controlled by extensions of the Fairhead – Clew Bay lineament and splays of the Great Glen Fault. The models highlight the strongly linear nature of the structures controlling the Erris and Slyne basins, and the distinct difference between the trends of these. A pattern of faulting at the margins of the Porcupine Basin is resolved by the gravity modelling which compares well with regional interpretations based on seismic data. A component of the Porcupine Volcanic Ridge System in the southern part of the basin can be traced for about 130 km using magnetic data, and correlates with a step in the thickness of the basin fill predicted by the gravity model. An ENE-trending lineament is detected in the Goban Spur area which has a strong influence on the forms of the Pendragon, Shackleton and Merlin basins. The linear trends of the basins to the south and east of Ireland are interpreted to have been inherited from a basement fabric that was initially established during the late Precambrian assembly of this basement and subsequently subjected to Caledonian and Variscan reactivation.

1 Introduction

The Irish Passive Margin Modelling Project (IPmmP) was commissioned by the Irish Shelf Petroleum Studies Group (ISPSG) in the summer of 2004 and has been conducted by the British Geological Survey (BGS). In outline, the project aimed to combine BGS methodologies and expertise in regional three-dimensional modelling with new data compilations, including results from the Irish National Seabed Survey, to produce enhanced models for the three-dimensional lithospheric structure beneath the Irish Continental Shelf.

The project study area is a rectangle embracing the Irish Designated Area, as shown in Figure 1. The bounding coordinates (UTM Zone 28) are:

-150000 – 1170000 mE; 5150000 – 6420000 mN

This report describes the work undertaken by the project and presents the results. The primary means for interrogating these results, however, is provided by the GIS and web browser interfaces developed for the project.

Key reference works for this study have been the structural nomenclature volumes for the Irish Rockall Basin and Porcupine-Goban regions published by the Petroleum Affairs Division (Naylor et al., 1999, 2002; see Figure 1 for locations). Users are directed to these publications for the definitions and descriptions of bathymetric and geological features referred to in this report. The structural element maps contained in these volumes are included in digital form in the IPmmP GIS.

2 Geophysical data

2.1 GEOPHYSICAL DATA SOURCES

The main geophysical data sources for this project were gravity, magnetic and topographic grids provided by the Geological Survey of Ireland (GSI) and Petroleum Affairs Division (PAD). Both of these organisations lie within the responsibility of the Irish Department of Communications, Marine and Natural Resources (DCMNR), and the grids were provided for the this project under the terms of an agreement with that department. The grids are based on the following data sources:

- (i) GSI gravity, magnetic and bathymetric data from the Irish National Seabed Survey (Zone 3)
- (ii) PAD gravity, magnetic and bathymetric compilations based on released survey data
- (iii) Satellite-derived gravity data (Sandwell and Smith, 1997)
- (iv) The GAMMA5 regional magnetic compilation (Verhoef et al., 1996)
- (v) Bathymetric contour data from the GEBCO Digital Atlas (IOC, IHO and BODC, 2003)

2.2 GEOPHYSICAL DATA PROCESSING

2.2.1 Coordinate systems

It was agreed at an initial start-up meeting that the project would employ Zone 28 of the Universal Transverse Mercator coordinate system and the European Datum 1950. The projection details are thus:

Projection:	Transverse Mercator
Spheroid:	International 1909 (or 1924)
Central Meridian:	15°W
Reference latitude:	Equator
Scale factor:	0.9996
Units :	metres
False easting:	500000
False northing:	0.0
Datum:	European Datum 1950 (ED50)

The ED50 datum was chosen because key exploration data (e.g. exploration wells) in Irish waters are currently referenced to this datum. It should be noted, however, that the WGS84 datum is increasingly used in offshore exploration and that points which have the same geographic coordinates but are referred to these different datums differ in their position on the Earth. Within the IPmmP study area the eastings and northings both differ by 90 – 140 m (the differences increasing to the south and west).

2.2.2 Gravity data processing

The gravity compilation was originally undertaken by ARK Geophysics Ltd. for the PAD in 2003, and was supplied as grids of free-air gravity anomaly (Figure 2) and simple Bouguer gravity anomaly for the offshore areas. The grid node spacing is 1 km. The Bouguer correction was calculated using a density of 2.20 Mg/m³, and employing water depths computed by interpolating the GEBCO bathymetry onto the gravity data point locations (M Croft, ARK Geophysics Ltd., personal communication).

Isostatically-corrected Bouguer gravity anomalies have been calculated for this project by 3D gravity modelling using the Gmod program (Dabek and Williamson, 1999). The isostatic component of the correction was calculated assuming a Moho with a reference depth of 30 km and a density contrast of 0.4 Mg/m³. Lee (1996) has illustrated how it is more appropriate to calculate the Bouguer component of the correction using a density representative of the crystalline upper crust rather than of the sediments close to the sea bed. This is because the latter approach generates large negative gravity anomalies over deep water troughs by, in effect, simulating a sedimentary basin with the same geometry as the water mass. The problem with using a basement density for the Bouguer correction is that the gravity effect of short-wavelength topographic features within low-density rocks at the sea bed will be over-corrected. In an attempt to address both these issues, the topography was separated into long and short wavelength components and the Bouguer correction calculated using different densities for each component (2.75 Mg/m³ and 1.8 Mg/m³ respectively). This significantly reduces short-wavelength noise, although there is still evidence of artefacts, for example along the eastern edge of the Porcupine Seabight and over the continental slope in the south-east of the study area (Figure 3). These artefacts appear to arise because the sea-bed topography in such areas is much better sampled than the gravity field.

Further processing of the gravity data involved separation of regional and residual components (by upward continuation) and computation of the scalar horizontal gradient. It was necessary to interpolate the gravity field across the data gaps in onshore areas when undertaking transformations such as upward continuation which involve computations in the wavenumber domain. This was done using a gravity field derived from the EGM96 (Earth Gravity Model 1996) coefficients rather than by simple interpolation.

2.2.3 Magnetic data processing

The magnetic data compilation was also undertaken by ARK Geophysics Ltd. for the PAD and was supplied as a grid of total field magnetic anomalies with a node spacing of 1 km (Figure 4).

Further processing included reduction to pole, regional-residual separation by upward continuation, transformation to pseudogravity, and computation of scalar horizontal gradients of both the total field and pseudogravity. For the purposes of these transformations, the Earth's magnetic field was assumed to have a declination of -10° and inclination of $+67^{\circ}$.

2.2.4 Bathymetric data processing

A topographic/bathymetric grid of the region (Figures 5 and 6) was provided by PAD in the ESRI raster export format. This was in decimal degrees (lon-lat), and was converted to UTM coordinates and re-gridded onto the nodes used in the gravity and magnetic compilations using GMT (Generic Mapping Tools; Wessel and Smith, 1991) routines.

2.2.5 Image generation

A series of digital images has been generated from the new data compilations, and are included in the project's digital deliverables (in the folder 'gis\geophys_images'), where they are accompanied by the supplementary files necessary to ensure that they are correctly georeferenced when displayed in a GIS (see Section 5). The images that are currently available are listed in Appendix 1. They were generated using the BGS COLMAP program and are in JPEG format. Examples of the images are provided in Figures 2 to 6, although a GIS interface should be used to examine the full detail that they contain.

In most cases, no smoothing was applied to the data grids prior to image generation. This means that there are clear changes in resolution across the study area depending on the sampling provided by different surveys. There is also some evidence of artefacts, such as the distinct 'grain' in topographic images that parallels the survey lines of parts of the Irish National Seabed Survey (e.g. in the Rockall Trough; Figure 6). It was considered advisable not to attempt to suppress such features, because this would inevitably lead to some loss of resolution of genuine short-wavelength variations. There is also a danger that an artefact that has been incompletely suppressed will be more difficult to distinguish from a real feature.

3 Well data

The Petroleum Affairs Division supplied data for the wells listed in Table 1 in the form of scanned well composites and digital gamma, sonic, density and calliper wireline logs.

Table 1 Wells used in the Irish Passive Margin Modelling Project

Well	Area	Latitude (degrees)	Longitude (degrees)	TD (m below KB)	Water depth (m)
12/13-1A	Erris Basin	55.6177	-9.5106	2869	480
13/3-1	Donegal Basin	55.8885	-8.5023	1366	131
18/20-1	Slyne Basin	54.3475	-11.0931	4372	354
19/5-1	Erris Basin	54.9617	-10.0334	2584	116
26/22-1A	Porcupine Basin	53.2270	-12.7080	2573	344
26/28-1	Porcupine Basin	53.0414	-12.5588	3315	400
26/28-3	Porcupine Basin	53.0708	-12.5241	2588	364
27/5-1	Slyne Basin	53.9194	-11.1077	1910	201

Well	Area	Latitude (degrees)	Longitude (degrees)	TD (m below KB)	Water depth (m)
27/13-1A	Slyne Basin	53.5574	-11.4103	2725	191
34/15-1	Porcupine Basin	52.5754	-13.1228	4446	482
35/8-2	Porcupine Basin	52.7749	-12.4652	4633	422
35/15-1	Porcupine Basin	52.5817	-12.1122	3687	311
35/19-1	Porcupine Basin	52.4379	-12.2796	5550	479
35/30-1	Porcupine Basin	52.0947	-12.1227	5215	700
36/16-1A	Porcupine Basin	52.4770	-11.9384	2747	250
43/13-1	Porcupine Basin	51.5050	-13.4025	5128	921
48/19-1A	North Celtic Sea Basin	51.4231	-8.3362	3685	88
48/25-1	North Celtic Sea Basin	51.3153	-8.0555	3335	94
49/19-1	North Celtic Sea Basin	51.3814	-7.3639	3603	87
49/29-1	South Celtic Sea Basin	51.0736	-7.3256	3201	97
55/30-1	Fastnet Basin	50.1527	-10.0984	2800	130
56/14-1A	North Celtic Sea Basin	50.5852	-9.2577	2827	105
56/18-1	North Celtic Sea Basin	50.3713	-9.4783	3649	135
56/20-1	North Celtic Sea Basin	50.4852	-9.1876	2417	129
56/22-1	Fastnet Basin	50.1857	-9.6361	2275	115
57/2-1	North Celtic Sea Basin	50.9081	-8.7007	3800	114
58/3-1	South Celtic Sea Basin	50.8963	-7.5862	2859	101
62/7-1	Goban Spur	49.6673	-11.7630	4672	993
63/10-1	Fastnet Basin	49.7625	-10.1711	3447	143

In addition, reference has been made to the results of investigations conducted by the Deep Sea Drilling Programme (DSDP) and Ocean Drilling Programme (ODP). These were accessed via the following websites:

www-odp.tamu.edu/publications (*reports*)
www.ldeo.columbia.edu/BRG/ODP (*wireline logging*)
www-odp.tamu.edu/database (*ODP core sample measurements*)
www.ngdc.noaa.gov/mgg/geology/dsdp/dsdpcdv2.htm (*DSDP sample measurements*)

4 Structural data sources

4.1 STRUCTURAL ELEMENT MAPS

The structural nomenclature publications for the Irish Rockall Basin (Naylor et al., 1999) and Porcupine-Goban region (Naylor et al., 2002) provide the structural framework for a significant proportion of the study area. Postscript versions of the structural element maps contained within these publications were converted to raster format and georeferenced for inclusion in the project GIS. The lon-lat graticule displayed on the maps was used for this purpose, because there were discrepancies between the UTM grid ticks on the two maps (the ticks on the Porcupine-Goban map appear to be in error).

4.2 SEDIMENT THICKNESS DATA

A number of data sources were compiled in order to construct an initial cover sequence model for the study area. These are based on well and seismic data in order to provide a structural input that is independent of the gravity inversion. It would not be possible to generate sensible estimates of sedimentary thickness from the gravity data alone without the initial guidance provided by such input. The physical property analysis (Section 6) suggests that the regional density structure of the cover sequence can be better represented if it is divided into Cenozoic and pre-Cenozoic components, so this is what was attempted. The following data sources were consulted:

1. Composite logs from the wells listed in Table 1.
2. Digitised thicknesses in two-way time (TWT) derived from geological cross-sections in enclosures within the structural nomenclature reports for the Irish Rockall Basin region (Naylor et al., 1999) and Porcupine-Goban region (Naylor et al., 2002).
3. Digitised contours (in depth and TWT) from the Rockall and Porcupine basins based on unpublished maps supplied by PAD.
4. Models for the structure of the cover sequence beneath the Rockall Basin derived from wide-angle data (Joppen and White, 1990; Hauser et al. 1995; Shannon et al., 1999; Mackenzie et al., 2002a, b).
5. Digitised contours of total sediment thickness from the North Atlantic geophysical atlas of Srivastava et al. (1988).
6. Contours of depth to acoustic basement in the Hatton-Rockall area from Roberts et al. (1979; their fig. 8).
7. Digitised contours of total sediment thickness within the Goban Spur area (Masson et al., 1985).
8. Digitised contours of total sediment thickness within the Celtic Sea basins area (Tucker and Arter, 1987).
9. Structural grids for the Rockall Basin donated by one of the ISPSG members.
10. Grids of total sediment thickness over the North Atlantic region generated by Loudon et al. (2004) and made available via an FTP server.
11. Various published seismic cross-sections (in TWT) and other data from the Peel, Kish Bank, Central Irish Sea, St Georges Channel, North Celtic Sea, Rockall, Slyne and Erris basins (e.g. Croker, 1995; Dancer et al., 1999; Dunford et al., 2001; Chapman et al., 1999; Floodpage et al., 2001; Izatt et al., 2001; Murdoch et al., 1995; MacKenzie et al., 2002b)
12. The PESGB (2005) map of the structural framework of the North Sea and Atlantic margin.

13. Data from the western approaches to the English Channel from Evans et al. (1990).
14. Data from the Malin-Hebrides Sea area from Fyfe et al. (1993).
15. Data from the Isle of Man area from Chadwick et al. (2001).

5 GIS development

5.1 OVERVIEW

A Geographic Information System (GIS) provides the primary means of disseminating and interrogating the results of the Irish Passive Margin Modelling Project. In recognition of the fact that different GIS platforms may be in use by different members of ISPSG, the GIS interface is provided in a variety of ESRI formats, as outlined below, including one for a freely available GIS viewer. In each case the GIS should run direct from the CD-ROM, although it is of course possible to transfer the files to another storage device as appropriate. When this is done the whole 'gis' folder should be copied across, without altering the arrangement of the files it contains, in order to ensure that the necessary relative file addresses are maintained.

The layers contained in the GIS are detailed in Appendix 1 (geophysical images), Appendix 2 (base data and structural data), and Appendix 3 (model data). Limited digital metadata are included (geographic information and a brief abstract) and these were generated in ArcCatalog using the ISO stylesheet. All raster sources are in projected co-ordinates (UTM Zone 28, ED50), while the vector sources (shapefiles) are in geographic co-ordinates (ED50) for ease of use in projected views in ArcView 3.x.

The following files are contained within the top level of the gis folder and can be opened within the relevant application (or by double-clicking the file icon).

ipmmp.mxd	For use with ArcMap (Version 8 or higher)
ipmmp.apr	For use with ArcView Version 3.x
ipmmp.pmf	For use with the ArcReader free viewer
ipmmp_viewer.htm	For use with Microsoft Internet Explorer

5.2 ARCMAP VERSION

The IPmmP GIS has been developed using the ArcGIS Desktop system, and the recommended way to access it is using the ArcMap application. The GIS was generated using ArcMap Version 8.3, which should be forward compatible with Version 9, although there may be backward compatibility issues with versions 8.1 and 8.2. One such issue relates to the use of layer (.lyr) files to store legend information relating to the relevant shapefiles. Legends are therefore also included in the previous ArcView legend file format (.avl), which can be read by all versions of the software.

The various components of the GIS are organised in group layers within the table of contents, and these should be expanded in order to access a particular component. There are groups for base data, tectonic data and a series of group layers which organise the geophysical images into categories in order to facilitate navigation between them. Further groups contain the 3D modelling results (initial model components, optimised model, flexural modelling and magnetic modelling). Note that the check-boxes at both the group and individual level need to be ticked in order for an image or shapefile to become visible. The group layers can be reloaded (or loaded into another GIS) using the layer (.lyr) files within the relevant folders (gis\base_data, gis\tectonic, gis\geophys_images, gis\modelling_results).

5.3 ARCVIEW 3.X VERSION

It is recognised that the previous generation of GIS interface (ArcView 3.x) is still used, so a version of the IPmmP GIS in this format is included. The table of contents contains a simple list of file names, so the relevant appendices (1, 2 and 3) need to be referred to in order to obtain more information about the various components. Note that the GIS includes gridded data, so the ArcView Spatial Analyst extension needs to be loaded in order to read it.

5.4 ARCREADER VERSION

ArcReader is a free viewer that is packaged with the ArcGIS system or can be downloaded from the ESRI website (www.esri.com). It allows users to view and explore the map information in much the same way as ArcMap, although other GIS functionality is very limited. The current ArcReader file was generated using the ArcGIS Publisher Extension (Version 8.3).

The installation files for Version 9.0 of ArcReader are included on the accompanying CD-ROM (double-click on `setup.exe` in the ArcReader90 folder). The installation will not proceed if the user has conflicting products installed, and this includes earlier versions of the ArcGIS desktop.

5.5 THE IPMMP VIEWER

The IPmmP Viewer (Figure 7) has been developed to allow different images to be viewed side-by-side rather than on top of each other, as in a conventional GIS. The latter allows correlation between two rasters either by toggling the visibility of the overlying one, or by adjusting its transparency, but both these approaches have their shortcomings. The new viewer retains full visibility of both images and allows detailed correlation by superimposing coincident cross-hairs on both of them (Figure 7a). The viewer is useful, for example, for comparing gravity and magnetic responses, but any combination of images can be selected using the pull-down lists, including structural element maps and results from the 3D modelling. In order to maximise resolution, only a small proportion of the study area is shown in the side-by-side windows, but a separate ‘thumbnail’ image of the whole study area is included to provide an overview. Again, this can be changed using a pull-down list. A cross-hair on the thumbnail traces the position of the cursor as it is moved over the main windows. Navigation around the main windows is either by using their scrollbars or by clicking on the required location in the thumbnail. Windows within the viewer can be resized, depending on the user’s priorities. The two main windows are always registered at their top left corners and clicking on the thumbnail image causes the main windows to scroll such that the target area moves to the centre of the left hand window.

A pull-down list below the thumbnail provides different options for the content of the window on the bottom right-hand side of the viewer. Short and long versions of the image lists are offered, with the former appropriate for rapid inspection using a limited range of displays and the latter suitable for more detailed analysis. A third option displays descriptive text within the viewer (Figure 7b). The text is based on Section 8.5 of this report and is linked dynamically to an annotated image, which can be invoked either by clicking on a link at the top of the text or from within the image lists. If the latter route is used, the annotated image can be displayed in either the left- or right-hand window, but is only fully interactive when placed in the right window. Clicking on a label in the annotated image will scroll the text to a description of that feature; clicking on labels within the text will pan both image windows to the feature under discussion. It is possible to toggle between list and text modes to change the combination of images being viewed.

Use of the ‘refresh’, ‘back’ and ‘forward’ buttons in the web browser with the IPmmP Viewer is not recommended as it can lead to misregistration between the different components of the viewer. Some of the viewer functions dynamically change the content of a window in a way that

cannot be recovered through the browser's history. If necessary there is a link below the lists that can be used to update the images to match the descriptions displayed in the list boxes.

The viewer only works in Internet Explorer (Version 6 or higher). If problems are encountered when starting it up, this may be because of the browser's security settings. Navigate to Tools > Internet Options > Advanced, scroll to 'Security' and make sure that active content is allowed (either from CD or disk, depending on where the IPmmP data are stored).

6 Rock properties

6.1 INTRODUCTION

An analysis of rock physical properties has been undertaken using data from the wells listed in Table 1 and DSDP/ODP data. The primary aim was to investigate the relationship between rock density and depth of burial in order to establish a scheme that can be used for simulating the density of the cover sequence in the gravity models. The effect of depth of burial on rock velocities was also investigated, for comparison with the trends observed in the density data and in order to assist with depth-conversion of two-way travel time data required for the sediment thickness compilation. A limited analysis of rock magnetic properties was also conducted, based on DSDP/ODP data.

The densities and velocities of sedimentary rocks are influenced by both lithology and compaction. If part of a sedimentary sequence has been removed, for example by uplift and erosion, the remaining rocks will not lie at their maximum burial depth and will have higher densities and velocities than similar, but normally compacted, lithologies at the same depths. This is an important consideration on the NE Atlantic margin where there is abundant evidence of Cenozoic uplift and denudation (Doré et al., 2002a and references therein). Denudation appears to have occurred across much of the Irish continental shelf, with the exception of the main Rockall and Porcupine basins (Allen et al., 2002; Doré et al., 2002b). The available density and velocity data have been compared with nominal normal compaction curves in order to identify such overcompaction effects.

6.2 DENSITIES

Figures 8 and 9 display the available digital density logs from exploration wells. Although a variety of lithologies are present in the sedimentary basins along the Irish margin, we have assumed that shale sequences dominate over the region as a whole. This was borne out by comparing assumed normally compacted sections with densities predicted for different lithologies by Sclater and Christie (1980), on the basis of empirically derived coefficients for an exponential relationship between porosity and depth combined with an assumed matrix density. The shale curve of Sclater and Christie (1980) has therefore been used as a common reference line against which to compare the logs shown in Figures 8 and 9. Although there are significant local departures, due to lithological variations or to poor quality log sections (e.g. due to caving), the overall tendency is for the logged densities to lie at or above this nominal normal compaction curve. This is as would be expected, given the likelihood of Cenozoic uplift and denudation at many of the sites sampled.

6.3 VELOCITIES

The initial approach adopted for the analysis of rock velocities was similar to that described for densities, in that an attempt was made to predict velocities on the basis of the porosity-depth relationship of Sclater and Christie (1980) together with an assumed matrix velocity (using the relationship of Wyllie et al., 1956). This proved unsuccessful, however, as there were significant

departures between the curves generated by this method and observed data for normally compacted rocks. The primary reason for this is believed to be that compaction affects the velocity of the matrix material itself to a much greater extent than its density (see Wyllie et al., 1958). An alternative approach was therefore adopted in which a series of relationships was derived that stems from an initial assumption that velocity within the cover sequence varies linearly with two-way travel time. The derivation of these expressions is set out in detail in Appendix 4, because they were also used for converting structural data for the cover sequence from two-way travel time to depth in a fashion that is consistent with the scheme used to predict densities.

The parameters in the empirical relationships were derived by comparison with well logs from areas where there is least likelihood of the effects of overburden removal. For example, thermal history studies on samples from well 35/8-2 in the Porcupine Basin indicate that these rocks are currently at their maximum post-depositional temperature and that there is no evidence of removed section, an interpretation that is compatible with the lack of unconformities within the sequence (Green, 2002). A section sampled by this well between about 2 km and 2.7 km below sea bed has a relatively high velocity, probably for lithological reasons (calcareous units), but much of the remainder of the log should provide a reasonably representative normally compacted section, an assumption that is borne out by comparison with density data for this well (Figure 8, panel 10). This well does not constrain velocities at shallow depths satisfactorily, so was supplemented by other sources, such as the velocity log from ODP borehole 982B (Figure 10). Figure 10 also includes some velocity models from the central part of the Rockall Basin derived from wide-angle seismic experiments. The adopted empirical relationship provides a reasonable fit both with the well data and with the velocity model derived from two-ship expanding spread profile ESP-12 of Joppen and White (1990). The latter profile lies in the central part of the Rockall Basin so is presumed to be relatively unaffected by overcompaction effects. The relationship is similar to the RAPIDS models (Mackenzie et al., 2002a, b) at shallower depths, but diverge deeper within the sedimentary section where the RAPIDS data indicate units with relatively high velocities.

Figures 11 and 12 display velocity logs from individual wells against the nominal, normally compacted trend in an analogous fashion to the density logs discussed earlier. It is noticeable that, in many cases, evidence for denudation provided by the density logs (Figures 8 and 9) is corroborated by a similar offset in the velocity logs (Figures 11 and 12).

6.4 AN ATTEMPT TO QUANTIFY DENUDATION

It is possible to provide quantitative estimates of the thickness of any removed section by computing the depth shift which, when applied the observed density or velocity logs, provides the best fit with the nominal normal compaction trend for that property. This has been done in a simplistic fashion by computing the difference between actual and theoretical depth below sea bed for each point in each log, filtering out extreme values, and then calculating a mean shift. The operation was conducted separately for the Cenozoic and pre-Cenozoic sections. The obvious shortcoming of this approach is that it is applied to the log indiscriminately, and is thus prone to distortion because of lithological variations or data quality problems. As an example, the uplift estimate in well 35/8-2 is distorted by the presence of the lithologically-related high-velocity section at 2 – 2.7 km depth. A more rigorous approach would involve making denudation estimates using only log sections selected on the basis of lithology and data quality. The results of the broad-brush approach nonetheless have some interest, and are displayed in Table 2.

Table 2 Nominal denudation estimates based on differences between log data and assumed normal compaction trends. Log sections less than 50 m in length have been omitted.

Well	Area	Denudation from velocity logs (m)		Denudation from density logs (m)	
		Cenozoic	Pre-Cenozoic	Cenozoic	Pre-Cenozoic
12/13-1A	Erris Basin	-332	653	-397	449
13/3-1	Donegal Basin	95	2807		3496
18/20-1	Slyne Basin				1061
19/5-1	Erris Basin	167	2351		1979
26/22-1A	Porcupine Basin		1444	143	906
26/28-1	Porcupine Basin	124	698	411	842
26/28-3	Porcupine Basin	-130	394		590
27/5-1	Slyne Basin		2545		1919
27/13-1A	Slyne Basin		1821		1444
34/15-1	Porcupine Basin	-60	-61		-333
35/8-2	Porcupine Basin	58	693	-593	552
35/15-1	Porcupine Basin	207	2994	-313	2124
35/19-1	Porcupine Basin	-131		-64	893
36/16-1A	Porcupine Basin	79	1649	347	1863
43/13-1	Porcupine Basin	202	243		1800
48/19-1A	North Celtic Sea Basin		1483		1639
48/25-1	North Celtic Sea Basin		2239		1360
49/19-1	North Celtic Sea Basin		2067		2336
49/29-1	South Celtic Sea Basin		1223		353
55/30-1	Fastnet Basin	493	1628		
56/14-1A	North Celtic Sea Basin	205	1023		
56/18-1	North Celtic Sea Basin	845	865		1513
56/20-1	North Celtic Sea Basin	466	1713	-125	1016
56/22-1	Fastnet Basin	555	1882	-159	2076
57/2-1	North Celtic Sea Basin	761	1764		839
58/3-1	South Celtic Sea Basin		1494		883
62/7-1	Goban Spur	104	928	-224	1194
63/10-1	Fastnet Basin	660	815	-122	545

The nominal denudation estimates are mainly positive, in line with the earlier qualitative appraisal. Although the few negative results could in theory be caused by overpressure, they are much more likely to have lithological or data quality explanations, which would need to be explored in the first instance. There are appreciable differences between the velocity and density denudation estimates for the Cenozoic rocks, but the estimates are predominantly significantly lower than those for the pre-Cenozoic section. This conforms with the evidence for widespread early Cenozoic denudation in this region (e.g. Allen et al. 2002).

The denudation estimates based on velocity and density data from pre-Cenozoic sedimentary rocks are broadly comparable with each other and with other sources of evidence. For example velocity logs from the 12 wells in the Celtic Sea and Fastnet basins indicate a mean denudation

of 1516 m while the 10 of these wells that have density logs indicate a mean uplift of 1256 m. Previously published denudation estimates for this region (e.g. Hillis, 1995; Murdoch et al., 1995) typically indicate values of the order of 1 km.

6.5 VOLCANIC UNITS

Data from DSDP and ODP studies have been analysed to provide insights into the properties of the Palaeogene volcanic rocks which are widespread in the north-west part of the study area. In addition to the drilling sites on this part of the Atlantic margin, data from deep ODP boreholes through analogous volcanic sequences on the Norwegian (Site 642) and Greenland (Site 917) margins were also considered. The available logs from these holes indicate that, although the central, massive components of the lava flows have high P-wave velocities (5 – 6 km/s) and densities (2.8 - 3.0 Mg/m³), the average values for the whole volcanic sequence are significantly less. This is because of the presence of vesicular, altered, brecciated (hyaloclastite) and/or fractured units towards the margins of the flows (Planke, 1994; Planke and Cambray, 1998). The average velocities and densities at Sites 642 and 917 are very similar (Table 3):

Table 3 Average density and velocity from wireline logs through volcanic sequences in ODP boreholes 642E (Vøring margin) and 917A (East Greenland margin)

Borehole	Interval sampled (m)	Density (Mg/m ³)		Velocity (km/s)	
		Mean	S.D.	Mean	S.D.
642E	715	2.53	0.29	4.04	0.85
917A	381	2.53	0.26	4.22	0.93

Note that the true density of a volcanic sequence is likely to be slightly higher than that measured by the borehole logging tool because the tool is not calibrated for rocks of this type. Calculations basic on typical compositions for volcanic rocks and the formulae provided by Schlumberger (1991) suggest that true densities may be around 0.02 Mg/m³ higher than those indicated by the log.

Magnetic property measurements are also available for samples from the DSDP/ODP boreholes. The mean susceptibilities of samples from boreholes 642E and 917A are 34.8×10^{-3} and 12.9×10^{-3} respectively. Measurements from igneous samples from DSDP boreholes 553A and 555, which lie within the IPmmP study area (see the IPmmP GIS for DSDP/ODP locations), are an order of magnitude lower and are considered suspect (it is not uncommon to encounter scaling problems in induced magnetic susceptibilities measured as part of palaeomagnetic studies). NRM (Natural Remanent Magnetisation) intensities are available for boreholes 553A, 555 and 917A and are 3.87 A/m, 2.50 A/m and 3.43 A/m respectively. The direction of magnetisation in all these cases is reversed.

7 Model construction

7.1 INTRODUCTION

Three-dimensional lithospheric modelling was undertaken using a methodology similar to that described by Kimbell et al. (2004). The first stage in the process was to construct a preliminary model of lithospheric structure which incorporated constraints that were independent of the gravity observations that would provide the primary means of refining the model geometries. This initial model included a three-dimensional representation of the structure and density of the

cover sequence and of upper-mantle density variations associated with regional temperature contrasts. An initial estimate of Moho topography was then constructed by assuming isostatic equilibrium and this, and the base of the cover sequence, were subsequently modified to improve the fit with observed gravity anomalies. Flexural modelling was undertaken to investigate how different assumptions regarding the strength of the lithosphere during sediment loading affected the model outputs. Finally, the predicted magnetic effect of the components that made up the initial and optimised models was computed. The models were constructed as a series of continuous grids with a 2 km node interval.

The following sections set out the stages in the modelling process in more detail.

7.2 THERMAL EFFECTS

O'Reilly et al. (1998), Breivik et al (1999) and Kimbell et al. (2004) have demonstrated the need for incorporating thermal effects when modelling gravity anomalies in the vicinity of continental margins. Two-dimensional finite element thermal modelling was conducted using the THERMIC program (Bonneville and Capolsini, 1999) in order to assess these effects. A simple model for a continent-ocean boundary was established, which involved juxtaposing oceanic and continental lithosphere and instantaneously heating the oceanic component to a nominal melt temperature (1333°C). The simulation then 're-heated' the oceanic component at 5 Ma intervals, but on each occasion the edge of the block that was reheated was stepped away from the continent by a distance equivalent to the average half-spreading rate in this part of the Atlantic. Figure 13 illustrates the simulated temperature section at 55 Ma and 105 Ma after ocean opening, which are the approximate minimum and maximum opening ages represented within the study area (Figure 14). These indicate that there is a relatively pronounced thermal contrast where ocean opening has occurred most recently, but that this has largely decayed beneath areas of oldest ocean crust. There is some evidence that the continental upper mantle may be slightly warmer than that at the same level beneath older oceans because of the influence of the higher concentration of heat-producing elements in the continental crust. Horizontal sections were taken through the thermal models to investigate the best way to represent the thermal transition in the 3D models. These indicated that the lateral temperature variations across the continent ocean boundary could be simulated with sufficient accuracy by a 170 km wide linear ramp centred at the continent-ocean boundary.

The upper mantle was represented in the 3D models by a series of 'layers' with laterally varying density. The boundaries between these were set at the Moho and at horizontal interfaces at 30 km, 50 km, 70 km, 90 km and 125 km below datum. A density was defined for each layer at each node of the model grid. For the oceanic upper mantle, a temperature profile was calculated using a 1D plate cooling model together with the estimated age of the ocean crust and the present-day bathymetry. The temperature profile beneath each node was then translated into densities by allowing for both thermal expansion and overburden stress, as described by Kimbell et al. (2004), and averaged within each of the mantle layers. For the continental upper mantle, the temperature profile was based on a nominal geotherm calculated on the basis of a surface heat flow of 55 mW/m² and was converted into densities in the same way. Beneath a 170 km wide corridor centred on the continent-ocean boundary (Figure 14), densities within each upper mantle layer were ramped between the continental and oceanic values on either side. It has been assumed that the conductive cooling model described here extends down to the 1100°C isotherm and that more efficient convective heat transfer below this isotherm substantially reduces thermal gradients (see discussion in Kimbell et al., 2004).

It is recognised that the region will contain additional thermal perturbations that are not simulated in the initial model. The thermal impact of Late Jurassic – Early Cretaceous continental extension should have decayed by now but any more recent extensional episodes, for example affecting the Hatton Basin, may still have a thermal imprint. The event that gave rise to widespread igneous activity on the Atlantic margin at c. 60 Ma could well have left a more

extensive thermal effect than the ‘standard’ passive margin model that has been assumed. O’Reilly et al. (1998) infer that a thermal anomaly beneath the Hatton-Rockall area extends several hundred kilometres from the continental margin. The uniform continental model does not allow for local variations in upper mantle temperature, for example due to variations in the thickness and thermal properties of the crust. These were not included in the model as there are insufficient reliable heat flow measurements to quantify them accurately. The approach that has been employed is to adopt the initial, simple thermal model described above and analyse the results for evidence of its shortcomings.

7.3 INITIAL MODEL FOR THE COVER SEQUENCE

An earlier attempt at 3D gravity modelling in the NE Atlantic region involved the use of a single density-depth relationship for the whole cover sequence (Kimbell et al., 2004). The aim in the present project was to refine the approach to provide a better representation of actual density variations. The key factors that needed to be addressed were the differences in compaction between the Cenozoic and pre-Cenozoic sequences (due to greater denudation of the latter) and the lateral variations in compaction within the pre-Cenozoic units (e.g. between the normally compacted Mesozoic sediments in the deep water basins and those in the uplifted basins on their flanks). In order to do this, the initial cover sequence model was divided into Cenozoic and pre-Cenozoic components and a different density model derived for each. Over such a large area, and with the limited resources available, it was not possible to model the required interfaces in anything but a generalised fashion.

7.3.1 Cenozoic (post-lava) sequence

A model of the thickness of the Cenozoic sequence (Figure 15) was constructed from the available sources (Section 4.2). In the north-western part of the study area the seismic expression of underlying sedimentary rocks is largely masked by the extensive Palaeogene lavas that underlie the Hatton-Rockall area (see following section), such that the acoustic basement used in the construction of published sediment thickness maps for this area (e.g. Roberts et al., 1979; Srivastava et al., 1988) will typically lie at the top of the lavas. The initial model therefore nominally represents post-lava sediments in this area and the full Cenozoic sequence elsewhere. In the south-western part of the study area little information was available on the thickness of the Cenozoic sequence and it was necessary to construct a highly generalised model for the base of the upper part of the cover sequence which does not have a particular stratigraphical significance. Although this is clearly a major approximation, the inaccuracies it introduces in the gravity models are not large, at least in deeper water areas, as the underlying rocks are not extensively over-compacted so a large density jump is not predicted at the base Cenozoic interface.

Data that were only available in two-way travel time were compiled initially and converted to thickness using the procedure described in Appendix 4 (assuming normal compaction). Where necessary, travel time in the water column was estimated using the bathymetric grid employed in this project and assuming a mean sea-water velocity of 1.48 km/s. Data sources that were available in depth were then merged into the compilation, which was edited in regions of overlap, giving greatest weight to the data sources that were considered more reliable.

The density of this part of the sedimentary sequence was assumed to follow the normal compaction curve for shale of Sclater and Christie (1980), as discussed in Section 6. The sequence was divided up into a series of layers parallel to the seabed in order to simulate the compaction effects more accurately.

7.3.2 Lavas in the Hatton-Rockall area

There is little information available on the thickness of the Palaeogene lavas in the Hatton Rockall area, apart from some speculative base lava picks on seismic sections (e.g. Boldreel and Andersen, 1994), evidence for ‘windows’ where they are highly thinned or absent (Hitchen, 2004) and imaging of the seaward-dipping reflector sequence adjacent to the continental margin (Barton and White, 1997a, b). Only a highly simplified representation of this unit was therefore considered appropriate in the 3D models. This included a thickened sequence where seaward-dipping reflectors were assumed to lie on continental crust (the inner reflector package of Barton and White, 1997a, b), feather-edges at the assumed limit of the lavas and where windows have been identified, and approximately 1 km of lavas elsewhere (Figure 16). The average density of this unit was estimated using a nominal compaction trend constructed by the interpolating between the averaged values identified from density logs through thick volcanic sections on the Voring and East Greenland margins (see Section 6.5) and the deeper density data available from the Lopra borehole on the Faroe Islands (Ellis et al., 2002).

7.3.3 Pre-Cenozoic sequence

The structural data for pre-Cenozoic sedimentary thickness that was available only in two-way time was first compiled and depth-converted. This included the interpreted seismic sections of Naylor et al. (1999, 2002) and a variety of other sources (Section 4.2). The depth conversion allowed for the effect of overcompaction on the seismic velocities of rocks which had undergone uplift and erosion using the scheme described in Appendix 4. This required a grid representing the difference between maximum and current depth of burial of the pre-Cenozoic sequence (Figure 17). Only a simplified representation of such denudation variations was considered justifiable, given the limitations of the available data, and an averaged value of 1.2 km was adopted over the shelf areas around Ireland, decreasing to zero beneath the deep water troughs.

The pre-Cenozoic sediment thickness data sources which were available in depth included, where appropriate, data derived from total sediment thickness estimates (e.g. Loudon et al., 2004) by subtraction of the Cenozoic thickness described in Section 7.3.1. All the data sources were compiled within a GIS and edited and merged to provide the model illustrated in Figure 18. The constraints on this model were limited in the Rockall and Hatton basins. In the case of the Hatton Basin, a nominal sub-lava sedimentary thickness of up to about 2 km was included on the basis of the limited information available from wide-angle seismic experiments (e.g. Vogt et al., 1998). Such experiments suggest that rapid thickness variations may occur within this layer but these could not be defined *a priori* so a smoothly varying initial thickness was adopted with the aim of using the gravity data to resolve shorter wavelength effects.

The density of the pre-Cenozoic unit was modelled by assuming the shale compaction curve of Sclater and Christie (1980) offset by an amount determined by the nominal denudation value (Figure 17) at each grid node. The density of the sub-lava sediments in the Hatton-Rockall area is difficult to quantify, but limited AFTA (Hitchen, 2004) and seismic velocity data suggest that this unit is overcompacted. An average denudation similar to that in the shelf areas around Ireland has been assumed, although it is recognised that this is poorly constrained.

The base of the cover sequence as defined for this modelling exercise does not coincide with a particular stratigraphic level, and this is even more the case after the surface has been optimised using gravity anomalies (see following section). The density contrast associated with this surface is primarily that between the Mesozoic sequence and the Lower Palaeozoic and older basement. The Carboniferous strata are ambiguous, as their structure is poorly defined and thus cannot be incorporated in the starting model, and their properties span from those of the cover (in low density Upper Carboniferous units) to those of the basement. The optimised model may thus contain features relating to Carboniferous structures but they are unlikely to be simulated accurately.

7.4 CONSTRUCTION OF AN OPTIMISED 3D MODEL

An optimised lithospheric model was constructed using the following procedure. The potential field computations and inversions were undertaken using the BGS Gmod and Bmod programs (Dabek and Williamson, 1999) which employ wavenumber domain routines developed by Parker (1972) and Oldenburg (1974).

1. An isostatic model was constructed using the topographic data and models for mantle density variations and cover sequence structure described above. An average density for the crystalline crust of 2.85 Mg/m^3 was assumed, together with a reference Moho depth of 30 km (i.e. its nominal depth when the topographic surface lies at datum and no cover sequence is present). The Moho depth was adjusted to equalise the load at a compensation depth of 125 km.
2. The gravity field over the entire model (down to 125 km) was computed. Following Kimbell et al. (2004), the average offset between the computed field over this isostatic model and the observed field was used to define a 'background' which was subtracted from observed gravity anomalies prior to model optimisation. In this case a shift of -15 mGal was applied to the observed anomalies.
3. The Moho interface was smoothed to remove shorter wavelength variations and then its geometry was optimised to improve the fit with observed longer wavelength gravity anomalies (employing a wavelength filter with a ramp between 67 km and 100 km).
4. The base sediment interface was optimised to accommodate shorter wavelength gravity variations, although it was still necessary to apply a low pass filter (ramp between 10 km and 20 km) to avoid instability.
5. The density structure of the sedimentary components and the upper mantle was re-computed using these modified interfaces. The density structure of the pre-Cenozoic sedimentary unit was subdivided (in a similar fashion to the Cenozoic sediments) to provide a better representation of compaction effects. A mid-crustal interface was introduced which equally divided the crystalline crust into upper (2.75 Mg/m^3) and lower (2.95 Mg/m^3) components.
6. A further optimisation of the Moho interface was undertaken, using the same filter settings as in step 2. The change in Moho depth was re-scaled to reflect the movement in the mid-crustal interface which was applied subsequently.
7. A further optimisation of the base sediment interface was undertaken, and the depth changes scaled by a factor reflecting the ratio between the local contrast at this boundary and the average contrast between the pre-Cenozoic sedimentary unit and the crystalline crust at each grid node.
8. The sedimentary and upper mantle densities were recomputed and a final forward gravity calculation was made using the complete model.

Figure 19 shows the thickness variations in the pre-Cenozoic sedimentary component after this optimisation process and Figure 20 shows the thickness of the entire cover sequence. The variations in the thickness of crystalline crust and depth to Moho are illustrated in Figures 21 and 22 respectively. The modelled field over the final model (Figure 23) matches the observed field (Figure 2) reasonably well, although more detailed inspection of residual anomalies (Figure 24) reveals a number of relatively large amplitude discrepancies, for example over igneous centres (which were not explicitly modelled). There is a general trend for residual anomalies to follow the observed anomaly trend (i.e. residual highs where there are highs in the observed field and vice versa). This is probably because of the scaling of optimisation changes used in steps 6 and 7, which were necessary to reduce the risk of instability and provided asymptotic convergence. The root mean square residual gravity anomaly over the final model is 1.92 mGal.

The load anomaly of the final model (Figure 25) illustrates relatively modest departures from local isostasy (± 20 MPa over much of the study area). An apparent extension factor (Figure 26) was calculated from the stretching required to thin the nominal 30 km thick continental crust to the values illustrated in Figure 21.

Figures 27 to 29 illustrate the similarities between the geometries defined by the optimised model and those interpreted from recent deep seismic experiments (Mackenzie et al., 2002a). A comparison with the original RAPIDS transect is less easy, because of differences between published versions of the structure revealed by this line, but a comparison with more recent interpretations is shown in Figure 30. Such comparisons will be discussed further in Section 8.

7.5 FLEXURAL MODELLING

In the flexural modelling, the following processing sequence was undertaken:

1. All or part of the section defined by the initial cover sequence model was backstripped assuming a variety of values for the effective elastic thickness (T_e) of the lithosphere and using the thin elastic plate approximation.
2. The Moho depth was calculated using the ‘unloaded’ topographic and top basement interfaces and assuming local isostatic equilibrium. The backstripped component was reintroduced into the model, restoring the topography and top basement to their original positions and flexing the Moho downward by the amount dictated by the original backstripping.
3. The gravity and load anomalies over each model were calculated.

The sequence did not incorporate modelling of the thermal effects of lithospheric extension, so does not provide insights into subsidence history. It does, however, provide insights into the extent to which the cover sequence is supported by the strength of the lithosphere and how this strength has varied with time. Two backstripping sequences were conducted. In the first (results shown in Figures 31 and 32), the entire cover sequence was backstripped whereas in the second (Figures 33 and 34) only the Cenozoic sedimentary component of the cover sequence was employed in the backstripping. The latter was designed to test the hypothesis that thermal events early in the Cenozoic may have weakened the lithosphere and allowed local isostasy to be established prior to the deposition of the Cenozoic sediments.

7.6 MAGNETIC MODELLING

The optimised model was used as the basis of the forward calculation of the magnetic field shown in Figure 35. It was assumed that the crystalline crust has a uniform magnetisation of 1 A/m in the direction of the Earth’s present field and that the lava unit in the Hatton-Rockall area has a reversed magnetisation of 3 A/m. Figure 36 shows the magnetic field computed assuming the properties described above but using the initial cover sequence model rather than the optimised version. Comparison with the observed field (Figure 4) indicates substantial differences, reflecting the influence of complex magnetisation variations within the crystalline basement and the intrusive and extrusive igneous rocks which are not simulated in the forward models. These models nonetheless can be used in qualitative analysis to identify property variations within the basement and assess the validity of features introduced by the optimisation process (see further discussion in Section 8).

8 Discussion of the modelling results

8.1 REGIONAL SETTING

Figures 37 and 38 illustrate the gravity and magnetic fields respectively over the region surrounding the IPmmP study area. The primary purpose for including these is to highlight structural lineaments identified by previous imaging and modelling which straddle the northern margin of the IPmmP study area and thus may be more difficult to identify on the basis of IPmmP data alone. The features of interest form the Anton Dohrn Lineament Complex of Kimbell et al (2005). The central of these lineaments can be correlated with a long-lived terrane boundary between the Archaean Hebridean terrane to the north and the Early Proterozoic Islay-Inishtrahull terrane to the south (Dickin, 1992). This, and strands to the north and south, appear to disrupt the Rockall Basin and are associated with other alignments in the gravity and magnetic anomalies in the Hatton-Rockall area. There is also evidence that they influenced the form of the continent-ocean boundary in the Hatton Bank area and the pattern of deformation resulting from Cenozoic compression in this area (Kimbell et al., 2005).

Kimbell et al. (2005) also identified the South Hatton Lineament separating northern and southern parts of the Hatton Basin (Figures 37 and 38) and the results of the new modelling provide an opportunity to reassess this feature.

8.2 OVERVIEW OF THE OPTIMISED 3D MODEL

8.2.1 Main features

On a broad scale, the optimised model confirms the well-known structural configuration of the region, with highly stretched crust and shallow Moho beneath the Rockall Basin and Porcupine Basin and more normal thicknesses elsewhere (Figures 21 and 22). The modelled average thickness of the crystalline crust beneath the Rockall Basin is 5-6 km but there is a distinct increase in crustal thickness in the north, with values of around 10 km characterising the part of the basin to the north of the Irish Designated Zone. Wide-angle seismic experiments (Roberts et al. 1988) and gravity modelling (Kimbell et al., 2005) confirm that lower apparent extension factors characterise the Rockall Basin to the north of the present study area. The change in degree of extension between the northern and southern parts of the Rockall Basin may have been accommodated by transfer movements on the intervening Anton Dohrn lineament zone (Kimbell et al., 2005). The crust beneath the deeper parts of the Hatton Basin is typically 13-16 km thick (Figure 21), suggesting an extension factor of around 2 (Figure 26), significantly less than the Rockall and Porcupine basins.

At least some of the areas of extreme crustal thinning indicated by the model beneath parts of the Rockall and Hatton Basins (Figure 26) may be artefacts due to instability in the inversion and limitations of the modelling assumptions (see further discussion below), but the potential for continental crust to have been stretched 'to the limit' cannot be dismissed. Some recent models invoke unroofing of the mantle lithosphere beneath the Porcupine Basin (Reston et al., 2004; Readman et al., 2005) and possibly also the Rockall Basin (Pérez-Gussinyé et al., 2001).

The optimised model provides considerably more detailed picture of the structure of the cover sequence than a previous regional 3D modelling exercise on this margin (Kimbell et al., 2004, 2005). This is mainly because of a more detailed approach to the structure and properties of the initial cover sequence model and the higher resolution of the gravity field available for this study. The details of the small basins on the flanks of the Rockall Basin are better resolved than in previous studies and a significantly more complex model for the structure of the Hatton Basin has been produced (Figures 19 and 20; Section 8.5). The inferred structure for the pre-Cenozoic

sedimentary rocks includes linear zones where there are sharp thickness changes implying fault control. Compare, for example, the initial and optimised geometries for the Slyne and Erris basins and eastern margin of the Porcupine Basin (Figures 18 and 19). The deep structure of the the Hatton Basin is speculative, because it relied on removal of the gravity effect of the post-lava sequences in this basin on the basis of very limited data. Errors in the initial top lava surface will have been absorbed (and amplified) by artefacts in the modelled base of the cover sequence. Nonetheless, there is support for rapid thickness changes in a pre-Cenozoic component of the cover sequence from seismic surveys (Vogt et al., 1998), and the trend of the structures inferred from the gravity model matches that of Mesozoic structures elsewhere in the study area.

The oceanic crust is significantly thicker in the north-west corner of the study area adjacent to the Hatton continental margin than beneath the Porcupine Abyssal Plain. This reflects the volcanic nature of the Hatton margin, where generation of thicker than normal oceanic crust has been ascribed to high mantle potential temperatures resulting from the influence of the Iceland Plume (White and McKenzie, 1989). A particularly interesting feature of the crustal thickness pattern is the zone of thickened oceanic crust to the south of the Charlie Gibbs fracture zone, that extends north-westwards from 21°W 51°N (Figure 21, but see GIS version for more detail). A conjugate of this feature occurs on the opposite side of the Atlantic Ocean (BGS, unpublished modelling), indicating that it probably dates from the time the oceanic crust was formed. The age of the ocean crust when the thickened zone first developed (c. 55 Ma) suggests strongly that this reflects a southward extension of the thermal anomaly that was responsible for the enhanced magmatism on the Hatton margin further north. The advantage of the southern feature is that oceanic crust lies on either side of it so it is possible to calibrate the development of the thermal anomaly in this area. It appears to have developed rapidly (over a period of $\leq 1\text{Ma}$) but decayed over a longer time-scale.

8.2.2 Comparison with deep seismic experiments

An obvious difference between the 3D model and seismic models (e.g. Figures 27 to 30) is that the crystalline crust in the former is arbitrarily divided into two layers of equal thickness whereas the latter are able to resolve the velocity discontinuities and often indicate a three-layer crust. Such layering cannot be resolved from gravity data and the mid-crustal interface is used as a mechanism for handling the transition from the density contrast at the base of the cover to that at the Moho effectively, without introducing undue complexity into the models. The results should still be comparable, in terms of crustal thickness and depth to Moho, provided the overall average density assumed for the crystalline crust remains valid. The locations of the seismic lines discussed below are contained in a layer within the project GIS (see Appendix 2).

The Moho predicted by the optimised model is typically within about 2 km of that determined by interpretation of the RAPIDS 3 wide-angle seismic data (Figures 27 to 29). The RADIDS 33 profile revealed an asymmetry in the pattern of crustal thinning across the Rockall Basin, with a steeper flank to the south-east than to the north-west, and this is very well reproduced by the 3D model (Figure 28). The agreement between the model and seismic Moho beneath the Rockall Basin is perhaps surprising, given the evidence for a relatively low seismic velocity in the upper mantle beneath the basin, which has been interpreted as the result of serpentinisation (O'Reilly et al., 1996; Mackenzie et al., 2002a, b). This potential low density zone is not incorporated in the model and thus might be expected to result in the model Moho lying at greater depth than the seismic Moho (Kimbell et al., 2004). It may be that the density effect of serpentinisation is offset by a thermal effect (relatively cold upper mantle because of thinning and reduced heat production in the overlying crust). It is also possible that the reference depth set for the Moho (30 km) is too shallow. This user-defined datum can be modified if the evidence supports it, and should be kept under review as the results of further wide-angle experiments become available. It is likely, however, that a more complicated picture will emerge as a result of more extensive seismic control, and that this will involve regional variations in the crustal and upper mantle density due to both compositional and thermal variations.

The data quality from the RAPIDS 1/2 (transverse) line (Figure 30) appears inferior to that from RAPIDS 3, as there are parts of the line where the Moho was poorly resolved. The model indicates a similar depth to Moho beneath the Rockall High (c. 28 km) and the Hatton Basin (20 km) to the seismic experiment, but there is a significant mismatch further west (at about 300 km in the profile shown in Figure 30). This could be in part because of a relatively low density crust, suggested by the absence of a lower crustal layer in the seismic interpretation, although an additional contributing factor is required to explain the scale of the mismatch. This could be a low density zone in the uppermost mantle, perhaps due to a thermal anomaly or to depletion (associated with melt extraction to form the neighbouring underplated zone). The results from the HADES experiment should shed more light on this. The mismatch in Moho depth across the underplated zone is explicable in terms of the relatively high density of this zone compared with the 'normal' crust assumed in the model. The modelled Moho depth beneath the oceanic crust at the western end of the line (13 km) is greater than that indicated by the RAPIDS interpretation, but closely matches the depth of the interpreted seismic Moho on the nearby CAM77 seismic line (Barton and White, 1997a).

The 3D model provides a good match to seismic structure (as shown by O'Reilly et al., 1998) beneath the central and western parts of the Rockall Basin on the RAPIDS 1/2 transverse line but there is a zone of apparent 'necking' in the model at about 860 km which is not supported by the seismic evidence (Figure 30). This is due to the gravity inversion becoming unstable and generating excessive thinning in the crystalline crust and thickening of the sedimentary section. This interpretation is supported by comparison with the results of the nearby ESP12 profile of Joppen and White (1990) which detected the Moho at a depth of 13.5 km beneath 5.6 km of crystalline crust at a location where the model indicates values of about 12 km and 4 km respectively. Areas where instability in the inversion may have occurred are indicated by very high extension factors in Figure 26, although this is not necessarily always the explanation, as it is possible that extreme stretching has occurred in places (see further discussion below).

The model agrees with the RAPIDS 2 axial line (Hauser et al., 1995) in defining a typical crustal thickness of 5-6 km beneath the Rockall Basin and an increase in Moho depth from about 11 km in the vicinity of the Charlie Gibbs fracture zone to about 15 km at the intersection with the RAPIDS 2 transverse profile. It indicates that the thicker crust at the latter intersection is the expression of a feature that extends north-eastwards along the axis, which is crossed obliquely by the axial line.

Further comparisons with deep seismic models are possible over the Rockall High and Hatton Basin through interpretations published by Scrutton (1970, 1972), Bunch (1979) and Smith et al. (2005). Line A of Scrutton (1970, 1972) was re-interpreted by Bunch (1979) who inferred that a transitional Moho lay at a depth of 29.5-31 km at its south-western end, beneath the Rockall High. It is not possible to register the location of this depth estimate precisely from available data but it lies in an area where the 3D model indicates a Moho depth of between 29 km and 30 km. Beneath the northern part of the Hatton Basin the seismic Moho was inferred to lie at a depth of 22 km by Scrutton (1972) and 19 ± 2 km by Smith et al (2005); the 3D model indicates a Moho depth of between 20 km and 22 km in the area covered by these experiments.

The modelled crustal thickness beneath the Porcupine High agrees well with the value of 28 km estimated by Whitmarsh et al. (1974) from a seismic refraction experiment, and there is also agreement with the inferred crustal thickness beneath the eastern part of COOLE 3A across the Irish Mainland Platform (Makris et al. 1988). The 3D model has significantly thinner crust beneath the Porcupine Basin and the Porcupine Abyssal Plain than was interpreted for the western end of COOLE 3A and COOLE 3B (Makris et al. 1988). Although the gravity model may underestimate crustal thickness beneath the basin, the seismic thickness estimates appear excessive and have probably been impaired by poor ray coverage towards the ends of the two COOLE lines (the central part of the basin was not covered by this experiment). This is the implication of the gravity model of Conroy and Brock (1989). An underestimate of oceanic

crustal thickness in this area is corroborated by comparison with the WAM profile (Horsfield et al., 1994), where the seismic estimate is 1 – 2 km greater than that predicted by the 3D model. White (1992) tabulates results from 7 seismic soundings around the Goban-Western Approaches margin that indicate an average seismic thickness for the crystalline crust of 6.37 km while the average modelled crustal thickness at the same sites is 5.23 km. There is little seismic evidence for the thickness of the oceanic crust beneath the Porcupine Abyssal Plain further to the west, away from the continental margin, but the comparisons described above suggest that the typical modelled thickness of 3-4 km in this area (Figure 21) is an underestimate. This could arise in part because the density of the oceanic crust is underestimated, but inaccuracies in other modelling assumptions may also be involved. For example there may be lateral changes in mantle density not allowed for in the modelling. The oceanic crust in this region may nonetheless still be thinner than the global average of about 7 km, as Thinon et al. (2003) cite values of 3-5 km for the oceanic crust off the North Armorican margin to the south.

The seismic model for the COOLE 85-7 line south of Ireland indicates a Moho which increases in depth from 26 km in the west to 24 km in the east (O'Reilly et al., 1991). The Moho in the 3D model is at a depth of about 25 km at the ends of the line and up to about 27 km towards its centre.

8.3 FLEXURAL MODELLING

The gravity fields calculated over flexural models in which the lithosphere is assumed to have strength throughout the history of sediment loading (Figure 31) show clear departures from the observed field which can be correlated with disparities between the predicted load anomalies and those over the optimised model (Figure 32). This is most obvious over narrow and deep Mesozoic sedimentary basins (e.g. those to the south of Ireland and the perched basins on the flanks of the Rockall Basin), where support of a sedimentary load by lithospheric strength leads to strong positive gravity and load anomalies which are contrary to the observations. The inference is that the lithosphere was weak ($T_e \leq 5$ km) during the development of these basins, or at least that their history was punctuated by episodes of weakness (extension and/or heating) which allowed isostatic equilibrium to be reset. One possibility is that the event that led to widespread early Cenozoic uplift in the region was associated with heating and weakening of the lithosphere, and this has been investigated by a second set of models in which strength was assumed only during deposition of the Cenozoic (post-lava) sediments (Figures 33 and 34).

An assessment of the flexural history of the Hatton Basin is complicated by the lack of independent evidence regarding the pre-lava sedimentary sequence, but there is no clear evidence of strong lithosphere in the current results. The most marked thickening of the post-lava sedimentary sequence within this basin occurs at about 18.6°W 56.7°N. The gravity anomaly over this feature is slightly subdued, and this coincides with a modest positive load anomaly in the optimised model, but comparison with the flexural modelling trials indicates that the lithospheric strength required is small ($T_e \leq 5$ km). If lithospheric strength had been significantly greater than this during deposition of the post-lava sequence it should have generated a more conspicuous positive gravity effect. Similarly, the gravity and load anomalies over the thick sedimentary sequence to the south of Edoras Bank (between 21°W and 24°W and just north of 55°N) appear indicative of weak lithosphere. The only part of this area where greater lithospheric strength appears a possibility is toward the continental margin, where the positive isostatic anomaly over the inner package of seaward-dipping reflectors (Kimbell et al., 2005) might indicate that these are supported at a relatively high level because of such strength. Other factors, such as the influence of dense intrusions beneath the reflectors, may also be important, however, so a more detailed analysis of these features is required before coming to a firm conclusion.

There is evidence of greater lithospheric strength beneath the Rockall Basin. The optimised model indicates a distinct load anomaly pattern across the flanks of this basin, with negative anomalies following the topographic slopes at the basin margins and parallel positive anomalies

lying about 50 km toward the centre of the basin. This load anomaly pattern is closely replicated by models incorporating strength during sediment loading. The strength estimates are hampered by distortion due to inaccuracies in the initial cover sequence model, but the gravity and load anomalies (Figures 31 and 32) suggest that, in the north-eastern part of the basin, an effective elastic thickness of 15 - 20 km could explain the observed patterns if this only applied during Cenozoic sediment loading. Somewhat lower Cenozoic strength ($T_e = 5 - 10$ km) appears more appropriate in the southern part of the basin, and weak lithosphere ($T_e \leq 5$ km) works best in the far north-west. In places the observed gravity field and load anomalies contain features that are not explained by any model based on the initial sediment thickness estimates and assumptions regarding strength during sediment loading. A particular example of this is the positive gravity and load anomaly centred at 17.8°W 53.8°N, which appears to be due to anomalous crust in the region between the two main components of the Barra Volcanic Ridge System. Another such feature is the gravity and load anomaly low along the axis of the Rockall Basin between about 11°W 56.3°N and 15°W 54.5°N, which appears to be due to relatively thick crystalline crust beneath this axis, perhaps resulting from migration of extension towards the flanks of the basin as the central axis cooled and strengthened (O'Reilly et al., 1995).

When the entire cover sequence is incorporated in the flexural modelling of the Rockall Basin (Figures 33 and 34) the responses are distorted because of the anomalous effects over the Mesozoic 'perched' basins on its flanks. This does not necessarily mean that lithospheric strength had no influence during Mesozoic deposition, since strength during the Cretaceous could contribute to the responses seen but cannot be explored using the current cover sequence model because of the lack of appropriate interfaces. Extending the period over which the strength had an effect would reduce the estimate of its average magnitude.

A number of interpretations have been put forward for the deep structure beneath the northern part of the Porcupine Basin, including highly thinned continental crust (Johnson et al., 2001) and unroofed, partially serpentinised upper mantle (Readman et al., 2005). Regardless of the nature of the underlying basement, the free-air and isostatic gravity anomaly high that coincides with the northern part of this basin indicates an isostatic imbalance. It is not possible to generate the positive gravity anomaly without placing the sedimentary infill at a higher level than would be dictated by local isostasy. The shapes of the load and gravity anomalies provide some insight into when this strength was acquired. If it is assumed to apply only to Cenozoic deposition, the anomalies are rather broader and offset slightly to the north of those observed (Figures 33 and 34). Assuming strength over a longer period provides a better replication of the anomaly shape (Figures 31 and 32) although it is probable that this applies primarily to the 'sag' phase of Cretaceous deposition, and that the main Late Jurassic to Early Cretaceous rift phase was characterised by weak lithosphere. When the present modelling is combined with the earlier results of Kimbell et al. (2004) an average effective elastic thickness of about 10 km during deposition of the Cretaceous and younger sedimentary rocks appears likely.

A striking feature of the gravity fields predicted by the flexural models is the way they simulate the contrast between the gravity expression of the northern and southern parts of the Porcupine Basin simply in terms of present-day basin geometry and flexural-isostatic history, without invoking any changes in the properties of the underlying basement. This is not denying the potential influence of basement lineaments on the evolution of the basin, as suggested by Masson and Miles (1986) and Readman et al. (2005) amongst others, but invites caution when attempting to analyse the gravity signatures over the basin in terms of such contrasts.

The southern part of the Porcupine Basin is not particularly well resolved by the optimised gravity model as the inversion has not simulated the central residual gravity low in this part of the basin (the modelled crystalline crust appears excessively thin in this area). Readman et al. (2005) suggest that this low is due to crustal thickening analogous to that along the central axis of the Rockall Basin, as discussed above. The flexural modelling results in this vicinity should also be treated with caution, particularly where the whole sedimentary sequence was

backstripped, as in parts of the basin it was not possible to construct an isostatic model of the pre-existing structure because the crustal thickness reduced to zero before local isostasy was achieved. Despite this, the flexural modelling results indicates that, in a qualitative sense, the NE-trending residual gravity highs flanking the central low described above may reflect the influence of lithospheric strength during sediment loading in an analogous fashion to the similar features that flank the Rockall Basin.

8.4 MAGNETIC MODELLING

The main fact revealed by the forward magnetic modelling (Figures 35 and 36) is that it is not possible to explain much of the observed magnetic signal over the study area (Figure 4) by applying a uniform magnetisation to the modelled crystalline crust and assumed lava layer. Clearly, substantial contributions are made by lateral variations in basement magnetisation combined with a variety of intrusive and extrusive magnetic sources, including both reversely and normally magnetised Palaeogene units. Despite this, the forward magnetic models do reproduce some of the broader features of the magnetic field and provide useful corroboration of some of the modelling results. In regions where the upper-crustal basement is magnetic, the magnetic models provide a useful resource for assessing confidence in features generated by the gravity optimisation. Local correlations such as this will be referred to in Section 8.5, and the present section will address broader patterns.

The models reveal clearly that the regional magnetic lows over the Rockall and Porcupine basins can be explained by the thinning of magnetic crystalline crust beneath these basins. The magnetic crust probably extends westwards beneath the Hatton-Rockall area (see below) but the basement beneath the basins to the south and east of Ireland is less magnetic, as the sharp magnetic signatures over these basins in the forward magnetic model are not reflected by the observed field. This is probably because the upper part of the basement in this region comprises Lower Palaeozoic metasedimentary rocks which generally have low magnetisations.

Within the Irish sector of the Hatton Basin, high amplitude NNE-trending magnetic highs and lows show a partial correlation with basement highs and lows suggested by the 3D modelling. However the differences in the detail of the anomaly pattern and the far smaller amplitudes of the anomalies in the forward magnetic model indicate that this is not simply a case of variations in the thickness of non-magnetic sediments over 'normal' magnetic crystalline basement. There are two additional factors that could contribute to the anomaly pattern. Firstly, Palaeogene lavas and sills with reversed magnetisation may be thicker within the thicker parts of the cover sequence increasing the effective magnetisation contrast between cover and basement and thus the anomaly amplitude. Secondly, there may be additional highly magnetic intrusive/extrusive sources which are responsible for the strongly linear features evident in the observed magnetic field. Most prominently, a pronounced linear positive magnetic anomaly extends almost 500 km in a north-north-east direction between 21°W 53°N and 18°W 57°N and is partially coincident with the Fangorn High. A number of alternative potential magnetic sources could be proposed, but one of the more attractive options is that normally magnetised igneous units were emplaced at the same time as the Barra Volcanic Ridge System (Bentley and Scrutton, 1987; Scrutton and Bentley, 1988). The latter is responsible for the arcuate magnetic anomalies of similar amplitude which extend across the Rockall Basin to the south-east and is of probable Cretaceous age. The change of in the trend of the igneous features between those mapped over the stretched crust of the Rockall Basin and those over the thicker crust of the Rockall High – western Hatton Basin area could reflect the controlling influence of a major fracture system in the latter area.

The magnetic signatures appear to change between the southern and northern parts of the Hatton Basin. In the north, the thickest parts of the cover sequence tend to correlate with magnetic highs rather than lows, possibly because reversely magnetised Palaeogene lavas are thinner beneath the basin than on its flanks as a result of thickness changes across the lava escarpments at the basin margins. The NNE trend is less pronounced in the north, although there are weak indications of

the continuity of magnetic lineaments across the divide. There are magnetic discontinuities at the South Hatton Lineament of Kimbell et al, (2005) (Figure 38), and it appears possible that there may be an additional discontinuity slightly further north, in the vicinity of the median line. The latter is difficult to identify with confidence in the current compilation, however, because of the marked change in magnetic data quality at that line.

The observed magnetic field in the southern part of the Rockall Basin is dominated by the effects of the Barra Volcanic Ridge System. Further north within the basin there are subtle magnetic features in the observed field that appear to be due to variations in the depth and thickness of the crystalline crust beneath the basin. A significant proportion of these features are reproduced by the optimised model (Figure 35) but not by the initial model (Figure 36) indicating that the optimisation process has recovered real variations in crustal structure. Although the igneous centres in the northern part of the basin were not explicitly modelled, they have, by default, been assigned the same normal magnetisation as the basement and comparison with the observed anomalies indicates that the Hebrides Terrace centre actually has a reversed magnetisation while the Anton Dohrn centre contains both normal and reversed components.

8.5 A REVIEW OF MODEL FEATURES

The text of this section is incorporated in the IPmmp Model Viewer (Section 5.6) and can be viewed alongside images of the model using that interface. It is recommended that the Model Viewer and/or the IPmmp GIS are consulted while reading this text as these allow the user to see the model details and register and compare these with other information (e.g. previous structural mapping, magnetic images) in a way that is not possible using the illustrations in this report. The various features discussed have been given abbreviations that are used in this discussion (shown in bold font), on an annotated map included in the IPmmp Model Viewer, and in a layer within the GIS. A reduced version of an annotated layer is shown in Figure 39 and the features are listed alphabetically in Appendix 5.

The Hatton continental margin (**CM**) is characterised by two packages of seaward-dipping reflectors (Barton and White 1997a, b). An outer package is normally magnetised and appears to have been extruded during the C24N polarity interval. To the north-west of this are a series of parallel positive and negative magnetic anomalies characteristic of oceanic crust (Figure 4). The inner seaward-dipping reflector package (**SDR**) coincides with a negative magnetic anomaly and has been proved by drilling at DSDP Site 553 to be composed of reversely magnetised lavas, probably extruded during chron C24R (Roberts et al., 1984). Following Kimbell et al. (2005) the continent-ocean boundary employed in the present modelling has been placed between these two packages. The inner package (**SDR**) was simulated in a simple fashion in the lava thickness model (Figure 16) and the forward magnetic modelling (Figure 35) indicates that this generates the required magnetic low.

Inboard of the seaward-dipping reflectors are the Hatton Ridge basins, which have northern (**HRBN**) and southern (**HRBS**) parts, separated by the South Hatton Lineament of Kimbell et al. (2005). Seismic evidence for this offset is provided by Roberts et al. (1979). The post lava sequence in the southern basin has been drilled at DSDP Site 555 and, while this demonstrates post-lava sedimentary thickening, the gravity modelling suggests that a pre-lava component is also required. Seismic control is very limited, but there is a weak indication of possible reflections from a sub-lava sequence on line CDP87-3 of Keser Neish (1993).

The cover sequence has a modelled thickness of 3-6 km in the northern part of the Hatton Basin (**NHB**), with the thickest deposits lying along an east-north-east-trending axis. The upper part of this sequence comprises Cenozoic sediments that have been imaged by normal incidence seismic reflection surveys and proved by drilling at DSDP Sites 116 and 117 and ODP Site 982. Wide-angle seismic surveys indicate a lower cover sequence layer with a velocity of 4.5 – 4.7 km/s, which is ≥ 2 km thick in the interpretations of Scrutton (1972) and Smith et al. (2005) but

somewhat thinner in the interpretation of Keser Neish (1993). The overall cover sequence thickness predicted by the 3D model is similar to that of Smith et al. (2005), slightly lower than that of Scrutton (1972) and greater than that of Keser Neish (1993). Smith et al. (2005) dismiss the idea that the 4.5 – 4.7 km/s layer is basaltic on the basis that the velocity is too low. This, however, appears contrary to the physical property results from ODP drilling (see Section 6.5) and those reported by Archer et al. (2005) for the North East Rockall Basin, which suggest that average velocities of this magnitude can characterise such volcanic sequences. When combined with the seismically opaque and hummocky nature of the top of the lower layer of Smith et al. (2005; their fig. 5), it appears likely that at least the upper part of this layer is volcanic. The hummocky seismic character suggests submarine deposition of the lavas within the Hatton Basin, contrasting with the parallel-bedded seismic facies of the subaerial lavas on the surrounding highs (Boldreel and Andersen, 1994). The contrast in style occurs across the volcanic escarpments at the margin of the basin. Boldreel and Andersen (1994) inferred that the submarine facies has a lower velocity than the subaerial facies, although this does not appear to be the case in the log data reported by Archer et al. (2005). The presence of a volcanic layer within the basin does not preclude the possibility of an older (syn-rift) sequence, as there is seismic evidence of deformed sediments beneath the lavas on the Hatton High (Keser Neish, 1993; Hitchen, 2004) and boreholes proving mid-Cretaceous sedimentary rocks in this area (Hitchen, 2004). The tendency for high magnetic field values to occur over the deepest parts of the basin suggests that the volcanic sequence is thinner there than on its flanks (assuming reversed magnetisation).

Kimbell et al. (2005) suggested that the South Hatton Lineament forms a discontinuity between the northern Hatton Basin (**NHB**) and southern Hatton Basin (**SHB**). There is evidence in the IPmmP imaging and modelling results for this lineament, which extends in an east-south-east direction from the discontinuity between the northern and southern Hatton Ridge basins (**HRBN** and **HRBS**). There is also the suggestion of a second discontinuity about 70 - 100 km to the north and close to the median line, although this is difficult to resolve with confidence because of the pronounced change in data resolution across this line.

The model for the southern part of the Hatton Basin (**SHB**) is characterised by a series of highs and lows with a north-north-east trend. Some of the modelled structure at the base of the cover sequence may be an artefact due to shortcomings in the initial model for cover sequence structure at shallower levels (e.g. the top lava interface), but seismic data along the RAPIDS profile indicate rapid thickness changes in a lower sedimentary layer, compatible with the configuration of the 3D model (Vogt et al., 1998; Figure 30). Further evidence for rapid changes in the thickness of the pre-lava unit comes from a GEUS seismic line (**GL**) shot in the south-east part of the basin which detected pre-lava sediment thickness variations that can be correlated with features in the 3D model (Boldreel and Andersen, 1994; Edwards, 2002). The lower layer on the model of Vogt et al. (1998) had an average velocity of 4.2 – 4.5 km/s and these authors suggested that it comprises overcompacted syn-rift sedimentary rocks. However, as discussed for the northern part of the basin, it appears likely that this package includes a volcanic component. The structural highs in the 3D model generally coincide with magnetic highs, suggesting that they contain normally magnetised rocks. As discussed in Section 8.4, the high amplitude of the anomalies suggests the influence of sources with a strong normal magnetisation (basement plus Cretaceous igneous units?), and the anomaly amplitudes may be enhanced by juxtaposition with units with reversed magnetisation (Palaeogene lavas, sills and intrusions).

The magnetic expression of the Fangorn High (**FH**; Roberts, 1975; Roberts et al., 1979) is more extensive than its structural expression, so it is possible that the latter is only partially coincident with a more extensive underlying igneous body. A small reversely magnetised feature (**RMF**) with an east-north-east trend lies on the western flank of the Fangorn High. This coincides with a local topographic high and is likely to be a Palaeogene intrusion. Although reversed magnetisation characterises this unit, and the other Palaeogene igneous units within the Hatton-Rockall area for which palaeomagnetic determinations are available, there is evidence that

Palaeogene magmatism also occurred during normal polarity intervals. In the northern part of the Hatton Basin a series of Palaeogene igneous centres have been identified on the basis of their gravity expression – Sandarro (**SO**), Sandastre (**SE**), Owlsgard (**O**), Mentone (**M**) and Aramassa (**A**). Of these, Owlsgard and Aramassa have signatures indicative of normal magnetisation and the magnetisation of the others is not well resolved. The presence of normally magnetised Palaeogene intrusive (and extrusive?) phases further complicates the magnetic interpretation in this area.

A thick sedimentary sequence to the south of Edoras Bank (**SEB**) was investigated at DSDP Sites 405 and 406 (Shipboard Scientific Party, 1979). Site 406 drilled to Middle Eocene rocks at a depth of 831 m, and seismic evidence suggests that the basement lies about 2 s TWT below this. Bull and Masson (1996) suggested that the acoustically transparent, lower part of this sequence comprises reversely magnetised lavas. This explanation is considered unlikely, however, as the magnetic model published by Bull and Masson (1996) is unconvincing. The modelled thickening of the sedimentary unit between the DSDP sites and the reversely magnetised Rohan igneous centre (**R**), about 50 km to the south, correlates closely with a magnetic high and this signature is more indicative of the thinning of a layer with reversed magnetisation than its thickening.

Naylor et al. (1999) identified the Colmán Basin (**COLB**) from its seismic expression on line WI-32, but were not able to define its lateral extent because of lack of data. The 3D model suggests that it is a linear feature, extending about 80 km to the north-east of this seismic line but only a short distance to the south-west (compare the model with the Rockall Structural Elements Map of Naylor (1999), which is incorporated in the IPmmP GIS and Viewer).

The modelling results suggest that a basin with a similar north-eastward trend (**RHB1**) is located on the Rockall High about 80 km to the east of the Colmán Basin. The form of the gravity anomaly over this feature suggests that it is a half-graben which is faulted on its south-eastern side. Naylor et al. (1999) mapped a fault which coincides with the inferred basin margin where it was crossed by GSI Line 1 (see the Rockall Structural Elements map) but did not detect significant sedimentary infill, perhaps because of the masking effect of Palaeogene lavas. The modelled basin can be correlated with an intermediate wavelength magnetic low upon which are superimposed shorter wavelength anomalies that could be associated with shallow volcanic rocks.

A further small basin (**RHB2**) is delineated on the Rockall High, extending about 80 km north-west of the Conall Basin. This feature appears as an upper-crustal, low velocity zone at the north-western end of the RAPIDS 33 profile (Figure 28; Mackenzie et al. 2002a; Morewood et al., 2005). There is a degree of correlation with magnetic features, especially between a modelled basement high and a magnetic anomaly at 16.2°W 55.6°N.

The Ciarán Basin (**CIAB**) is a faulted Mesozoic basin on the north-western flank of the Rockall Basin which was identified on seismic line WI-32 by Naylor et al. (1999). Lack of data prevented the delineation of its shape from seismic data, but the 3D modelling suggests that its northern margin has an east-west orientation while the faulted basement high on its south-eastern side has a north-eastward trend. The magnetic images suggest that a north-westward continuation of one of the Barra volcanic ridges extends across the basin just west of WI-32.

The structural element map of Naylor et al. (1999) indicates buried Mesozoic fault blocks (**BMF**) in the area north-east of the Ciarán Basin, and the 3D model suggests that these lie parallel to the north-eastward trend of the postulated basin to the north-west (**RHB1**). However, the magnetic evidence is equivocal, indicating that the modelled structures should be treated with caution. The edge of the Rockall High to the north-west of this zone has a distinct magnetic signature, indicative of magnetic basement, but the modelled basement highs to the south-east are not associated with the positive magnetic anomalies that would be expected on this basis (compare the forward-modelled and observed magnetic fields). It is possible that structural highs

are formed of non-magnetic basement, but further seismic corroboration is required before these features can be identified with any confidence.

The modelled form of the Conall Basin (**CNB**) is more arcuate than suggested by Naylor et al. (1999) and this is supported by the magnetic evidence (compare the observed (Figure 4) and forward-modelled (Figure 35) magnetic field over this feature). The southern side of this basin lies on the South Hatton Lineament of Kimbell et al. (2005), which may be responsible for the structural disruption in this area.

The geometry interpreted for the Rónán Basin (**ROB**) is similar to that mapped by Naylor et al. (1999). The basin tapers south-westwards towards a minimum width at about 14.5°W 56.2°N and then broadens into a compartment situated between this basin and the Conall Basin. The magnetic evidence shows that the Ladra High is highly magnetic and it appears that relatively shallow basement extends 20 – 30 km to the south-east of the axis of this feature, although probably not as shallow as indicated by the model (the forward-calculated magnetic anomaly is more pronounced than the observed).

A modelled basin on the Rockall High just north of the median line (**RHB3**) has an identical trend to the Rónán Basin and may thus be a faulted Mesozoic basin beneath the Palaeogene basalts. Hitchen (2004) reports evidence for natural oil seeps along the northern margin of this basin and a separate set which align along a prolongation of the north-western margin of the Rónán Basin to the south. Another possible basin, of similar extent, lies 50 km to the east of RHB3 on the edge of the Rockall Basin. There is a reasonable correlation between these features and the magnetic anomaly pattern, particularly along the north-western margin of RHB3.

The geophysical signatures and modelling results over the Rockall Basin (**RB**) have been discussed in previous sections. The gravity and seismic data suggest that the crystalline crust beneath the axis of the basin is somewhat thicker than towards its flanks, and O'Reilly et al. (1995) has ascribed this to cooling and strengthening along this axis leading to outward migration of strain to the warmer margins (see also Bassi, 1995). The Hebrides Terrace (**HT**) and Anton Dohrn (**AD**) igneous centres are located on strands of the Anton Dohrn Lineament Complex of Kimbell et al. (2005), which acted as a transfer or accommodation zone between the northern and southern parts of the Rockall Basin. Comparison of the observed and forward-modelled magnetic fields shows that the subtle magnetic anomaly variations over the central part of the Rockall Basin to the south of these lineaments can be explained by modelled variations in the geometry of the underlying, thinned crystalline crust.

Naylor et al. (1999) map a Cenozoic compressional structure in the centre of the Rockall Basin (**RBC**; see the Rockall Basin Structural Element Map). A coincident magnetic anomaly, however, indicates that this is probably a volcanic structure. A magnetic anomaly can be traced in a south-southwestward direction from this feature towards the area to the west of the South Brona Basin where Norton (2002) identified a volcanic ridge in seismic reflection data.

The Barra Volcanic Ridge System (**BVRS**) in the southern part of the Rockall Basin comprises a series of arcuate ridges in the acoustic basement and are associated with strong magnetic anomalies (Bentley and Scrutton, 1987; Scrutton and Bentley, 1988). The ridges are considered to be extrusive volcanic edifices which were subsequently draped with sedimentary rocks until finally being overstepped by sediment in Eocene time (Scrutton and Bentley, 1988). The stratigraphic control does not allow them to be dated accurately but they may be of Early Cretaceous age, when there was also significant igneous activity in the Porcupine Basin and on the Labrador Margin (Scrutton and Bentley, 1988; Tate and Dobson, 1988; Balkwill, 1989; DeSilva, 1999). Although the seismically imaged ridges appear extrusive, modelling by Scrutton and Bentley (1988) indicated that the magnetic anomalies are best explained by a combination of the extrusive units and underlying intrusions, presumably lying along the fissures through which the igneous rocks were emplaced. The two most prominent ridges (in terms of their magnetic anomalies) correlate closely with the margins of a pronounced positive isostatic gravity anomaly (centred at about 17.5°W 53.5°N). This is accommodated in the 3D model by a zone of highly

stretched crystalline crust, presumably associated with the same extensional event that led to the magmatism, although lateral changes in crustal density are an alternative explanation (Scrutton and Bentley, 1988). The gravity anomalies indicate that the mass excess is held out of isostatic equilibrium, suggesting the possibility of strength during stretching with a relatively shallow depth of necking (Braun and Beaumont, 1989; Weissel and Karner, 1989).

The North Brona Basin (**NBB**) and South Brona Basin (**SBB**) are Mesozoic basins on the western side of the Porcupine High. The 3D model resolves their faulted eastern margins and also provides insights into the geometry of the structural highs that separate them from the Rockall Basin to the west. There is a magnetic anomaly over the high adjacent to the South Brona Basin but not over that to the west of the North Brona Basin. This is compatible with the pattern of magnetic anomalies over the basement further east, which indicates an E-W aligned magnetic low which projects towards the northern high. This could indicate a zone of less magnetic basement (e.g. a wedge of metasedimentary rocks).

The Cillian Basin (**CIB**) is a shallow graben lying to the east of the Brona Basins. Naylor et al. (1999) indicate a Cenozoic age but Haughton et al. (2005) ascribe a substantial proportion of the basin fill to the Cretaceous. The southern part of the basin is not well resolved by the 3D modelling, but the results do suggest that it extends about 30 km further to the north-west than is indicated in the map of Naylor et al. (1999). The east-north-east alignment of the northern margin of this extension suggests the possibility of an association with the Fairhead – Clew Bay Lineament (cf. Corfield et al., 1999).

The model indicates a further possible basin (**PHB**) on the Porcupine High between the Cillian and Macdara basins. The gravity feature on which this is based was identified by Corfield et al. (1999), who interpreted it to lie between splays of the Great Glen Fault. The interpretation by Naylor et al. (1999) of GSI Line 1 indicates only thin Cenozoic cover across the basin, implying a Mesozoic or older age, although the same authors imply that Cenozoic-Cretaceous strata may thicken across a fault further north which could be part of the faulted northern boundary of this basin (see Rockall or Porcupine structural element map). Recent evidence for lavas of Cretaceous age in this area (Haughton et al., 2005) might explain the difficulty in imaging deeper structure on seismic profiles. The basin can be correlated with a magnetic low, although the magnetic feature extends further to the west, suggesting that it may be due in part to intra-basement magnetisation contrasts or to the influence of relatively dense non-magnetic cover.

The Macdara Basin (**MDB**) lies on the north-western corner of the Porcupine High (Corfield et al., 1999; Naylor et al., 1999). The type section for this basin (GSR96-0114 in Naylor et al., 1999) suggests a thinner pre-Cenozoic sequence in the central part than towards its margins, and this is corroborated by the 3D model which indicates that the structures that define the northern side of the intrabasinal high have a more northerly trend than the fault which forms the southern margin of the basin.

The Colm Basin (**CMB**) is a shallow basin containing up to 0.5 s (TWT) of presumed Neogene strata (Naylor et al., 1999). A sharp gravity low with an E-W orientation just to the east of the mapped basin has generated a local sedimentary thickening in the 3D model. The reason for the gravity low is unknown. Its sharpness might be due to a data artefact, although the possibility of a small Mesozoic basin cannot be ruled out.

The model emphasises the linearity of the Erris Basin (**EB**), and comparison with the starting model reveals that the most strongly linear components were introduced by the gravity optimisation and thus provide an independent view of the fault architecture. The northern extension of the basin is offset north of 55.8°N and the southern limit of the basin occurs in an area of structural complexity where splays of the Great Glen Fault, and possibly also an extension of the South Hatton Lineament (Kimbell et al., 2005), appear to have influenced basin morphology. The gravity and magnetic modelling enable the Erris High (**EH**) to be traced over a distance of about 170 km, as far south as the basement high detected on WESTLINE (England and Hobbs, 1997).

The Slyne Basin (**SB**) is another strongly linear feature, particularly along its faulted western margin, and this accentuates the difference between its north-north-east trend and the north-east trend of the Erris Basin. The eastern margin of the basin appears faulted towards the north, close to the intersection with the Erris Basin, but more diffuse south of about 54°N, compatible with the seismic images presented by Dancer et al. (1999).

The Carboniferous basins to the west of Ireland – Donegal (**DB**), Mayo (**MB**) and Clare (**CLB**) - are not well-resolved by the 3D modelling. The density log for well 13/3-1 (Figure 8) in the Donegal Basin indicates a relatively high-density infill making gravity modelling difficult. The Donegal and Clare basins are not properly represented in the model, but an attempt has been made to accommodate the low density component of the Clare Basin, as delineated by a gravity low. The properties and modelling assumptions employed are, however, not well tuned for this target.

Some of the implications of the modelling for the structure and evolution of the Porcupine Basin (**PB**) have been discussed elsewhere in this report. The modelled pre-Cenozoic sedimentary thickness across the margins of the basin shows sharp inflections that are most probably related to fault zones. Comparison of the initial and optimised structure, particularly along the eastern margin of the basin, indicates that offsets between fault zones at the basin margin have been resolved from the gravity data and that these compare well with structure based on seismic interpretation (e.g. Naylor et al., 2002).

The Porcupine Median Volcanic Ridge (Tate and Dobson, 1988) can be identified by a reduction in the thickness of the pre-Cenozoic sediments and a coincident magnetic anomaly. The latter is best resolved by the residual magnetic anomaly image, which indicates that the anomaly terminates in the south at a hiatus at around 51°N (compare this image with the Porcupine-Goban Structural Element Map in the IPmmP GIS or Viewer). There are further magnetic anomalies to the south of this line, in the southern part of the Porcupine Basin (**PBS**), that are most probably due to additional components of the Porcupine Volcanic Ridge System (Naylor et al., 2002). These authors recognised two such ridges on the west side of the basin in seismic records but were unable to trace them southwards because of lack of data. The residual magnetic image reveals that the eastern of these two features is about 130 km long and extends southwards as far as the Lugh High (Masson and Miles, 1986; Naylor et al., 2002) at the mouth of the basin. Its trend swings from south-south-west to south-west in a southward direction and there is a close correlation between the feature and an axis in the optimised model of pre-Cenozoic thickness, with a distinct sedimentary thickening on its eastern side.

The Canice Basin (**CAB**) is a small faulted basin on the Porcupine High which was first identified by Tate (1992, 1993). The gravity imaging and modelling suggest that the thickest component of the basin is a graben just north of 51°N, which has a well-defined east-north-east trend and can be correlated with a magnetic low. A further apparent sedimentary thickening along an E-W axis 25 km to the south is probably an artefact of the inversion process, as it coincides with the flank of a gravity high and does not have a magnetic expression.

A number of authors (e.g. Lefort and Max, 1984; Masson and Miles, 1986; Readman et al., 2005) have highlighted the influence of north-west-trending lineaments on the Porcupine Basin. The linkage of features along a particular trend can be somewhat subjective, but there is reasonable support for certain of these features within the present results. For example the model reflects the influence of the Goban-Cockburn Fault zone (Smith, 1995) on the southern end of the Fastnet Basin (**FB**) and the Cockburn Basin (**COB**), and this can be extrapolated north-westward toward a zone of disruption on the east side of the Porcupine Basin. However, east-north-east-trending structures (locally expressed by the Balar Spur) are also implicated in the latter disruption (Naylor et al., 2002). There is also evidence for a north-west-trending feature linking the northern end of the Fastnet Basin to disruption of the eastern side of the Porcupine Basin just north of 51°N (this is the main lineament identified by Readman et al. (2005)). Possible correlatives of both features can be identified tentatively in gravity and magnetic

imagery on the west side of the Porcupine Basin. The evidence for north-west-trending structures influencing the Porcupine Basin further north is less convincing, as the primary structural controls here appear to have broadly east-west orientations.

An east-north-east structural trend is followed by the Goban Graben (**GG**; Dingle and Scrutton, 1979; Cook, 1987) and by a very clear lineament crossing the Goban Spur (**GSL**) about 30 km further south. The latter feature appears to mark a distinct discontinuity in the Pendragon Basin (thicker sediments to the south) and the northern limits of the Shackleton and Merlin basins (Naylor et al., 2002 and references therein). The basement high between this feature and the Goban Graben can be correlated with a distinct magnetic high, although the wavelength of the anomaly suggests that the magnetic basement lies at greater depth than the top basement surface in the gravity model.

A further strong lineament, this time with a north-east trend, occurs on the south side of the Goban Spur (**SGS**). This feature lies along the projection of the axis of the Fastnet Basin and is imaged very clearly by the isostatic gravity anomaly. The model attempts to simulate the gravity feature by a sharp increase in the thickness of the pre-Cenozoic sedimentary component. It is surprising that such a clear and undisturbed gravity trend is preserved when there are major cross-cutting structural and bathymetric features, and it is possible that this feature is due to an artefact in the original gravity data compilation.

The Western Approaches – North Armorican margin (**WANA**) was not a major target for this project, and it is likely the modelling is distorted here because of the disparity in resolution between the bathymetric and gravity data sources which was inferred from attempts to calculate isostatic gravity anomalies in this area (see Section 2.2.2). The optimised 3D model contains thicker sediments beneath local topographic highs and thinner sediments beneath local topographic lows. While such an effect might be expected, for example across canyons cutting down into a sedimentary layer, it is very much exaggerated in this case because the observed gravity effect of such local features has not been properly sampled. Details of the data distribution are not known but comparison with other compilations suggests that the gravity field is based on satellite data.

The model for the cover sequence emphasises the linear east-north-east-trending structural control over the North Celtic Sea Basin (**NCSB**), South Celtic Sea Basin (**SCSB**) and Western Approaches Basin (**WAB**). A similar trend is evident in the Variscan Haig Fras Granite (**HFG**; simulated by an artificial ‘basin’ in the model). This trend contrasts with north-east- to north-north-east-trending structural control which has influenced the Fastnet Basin (**FB**) and, to the north-east, the Kish Bank Basin (**KBB**), Central Irish Sea Basin (**CISB**), Peel Basin (**PB**) and Cardigan Bay Basin (**CBB**). The change in trend between the basins in the Celtic and Irish Seas could reflect the influence of the Variscan Front, but it is interesting to note a similar change in the trend of Caledonian features, including the Iapetus Suture, which swings from an east-north-east trend across the west of Ireland to a north-east trend across the east of Ireland and back to an east-north-east trend beneath mainland Britain (Figure 38; Phillips et al., 1976; McKerrow and Soper, 1989; Kimbell and Quirk, 1999). Kimbell and Stone (1995) and Kimbell and Quirk (1999) identified antecedents for these trends within the basement to the south of the Iapetus Suture beneath Britain. The east-north-east trend is followed, for example, by the Causey Pike Fault and Southern Borrowdales lineament of the Lake District, and the more northerly trend is followed by the Welsh Borderland Fault System and other basement structures beneath northern England and the Irish Sea. Kimbell and Quirk (1999) concluded that the basement structures with these trends may have been initiated during the late Precambrian – early Cambrian assembly of Avalonia at the northern margin of Gondwana, and that they were subsequently subject to multiple phases of Caledonian reactivation, including rifting at the margins of the Iapetus Ocean and compressional deformation associated with the closure of that ocean. If the Avalonian basement to the south of Ireland has a similar structural fabric this could have influenced Caledonian and Variscan deformation in this region which, in turn, established the

structural controls over subsequent basin evolution (cf. Bois et al., 1990; Ford et al., 1992; McCann and Shannon, 1992; McCann, 1996). The nature of the underlying continental basement may change in the extreme south-east of the study area, because the northern margin of the Western Approaches Basin appears to lie along the extension of the Rheic Suture, which marks the boundary between Avalonian and Cadomian basement formed by the closure of the Rheic Ocean in the late Silurian – early Devonian (Pharaoh, 1999 and references therein).

9 Conclusions and recommendations

The modelling methodology described by Kimbell et al. (2004) has been further developed and applied in order to produce a new three-dimensional lithospheric model for the Irish margin. It has been demonstrated that a more refined approach to defining the structure and properties of the cover sequence pays dividends in terms of the resolution and information content of the final model. An initial review of the modelling results suggests that they provide many new insights into the geometry of basins in this region, including examples of basins that have yet to be detected by seismic methods. Given the scope of the modelling, such a review will inevitably not have addressed all features of interest, and the long-term value of the results to the project sponsors should be as a reference source that can be compared and integrated with proprietary data.

One of the most challenging parts of the project was the construction of an initial digital 3D model for the cover sequence. An acceptable first-pass model was achieved but there is certainly scope for refinement. The more accurate the definition of the ‘known’ parts of the cover sequence, the better the resolution of the residual gravity anomalies attributable to the poorly understood parts. A digital compilation of structural horizons for this margin would be a valuable commodity in its own right, independent of its application in gravity modelling. This compilation could be constructed in such a way that it could be updated readily when new data became available, and its development might create a momentum by encouraging donations of data from companies who would in turn benefit from the regional overview provided. The next generation cover sequence model should certainly include a base Cretaceous interface as this would provide an important additional subdivision in terms of cover sequence structure and properties. The present results suggest that it is also a key interface in terms of the flexural development of the region, marking the transition from a time when the lithosphere was very weak to one in which flexural strength started to have some influence, at least in the deeper basins.

The results from the RAPIDS 4 and HADES seismic experiments should become available soon and will provide a valuable supplement to the deep seismic database for the region. As this database is enhanced it will become practicable to consider refining the regional 3D model on the basis of comparisons with such control. At present the Moho depth is simply referred to a user-defined ‘reference’ depth of 30 km. Improved seismic control could facilitate identification of patterns in the differences between seismic and model Moho which should allow refinement of this assumption including, if appropriate, lateral variations to reflect deep density changes that are not modelled explicitly.

The Hatton Basin area would certainly benefit from closer investigation. A seismic reflection survey has been conducted over the basin recently (2004) but the results were not available in time for the IPmmp modelling. The control over shallow structure provided by this survey together with the deep control from HADES should lead to better constrained gravity modelling. The magnetic signatures over the basin, and the contrasts between the magnetic expression of its northern and southern parts, also deserve further attention. The new seismic data, together with more detailed magnetic modelling, could be used to site boreholes to investigate the basement and igneous history of the area. In particular, it would be of great interest to sample the rocks beneath the linear magnetic and structural highs that characterise the southern part of the basin.

Appendix 1 Geophysical images

The following table provides details of the digital geophysical images that have been generated for the Irish Passive Margin Modelling Project and are included within the IPmmP GIS. These are contained in the folder `gis\geophys_images` in the accompanying CD-ROM. Where indicated, an image is available which shows the colour scale that applies to a particular display. These are stored in the `colour_scales` subfolder and are in tiff format, as this appears to offer the most flexibility for import into GIS layouts or for other annotation purposes.

File name	Description	Colour scale file name
<i>Gravity images:</i>		
faacn.jpg	Free-air gravity anomaly. Colour shaded-relief. Equal area colour. Illuminated from the north.	faa_cs.tif
faacv.jpg	Free-air gravity anomaly. Colour shaded-relief. Equal area colour. Vertical illumination.	faa_cs.tif
faaup10cn.jpg	Free-air gravity anomaly - upward continued by 10 km. Equal area colour. Illuminated from the north.	faaup10_cs.tif
faaup10rcn.jpg	Free-air gravity anomaly - 10 km continuation residual. Equal area colour. Illuminated from the north.	faaup10r_cs.tif
faahgcn.jpg	Scalar horizontal gradient of the free-air gravity anomaly. Equal area colour + shaded-relief. Illuminated from the north.	faahg_cs.tif
bacn.jpg	Bouguer gravity anomaly (reduction density = 2.20 Mg/m ³). Equal area colour + shaded-relief. Illuminated from the north.	ba_cs.tif
gisoscn.jpg	Isostatically corrected Bouguer anomaly. Equal area colour. Illuminated from the north.	gisos_cs.tif
gisoscv.jpg	Isostatically corrected Bouguer anomaly. Equal area colour. Vertical illumination.	gisos_cs.tif
faan.jpg	Free-air gravity anomaly. Grey-scale shaded-relief. Illuminated from the north.	—
faanw.jpg	Free-air gravity anomaly. Grey-scale shaded-relief. Illuminated from the northwest.	—
faane.jpg	Free-air gravity anomaly. Grey-scale shaded-relief. Illuminated from the northeast.	—
faaw.jpg	Free-air gravity anomaly. Grey-scale shaded-relief. Illuminated from the west.	—
faae.jpg	Free-air gravity anomaly. Grey-scale shaded-relief. Illuminated from the east.	—
faasw.jpg	Free-air gravity anomaly. Grey-scale shaded-relief. Illuminated from the southwest.	—
faase.jpg	Free-air gravity anomaly. Grey-scale shaded-relief. Illuminated from the southeast.	—
faas.jpg	Free-air gravity anomaly. Grey-scale shaded-relief. Illuminated from the south.	—
faav.jpg	Free-air gravity anomaly. Grey-scale shaded-relief. Vertical illumination.	—
<i>Magnetic images:</i>		
magcn.jpg	Total magnetic field. Colour shaded-relief. Equal area colour. Illuminated from the north.	mag_cs.tif
magcv.jpg	Total magnetic field. Colour shaded-relief. Equal area colour. Vertical illumination.	mag_cs.tif
rtpcn.jpg	Reduced-to-pole magnetic field. Colour shaded-relief. Equal area colour. Illuminated from the north.	rtp_cs.tif
rtpcv.jpg	Reduced-to-pole magnetic field. Colour shaded-relief. Equal area colour. Vertical illumination.	rtp_cs.tif
rtpup10cn.jpg	Reduced-to-pole magnetic field - upward continued by 10 km. Equal area colour. Illuminated from the north.	rtpup10_cs.tif

File name	Description	Colour scale file name
rtpup10rcn.jpg	Reduced-to-pole magnetic field - 10 km continuation residual. Equal area colour. Illuminated from the north.	rtpup10r_cs.tif
maghgcn.jpg	Scalar horizontal gradient of the total magnetic field. Equal area colour + shaded-relief. Illuminated from the north.	maghg_cs.tif
pseudcn.jpg	Pseudogravity field. Colour shaded-relief. Equal area colour. Illuminated from the north.	pseud_cs.tif
pseudcv.jpg	Pseudogravity field. Colour shaded-relief. Equal area colour. Vertical illumination.	pseud_cs.tif
pseudhgcn.jpg	Horizontal gradient of pseudogravity. Colour shaded-relief. Equal area colour. Illuminated from the north.	pseudhg_cs.tif
magn.jpg	Total magnetic field. Grey-scale shaded-relief. Illuminated from the north.	—
magnw.jpg	Total magnetic field. Grey-scale shaded-relief. Illuminated from the northwest.	—
magne.jpg	Total magnetic field. Grey-scale shaded-relief. Illuminated from the northeast.	—
magw.jpg	Total magnetic field. Grey-scale shaded-relief. Illuminated from the west.	—
mage.jpg	Total magnetic field. Grey-scale shaded-relief. Illuminated from the east.	—
magsw.jpg	Total magnetic field. Grey-scale shaded-relief. Illuminated from the southwest.	—
magse.jpg	Total magnetic field. Grey-scale shaded-relief. Illuminated from the southeast.	—
mags.jpg	Total magnetic field. Grey-scale shaded-relief. Illuminated from the south.	—
magv.jpg	Total magnetic field. Grey-scale shaded-relief. Vertical illumination.	—
<i>Topographic images:</i>		
topocn.jpg	Bathymetry/topography. Colour shaded-relief. Adapted colour scale. Illuminated from the north.	topo_cs.tif
topon.jpg	Bathymetry/topography. Grey-scale shaded-relief. Illuminated from the north.	—
topov.jpg	Bathymetry/topography. Grey-scale shaded-relief. Vertical illumination.	—
topocont.jpg	Colour contour bathymetric map (cf. Figure 5 of this report). Contours are at 500 m intervals and there is a colour scale in the bottom left-hand corner of the map.	—

Appendix 2 Base data and structural data within the GIS

The table below lists the GIS layers in the 'Base data' and 'Tectonic' categories within the IPmmP GIS.

File name	Description
<i>Base data:</i>	
study_area.shp	Study area for the Irish Passive Margins Modelling Project (IPmmP)
irish_desig_area.shp	Irish Designated Area. Shapefile previously generated for the Petroleum Infrastructure Project and supplied to the Irish Passive Margin Modelling Project in September 2004.
coast.shp	Coastline based on World Vector Shoreline. Previously generated for the Petroleum Infrastructure Project and supplied to the Irish Passive Margin Modelling Project in September 2004.
coast_ply.shp	Coastline based on World Vector Shoreline. Previously generated for the Petroleum Infrastructure Project and supplied to the Irish Passive Margin Modelling Project (IPmmP) in September 2004. Irish and UK landmass converted to polygons by IPmmP.
wells_props.shp	Wells in Irish Waters used in the physical property analysis conducted by the Irish Passive Margin Modelling Project (IPmmP). Shapefile previously generated for the Petroleum Infrastructure Project from Petroleum Affairs Division data and supplied to IPmmP on 20 September 2004.
wells00.shp	Wells in Irish waters. Shapefile previously generated for the Petroleum Infrastructure Project from Petroleum Affairs Division data and supplied to the Irish Passive Margin Modelling Project in September 2004.
dspdpsites.shp	Deep Sea Drilling Program sites downloaded from www-odp.tamu.edu . Shapefile created by Dr Sebastian Luening.
opdsites.shp	Ocean Drilling Program sites downloaded from www-odp.tamu.edu . Shapefile created by Dr Sebastian Luening.
deep_seismic.shp	Locations of deep seismic profiles (approximate)
latlon_5deg.shp	Lat-lon graticule at 5 degree intervals
latlon_1deg.shp	Lat-lon graticule at 1 degree intervals
pipmap04_scan.jpg	Scan of the Petroleum Infrastructure Project (PIP) Database Map published in 2004.
<i>Structural data:</i>	
pip_rockall_struc.jpg	Georeferenced version of the structural nomenclature map contained in: Naylor, D, Shannon, P, and Murphy, N. 1999. Irish Rockall Basin region - a standard structural nomenclature system. Petroleum Affairs Division, Special Publication 1/99.
pip_porcupine_struc.jpg	Georeferenced version of the structural nomenclature map contained in: Naylor, D, Shannon, P, and Murphy, N. 2002. Porcupine-Goban region - a standard structural nomenclature system. Petroleum Affairs Division, Special Publication 1/02.
igneous_centres.shp	Locations of igneous centres
cont_ocean_boundary.shp	Continent-ocean boundary assumed in the modelling
ocean_age	Grid of ages of oceanic crust (after Müller et al., 1997)

Appendix 3 Model data within the GIS

The following layers have been incorporated in the GIS to enable users to interrogate the results of the 3D modelling. The model components are provided as grids and the fields are provided as images. Shapefiles of contour overlays for the grids are also included, and have filenames of the form gridfile_conts.shp. The grid node spacing is 2 km, except in the case of the flexural models, which employed a 4 km interval.

File	Description
<i>Optimised model:</i>	
coverthk_opt	Optimised cover sequence thickness (km)
precenthk_opt	Optimised thickness of pre-Cenozoic (pre-lava) sedimentary rocks (km)
cryst_opt	Optimised thickness of crystalline crust (km)
moho_opt	Optimised depth to Moho (km)
exfac_opt	Apparent extension factor calculated from optimised model
loadanom_opt	Apparent load anomaly (MPa) calculated from optimised model
calcg_opt.jpg	Image of the calculated field (Free-air gravity anomaly) over the optimised model (same imaging parameters as faacn.jpg of Appendix 1)
resg_opt.jpg	Image of residual gravity anomalies over the optimised model (colour scale as in Figure 25 in this report)
model_features.shp	Labelled features referred to in the discussion in Section 8.5 of this report and in the IPmmp Viewer
<i>Initial model:</i>	
centhk	Thickness of Cenozoic (post-lava) sedimentary rocks (km)
lavathk	Nominal thickness of Palaeogene lavas in the Hatton-Rockall area (km)
precen_init	Initial thickness of pre-Cenozoic (pre-lava) sedimentary rocks (km)
denude	Assumed denudation of the pre-Cenozoic layer
<i>Magnetic modelling:</i>	
calcm_initisos.jpg	Image of the calculated total magnetic field over the initial isostatic model (same imaging parameters as magcn.jpg of Appendix 1)
calcm_opt.jpg	Image of the calculated total magnetic field over the optimised model (same imaging parameters as magcn.jpg of Appendix 1)
calcm_opt_up10.jpg	Image of the calculated total magnetic field over the optimised model after upward continuation by 10 km
obsm_opt_up10.jpg	Image of the observed total magnetic field after upward continuation by 10 km
<i>Flexural modelling:</i>	
calcg_isos.jpg	Image of the calculated free-air gravity anomaly over a model in isostatic equilibrium.
calcg_all_te5.jpg	Image of the calculated free-air gravity anomaly over a model assuming $T_e = 5$ km throughout the deposition of the cover sequence.
calcg_all_te10.jpg	Image of the calculated free-air gravity anomaly over a model assuming $T_e = 10$ km throughout the deposition of the cover sequence.
calcg_all_te15.jpg	Image of the calculated free-air gravity anomaly over a model assuming $T_e = 15$ km throughout the deposition of the cover sequence.
calcg_all_te20.jpg	Image of the calculated free-air gravity anomaly over a model assuming $T_e = 20$ km throughout the deposition of the cover sequence.
load_all_te5	Load anomaly (MPa) of a model assuming $T_e = 5$ km throughout the deposition of the cover sequence.

File	Description
load_all_te10	Load anomaly (MPa) of a model assuming $T_e = 10$ km throughout the deposition of the cover sequence.
load_all_te15	Load anomaly (MPa) of a model assuming $T_e = 15$ km throughout the deposition of the cover sequence.
load_all_te20	Load anomaly (MPa) of a model assuming $T_e = 20$ km throughout the deposition of the cover sequence.
calcg_cen_te5.jpg	Image of the calculated free-air gravity anomaly over a model assuming $T_e = 5$ km during Cenozoic sediment loading.
calcg_cen_te10.jpg	Image of the calculated free-air gravity anomaly over a model assuming $T_e = 10$ km during Cenozoic sediment loading.
calcg_cen_te15.jpg	Image of the calculated free-air gravity anomaly over a model assuming $T_e = 15$ km during Cenozoic sediment loading.
calcg_cen_te20.jpg	Image of the calculated free-air gravity anomaly over a model assuming $T_e = 20$ km during Cenozoic sediment loading.
load_cen_te5	Load anomaly (MPa) of a model assuming $T_e = 5$ km during Cenozoic sediment loading.
load_cen_te10	Load anomaly (MPa) of a model assuming $T_e = 10$ km during Cenozoic sediment loading.
load_cen_te15	Load anomaly (MPa) of a model assuming $T_e = 15$ km during Cenozoic sediment loading.
load_cen_te20	Load anomaly (MPa) of a model assuming $T_e = 20$ km during Cenozoic sediment loading.
<i>All the calculated fields for the flexural models use the same colour scale as faacn.jpg (Appendix 1).</i>	

In addition to the GIS versions, the accompanying CD-ROM contains grids of the initial and optimised models in a simple ASCII xyz (Unix) format, which can be found in the gis\xyz_files folder. Horizontal co-ordinates in these files are referred to UTM Zone 28 (ED50), and thicknesses are in kilometres. Null values are indicated by '1e+20' in the z field.

Appendix 4 Velocity-depth relationships

This Appendix sets out some approximations for relationships between velocity, two-way travel time and depth in sedimentary rocks in the Irish Passive Margins Modelling Project study area. They relate to shale-dominated sequences, so the depth-conversion will be distorted by the presence of other lithologies (e.g. lavas and sills) within the cover sequence.

First assume that velocity within the cover sequence varies linearly with two-way-time:

$$v = v_0 + kt \quad (1)$$

Where:

- t = two-way travel time (below sea bed)
- v = sediment velocity at depth represented by t
- v₀ = sediment velocity at sea bed
- k = a constant

The average velocity and depth can then be calculated by:

$$v_{ave} = v_0 + kt/2 \quad (2)$$

$$d = v_0t/2 + kt^2/4 \quad (3)$$

Where:

- v_{ave} = the time-averaged velocity between the sea bed and t
- d = depth below sea bed at time t

Expression (3) thus provides a straightforward means of converting from two-way time to depth in normally compacted sedimentary rocks.

Substituting (1) into (3) gives a velocity-depth relationship that can be tested against velocity profiles from well logs and wide-angle experiments:

$$v = (v_0^2 + 4kd)^{1/2} \quad (4)$$

For a sedimentary package lying between two-way times t₁ and t₂ below sea bed, the following expressions apply:

$$v_{12} = v_0 + k(t_1+t_2)/2 \quad (5)$$

$$z_{12} = v_0(t_2-t_1)/2 + k(t_2^2-t_1^2)/4 \quad (6)$$

Where:

- v₁₂ = time-averaged velocity between t₁ and t₂
- z₁₂ = sediment thickness between t₁ and t₂

Abnormal velocities will occur if sequences are overcompacted as a result of uplift and erosion. Initial estimates of appropriate parameters have therefore been based on well logs from areas where there is less likelihood of such effects. For example, thermal history studies on samples from well 35/8-2 indicate that these rocks are currently at their maximum post-depositional temperature and that there is no evidence of removed section, an interpretation that is compatible with the lack of unconformities within the sequence (Green, 2002). In order to extend the comparison to normally compacted rocks at shallow depths, the velocity log for this well is plotted together with the velocity log from ODP borehole 982B (Hatton Basin) in Figure 10. This figure also includes some velocity models from the central part of the Rockall Basin derived from wide-angle seismic experiments.

Figure 10 illustrates an empirical velocity-depth relationship based on the following parameters:

$$v_0 = 1.6 \text{ km/s}$$

$$k = 0.95$$

Which when inserted in (1)-(4) above gives:

$$v = 1.6 + 0.95t$$

$$v_{ave} = 1.6 + 0.475t$$

$$d = 0.8t + 0.2375t^2$$

$$v = (2.56 + 3.8d)^{1/2}$$

Where v is in km/s, d is in km and t is in seconds.

With these parameters there is a reasonable fit both with the well log data (except between 2.0 km and 2.7 km in 35/8-2, where calcareous rocks are present) and with the velocity model derived from ESP-12 by Joppen and White (1990) (Figure 10). It is also comparable to the RAPIDS 3 models (Mackenzie et al., 2002a, b) at shallower depths, but not deeper within the sedimentary section where the RAPIDS data indicate higher velocities.

Influence of uplift and erosion

The empirical velocity trend described above can be compared with velocity data from other wells to identify evidence of overcompaction. It is possible to provide quantitative estimates of the thickness of any removed section by computing the depth shift which, when applied to the velocity log, provides the best fit with the empirical curve. This has been attempted in an automated fashion on all the wells being analysed by IPmmP, and the results are broadly comparable with those resulting from a similar approach based on density data (see section 6.4 in main report). Noise is introduced by using the full logs, however, because of the effects of different lithologies, caving etc., so a more careful approach based on selected log segments is recommended to constrain the estimates of removed overburden more accurately.

It is necessary to modify the two-way time to depth conversion formula (3) in regions that have undergone uplift and erosion, and this involves dividing the sedimentary sequence if normally compacted sediments have been deposited on top of an overcompacted layer. The calculation sequence is:

- (i) Use expression (3) to compute the depth below sea bed of the top of the overcompacted section from the two-way travel time (t_1).
- (ii) Increase this depth by an amount equal to the estimated denudation at the location (Figure 17), and insert this value in (4) to get the velocity at the top of the overcompacted section (v_1).
- (iii) Calculate the velocity at the bottom of the overcompacted section (v_2) at two-way time t_2 using (1) [$v_2 = v_1 + k(t_2 - t_1)$]
- (iv) Recompute the thickness of the overcompacted section (z_{12}) from the average velocity and two-way time interval [$z_{12} = (v_1 + v_2)(t_2 - t_1)/4$].
- (v) Reconstruct the sedimentary sequence in depth by placing this unit beneath the base of the normally compacted component, as computed in (i).

Reversing the procedure

It is also possible to perform the reverse operation on the sediment thickness maps produced as a result of the gravity inversion, i.e. generate theoretical two-way time maps from the computed

sediment thickness. In normally compacted components, two-way time can be expressed in terms of depth by solving equation (3) for t:

$$t = ((v_0^2 + 4kd)^{1/2} - v_0) / k \quad (7)$$

If the unit has been uplifted and eroded, the velocities at its top and bottom can be calculated using (4), with the depths incremented by the appropriate uplift. The thickness in two-way time of the unit can then be calculated by dividing its true thickness (in km) by the average of these velocities and multiplying by 2.

Limitations on use

The approximations described above are not applicable when the sedimentary thickness is very large. They give acceptable results up to about 4 s TWT (7 km sediment thickness) but progressively overestimate the thickness at greater times and certainly should not be used when more than 10 km of sediment is present. Note that it is the sum of present day sediment thickness and the removed section that needs to be kept within these constraints. The programs which have been used to implement these approximations in the present project avoid excessive depth estimates by ‘capping’ the velocity estimates, for example in steps (i) and (iii) in the above sequence, at a maximum value of 5.7 km/s (an assumed velocity for a mudrock with zero porosity).

Appendix 5 Alphabetical list of model features

The following abbreviations have been applied in annotations included in the IPmmP GIS and Model Viewer, and are referred to in the discussion in Section 8.5

Code	Feature
A	Aramassa igneous centre
AD	Anton Dohrn igneous centre
BMF	Buried Mesozoic fault blocks
BVRS	Barra Volcanic Ridge System
CAB	Canice Basin
CBB	Cardigan Bay Basin
CIAB	Ciarán Basin
CIB	Cillian Basin (NNE extension?)
CISB	Central Irish Sea Basin
CLB	Clare Basin
CM	Continental margin
CMB	Colm Basin
CNB	Connall Basin
COB	Cockburn Basin
COLB	Colmán Basin
DB	Donegal Basin
EB	Erris Basin
EH	Erris High
FB	Fastnet Basin
FH	Fangorn High
GG	Goban Graben
GL	GEUS line 3
GSL	ENE-trending lineament on Goban Spur
HFG	Haig Fras Granite
HRBN	Hatton Ridge Basin (N)
HRBS	Hatton Ridge Basin (S)
HT	Hebrides Terrace igneous centre
KBB	Kish Bank Basin
M	Mentone igneous centre
MB	Mayo Basin
MDB	Macdara Basin
NBB	North Brona Basin
NCSB	North Celtic Sea Basin
NHB	Northern Hatton Basin
O	Owlsgard igneous centre
PB	Porcupine Basin

PBS	Porcupine Basin (S)
PEB	Peel Basin
PHB	Possible basin on Porcupine High
R	Rohan igneous centre
RB	Rockall Basin
RBC	Rockall Basin - compressional or igneous feature?
RHB1	Possible basin on Rockall High (1)
RHB2	Possible basin on Rockall high (2)
RHB3	Possible basin on Rockall High (3)
RMF	Reversely magnetised feature adjacent to Fangorn High
ROB	Rónán Basin (/ Ladra High)
SB	Slyne Basin
SBB	South Brona Basin
SCSB	South Celtic Sea Basin
SDR	Seaward-dipping reflectors
SE	Sandastre igneous centre
SEB	S side of Edoras Bank
SGS	NE-trending gravity minimum S of Goban Spur
SHB	Southern Hatton Basin
SO	Sandarro igneous centre
WAB	Western Approaches Basin
WANA	Western Approaches - North Armorican margin

References

- ALLEN, P A, BENNETT, S D, CUNNINGHAM, M J M, CARTER, A, GALLAGHER, K, LAZZARETTI, E, GALEWSKY, J, DENSMORE, A L, PHILLIPS, W E A, NAYLOR, D, AND SOLLA HACH, C. 2002. The post-Variscan thermal and denudational history of Ireland. 371-399 in *Exhumation of the North Atlantic margin: Timing, Mechanisms and Implications for Petroleum Exploration*. DORÉ, A G, CARTWRIGHT, J A, STOKER, M S, TURNER, J P, and WHITE, N J (editors). *Special Publication of the Geological Society, London*, No. 196.
- ARCHER, S G, BERGMAN, S C, ILIFFE, J, MURPHY, C M, and THORNTON, M. 2005. Palaeogene igneous rocks reveal new insights into the geodynamic evolution and petroleum potential of the Rockall Trough, NE Atlantic Margin. *Basin Research*, Vol. 17, 171-201.
- BALKWILL, H R. 1987. Labrador Basin: structural and stratigraphic style. *Memoir of the Canadian Society of Petroleum Geologists*, No. 12, 17-43.
- BARTON, A J, and WHITE R S. 1997a. Crustal structure of Eboras Bank continental margin and mantle thermal anomalies beneath the North Atlantic. *Journal of Geophysical Research*, Vol. 102, B2, 3109-3129.
- BARTON, A J, and WHITE, R S. 1997b. Volcanism on the Rockall continental margin. *Journal of the Geological Society, London*, Vol. 154, 531-536.
- BASSI, G. 1995. Relative importance of strain rate and rheology for the mode of continental extension. *Geophysical Journal International*, **122**, 195-210.
- BENTLEY, P A D, and SCRUTTON, R A. 1987. Seismic investigations into the basement structure of southern Rockall Trough. 667-675 in *Petroleum Geology of Northwest Europe: Proceedings of the 3rd Conference*. BROOKS, J and GLENNIE, K W (editors). (London: The Geological Society.)
- BOIS, C, LEFORT, J-P, LE GALL, B, SIBUET, J-C, GARIEL, O, PINET, B, and CAZES, M. 1990. Superimposed Variscan, Caledonian and Proterozoic features inferred from deep seismic profiles recorded between southern Ireland, southwestern Britain and western France. *Tectonophysics*, Vol. 177, 15-37.
- BOLDREEL, L O, and ANDERSEN, M S. 1994. Tertiary development of the Faroe-Rockall Plateau based on seismic reflection data. *Bulletin of the Geological Society of Denmark*, Vol. 41, 169-180.
- BONNEVILLE, A, and CAPOLSINI, P. 1999. THERMIC: a 2-D finite-element tool to solve conductive and advective problems in Earth Sciences. *Computers and Geosciences*, Vol. 25 1137-1148.
- BRAUN, J, and BEAUMONT, C. 1989 A physical explanation of the relation between flank uplifts and the break-unconformity at rifted continental margins. *Geology*, Vol. 17, 760-764.
- BREIVIK, A J, VERHOEF, J, and FALEIDE, J I. 1999. Effect of thermal contrasts on gravity modelling at passive margins: results from the western Barents Sea. *Journal of Geophysical Research*, Vol. 104, 15293-15311.
- BULL, J M, and MASSON, D G. 1996. The southern margin of the Rockall Plateau: stratigraphy, Tertiary volcanism and plate tectonic evolution. *Journal of the Geological Society, London*, Vol. 153, 601-612.
- BUNCH, A W H. 1979. A detailed seismic structure of Rockall Bank (55°N, 15°W) - a synthetic seismogram analysis. *Earth and Planetary Science Letters*, Vol. 45, 453-463.
- CHADWICK, R A, JACKSON, D I, BARNES, R P, KIMBELL, G S, JOHNSON, H, CHIVERRELL, R C, THOMAS, G S P, JONES, N S, RILEY, N J, PICKETT, E A, YOUNG, B, HOLLIDAY, D W, BALL, D F, MOLYNEUX, S G, LONG, D, POWER, G M and ROBERTS, D H. 2001. Geology of the Isle of Man and its offshore area. *British Geological Survey Research Report*, RR/01/06.
- CHAPMAN, T J, BROKS, T M, CORCORAN, D V, DUNCAN, L A, and DANCER, P N. 1999. The structural evolution of the Erris Trough, offshore northwest Ireland, and implications for hydrocarbon generation. 455-469 in *Petroleum Geology of Northwest Europe: Proceedings of the 5th Conference*. FLEET, A J, and BOLDY, S A R (editors). (London: The Geological Society.)
- CONROY, J J, and BROCK, A. 1989. Gravity and magnetic studies of crustal structure across the Porcupine basin west of Ireland. *Earth and Planetary Science Letters*, Vol. 93, 371-376.
- COOK, D R. 1987. The Goban Spur - exploration in a deep water frontier basin. 623-632 in *Petroleum Geology of North West Europe*. Brooks, K, and Glennie, KW. (editors). (London: Graham and Trotman.)
- CORFIELD, S, MURPHY, N, and PARKER, S. 1999. The structural and stratigraphic framework of the Irish Rockall Trough. 407-420 in *Petroleum Geology of Northwest Europe: Proceedings of the 5th Conference*. FLEET, A J, and BOLDY, S A R (editors). (London: The Geological Society.)
- CROKER, P F. 1995. The Clare Basin; a geological and geophysical outline. 327-339 in *The Petroleum Geology of Ireland's Offshore Basins*. CROKER, P F, and SHANNON, P M (editors). *Special Publication of the Geological Society, London*, No. 93.
- DABEK, Z K and WILLIAMSON, J P. 1999. Forward and inverse wavenumber formulae for the gravity and magnetic responses of layered models. *British Geological Survey Technical Report* WK/99/03C.

- DANCER, P N, ALGAR, S T, and WILSON, I R. 1999. Structural evolution of the Slyne Trough. 445-453 in *Petroleum Geology of Northwest Europe: Proceedings of the 5th Conference*. FLEET, A J, and BOLDY, S A R (editors). (London: The Geological Society.)
- DESILVA, N R. 1999. Sedimentary basins and petroleum systems offshore Newfoundland and Labrador. 501-515 in *Petroleum Geology of Northwest Europe: Proceedings of the 5th Conference*. FLEET, A J, and BOLDY, S A R (editors). (London: The Geological Society.)
- DICKIN, A P. 1992. Evidence for an Early Proterozoic crustal province in the North Atlantic region. *Journal of the Geological Society, London*, Vol. 149, 483-486.
- DINGLE, R V, and SCRUTTON, R A. 1979. Sedimentary succession and tectonic history of a marginal plateau (Goban Spur, south-west of Ireland). *Marine Geology*, Vol. 33, 45-69.
- DORÉ, A G, CARTWRIGHT, J A, STOKER, M S, TURNER, J P, and WHITE, N (editors). 2002a. Exhumation of the North Atlantic margin: Timing, Mechanisms and Implications for Petroleum Exploration. *Special Publication of the Geological Society, London*, No. 196.
- DORÉ, A G, CORCORAN, D V, AND SCOTCHMAN, I C. 2002b. Prediction of the hydrocarbon system in exhumed basins, and application to the NW European margin. 401-429 in *Exhumation of the North Atlantic margin: Timing, Mechanisms and Implications for Petroleum Exploration*. DORÉ, A G, CARTWRIGHT, J A, STOKER, M S, TURNER, J P, and WHITE, N (editors). *Special Publication of the Geological Society, London*, No. 196.
- DUNFORD, G M, DANCER, P N, and LONG, K D. 2001. Hydrocarbon potential of the Kish Bank Basin: integration within a regional model for the greater Irish Sea Basin. 135-154 in *The Petroleum Exploration of Ireland's Offshore Basins*. SHANNON, P M, HAUGHTON, P D W, and CORCORAN, D V (editors). *Special Publication of the Geological Society, London*, No. 188.
- EDWARDS, J W F. 2002. Development of the Hatton-Rockall Basin, north-east Atlantic Ocean. *Marine and Petroleum Geology*, Vol. 19, 193-205.
- ELLIS, D, BELL, B R, JOLLEY, D W, and O'CALLAGHAN, M. 2002. The stratigraphy, environment of eruption and age of the Faroes Lava Group, NE Atlantic Ocean. 253-269 in *The North Atlantic Igneous Province: Stratigraphy, Tectonic, Volcanic and Magmatic Processes*. JOLLEY, D W and BELL, B R (editors). *Special Publication of the Geological Society, London*, No. 197.
- ENGLAND, R W, and HOBBS, R W. 1997. The structure of the Rockall Trough imaged by deep seismic reflection profiling. *Journal of the Geological Society, London*, Vol. 154, 497-502.
- EVANS, C D R, HILLIS, R R, GATLIFF, R W, DAY, G A, and EDWARDS, J W F. 1990. *United Kingdom offshore regional report: the geology of the western English Channel and its western approaches*. (London: HMSO for the British Geological Survey.)
- FLOODPAGE, J, NEWMAN, P, and WHITE, J. 2001. Hydrocarbon prospectivity in the Irish Sea area; insights from recent exploration of the Central Irish Sea, Peel and Solway basins. 107-134 in *The Petroleum Exploration of Ireland's Offshore Basins*. SHANNON, P M, HAUGHTON, P D W, and CORCORAN, D V (editors). *Special Publication of the Geological Society, London*, No. 188.
- FORD, M, KLEMPERER, S L, and RYAN, P D. 1992. Deep structure of southern Ireland: a new geological synthesis using BIRPS deep reflection profiling. *Journal of the Geological Society, London*, Vol. 149, 915-922.
- FYFE, J A, LONG, D, EVANS, D, and ABRAHAM, D A. 1993. *United Kingdom offshore regional report: the geology of the Malin-Hebrides Sea area*. (London: HMSO for the British Geological Survey.)
- GREEN, P F. 2002. Thermal history reconstruction in Porcupine Basin wells 26/28-1 and 35/8-2 based on AFTA[®], VR and fluid inclusion data. Petroleum Infrastructure Project, Porcupine Studies Group Report 00/22.
- HAUGHTON, P, PRAEG, D, SHANNON, P, HARRINGTON, G, HIGGS, K, AMY, L, TYRRELL, S, and MORRISSEY, T. 2005. First results from shallow stratigraphic boreholes on the eastern flank of the Rockall Basin, offshore western Ireland. 1077-1094 in *Petroleum Geology: North-West Europe and Global Perspectives - Proceedings of the 6th Petroleum Geology Conference*. DORÉ, A G and VINING, B (editors). (London: The Geological Society.)
- HAUSER, F, O'REILLY, B M, JACOB, A W B, SHANNON, P M, MAKRISS, J, and VOGT, U. 1995. The crustal structure of the Rockall Trough: differential stretching without underplating. *Journal of Geophysical Research*, Vol. 100, 4097-4116.
- HILLIS, R. 1995. Regional Tertiary exhumation in and around the United Kingdom. 167-190 in *Basin Inversion*. BUCHANAN, J G, and BUCHANAN, P G (editors). *Special Publication of the Geological Society, London*, No. 88.
- HITCHEN, K. 2004. The geology of the UK Hatton-Rockall margin. *Marine and Petroleum Geology*, Vol. 21, 993-1012.
- HORSEFIELD, S J, WHITMARSH, R B, WHITE, R S, AND SIBUET, J-C. 1992. Crustal structure of the Goban Spur rifted continental margin, NE Atlantic. *Geophysical Journal International*, Vol. 119, 1-19.
- IOC, IHO and BODC, 2003. *Centenary Edition of the GEBCO Digital Atlas*. Published on CD-ROM on behalf of the Intergovernmental Oceanographic Commission and the International Hydrographic Organization as part of the General Bathymetric Chart of the Oceans. (British Oceanographic Data Centre, Liverpool.)
- IZATT, C, MAINGARM, S, and RACEY, A. 2001. Fault distribution and timing in the Central Irish Sea Basin. 155-169 in *The Petroleum Exploration of Ireland's Offshore Basins*. SHANNON, P M, HAUGHTON, P D W, and CORCORAN, D V (editors). *Special Publication of the Geological Society, London*, No. 188.
- JOHNSON, H, RITCHIE, J D, GATLIFF, R W, WILLIAMSON, J P, CAVILL, J and BULAT, J. 2001. Aspects of the structure of the Porcupine and Porcupine Seabight basins as revealed from gravity modelling of regional seismic transects. 265-274 in *The*

Petroleum Exploration of Ireland's Offshore Basins. SHANNON, P M, HAUGHTON, P D W, and CORCORAN, D V (editors). *Special Publication of the Geological Society, London*, No. 188.

JOPPEN, M and WHITE, R S. 1990. The structure and subsidence of Rockall Trough from two-ship seismic experiments. *Journal of Geophysical Research*, Vol. 95, No. B12, 19821-19837.

KESER NEISH, J. 1993. Seismic structure of the Hatton-Rockall area: an intergrated seismic/modelling study from composite datasets. 1047-1056 in *Petroleum Geology of Northwest Europe: Proceedings of the 4th Conference*. PARKER, J R (editor). (London: The Geological Society.)

KIMBELL, G S and STONE, P. 1995. Crustal magnetisation variations across the Iapetus Suture Zone. *Geological Magazine*, Vol. 132, 599-609.

KIMBELL, G S and QUIRK, D G. 1999. Crustal magnetic structure of the Irish Sea region: evidence for a major basement boundary beneath the Isle of Man. 227-238 in *In sight of the suture: the geology of the Isle of Man in its Iapetus Ocean context*. WOODCOCK, N H, QUIRK, D G, FITCHES, W R and BARNES, R P (editors). *Geological Society, London, Special Publications*, No. 160.

KIMBELL, G S, GATLIFF, R W, RITCHIE, J D, WALKER, A S D, and WILLIAMSON, J P. 2004. Regional three-dimensional modelling of the NE Atlantic margin. *Basin Research*, Vol. 16, 259-278.

KIMBELL, G S, RITCHIE, J D, JOHNSON, H, and GATLIFF, R W. 2005. Controls on the structure and evolution of the NE Atlantic margin revealed by regional potential field imaging and 3D modelling. 933-945 in *Petroleum Geology: North-West Europe and Global Perspectives - Proceedings of the 6th Petroleum Geology Conference*. DORÉ, A G and VINING, B (editors). (London: The Geological Society.)

LEE, M K. 1996. Techniques for basin identification on the northwest UK – Faroes continental margin from marine and satellite gravity data. *EAGE 58th Conference and Technical Exhibition – Amsterdam, The Netherlands, 3-7 June 1996*. Abstract M053.

LEFORT, J-P, and MAX, M D. 1984. Development of the Porcupine Seabight: use of magnetic data to show the direct relationship between early oceanic and continental structures. *Journal of the Geological Society, London*, Vol. 148, 149-164.

LOUDEN, K E, TUCHOLKE, B E, and OAKLEY, G N. 2004. Regional anomalies of sediment thickness, basement depth and isostatic crustal thickness in the North Atlantic Ocean. *Earth and Planetary Science Letters*, Vol. 224, 193-211.

MCCANN, T. 1996. The North Celtic Sea reflector – a possible basement structure, offshore southern Ireland. *Tectonophysics*, Vol. 266, 361-377.

MCCANN, T, and SHANNON, P M. 1994. Late Mesozoic reactivation of Variscan faults in the North Celtic Sea Basin, Ireland. *Marine and Petroleum Geology*, Vol. 11, 94-103.

MACKENZIE, G D, MOREWOOD, N C, SHANNON, P M and JACOB, A W B. 2002a. RAPIDS 3 wide angle profiling final report. Petroleum Infrastructure Project, Rockall Studies Group Report 97/11.

MACKENZIE, G D, SHANNON, P M, JACOB, A W B, MOREWOOD, N C, MAKRIS, J, GAYE, M and EGLOFF, F. 2002b. The velocity structure of the sediments in the southern Rockall Basin: results from new wide-angle seismic modelling. *Marine and Petroleum Geology*, Vol. 19, 983-1003.

MCKERROW, W S, and SOPER, N J. 1989. The Iapetus suture in the British Isles. *Geological Magazine*, Vol. 126, 1-8.

MAKRIS, J, EGLOFF, R, JACOB, A W B, MOHR, P, MURPHY, T, and RYAN, P. 1988. Continental crust under the southern Porcupine Seabight west of Ireland. *Earth and Planetary Science Letters*, Vol. 89, 387-397.

MASSON, D G, and MILES, P R. 1986. Structure and development of Porcupine Seabight sedimentary basin, offshore southwest Ireland. *Bulletin of the American Society of Petroleum Geologists*, Vol. 70, 536-548.

MASSON, D G, MONTADERT, L, and SCRUTTON R A. 1985. Regional geology of the Goban Spur continental margin. *Initial Reports of the Deep Sea Drilling Project*, Leg 80, 1115-1139.

MOREWOOD, N C, MACKENZIE, G D, SHANNON, P M, O'REILLY, B M, READMAN, P W, AND MAKRIS, J. 2005. The crustal structure and regional development of the Irish Atlantic margin region. 1023-1033 in *Petroleum Geology: North-West Europe and Global Perspectives - Proceedings of the 6th Petroleum Geology Conference*. Doré, A G and Vining, B (editors). (London: The Geological Society.)

MÜLLER, R D, ROEST W R, ROYER, J-Y, GAHAGAN, L M and SCLATER, J G. 1997. Digital isochrons of the world's ocean floor. *Journal of Geophysical Research*, Vol. 102, 3211-3214.

MURDOCH, L M, MUSGROVE, F W and PERRY, J S. 1995. Tertiary uplift and inversion history in the North Celtic Sea Basin and its influence on source rock maturity. 297-319 in *Basin Inversion*. BUCHANAN, J G, and BUCHANAN, P G (editors). *Special Publication of the Geological Society, London*, No. 88.

NAYLOR, D, SHANNON, P, and MURPHY, N. 1999. Irish Rockall Basin region - a standard structural nomenclature system. Petroleum Affairs Division, Special Publication 1/99.

NAYLOR, D, SHANNON, P, and MURPHY, N. 2002. Porcupine-Goban region - a standard structural nomenclature system. Petroleum Affairs Division, Special Publication 1/02.

NORTON, M G. 2002. Tectonic evolution of the Porcupine Basin. Petroleum Infrastructure Project, Porcupine Studies Group Report P00/8.

OLDENBURG, D W. 1974. The inversion and interpretation of gravity anomalies. *Geophysics*, Vol. 39, 526-536.

- O'REILLY, B M, SHANNON, P M, and VOGT, U. 1991. Seismic studies in the North Celtic Sea Basin: implications for basin development. *Journal of the Geological Society, London*, Vol. 148, 191-195.
- O'REILLY, B M, HAUSER, F, JACOB, A W B, SHANNON, P M, MAKRIS, J and VOGT, U. 1995. The transition between the Erris and the Rockall Basins: new evidence from wide-angle seismic data. *Tectonophysics*, Vol. 241, 143-163.
- O'REILLY, B M, HAUSER, F, JACOB, A W B, and SHANNON, P M. 1996. The lithosphere below the Rockall Trough: wide-angle seismic evidence for extensive serpentinisation. *Tectonophysics*, Vol. 255, 1-23.
- O'REILLY, B M, READMAN, P W, and HAUSER, F. 1998. Lithospheric structure across the western Eurasian plate from a wide-angle seismic and gravity study: evidence for a regional thermal anomaly. *Earth and Planetary Science Letters*, Vol. 156, 275-280.
- PARKER, R L. 1972. The rapid calculation of potential anomalies. *Geophysical Journal of the Royal Astronomical Society*, Vol. 31, 447-455.
- PÉREZ-GUSSINYÉ, M, RESTON, T J, and PHIPPS MORGAN, J. 2001. Serpentinization and magmatism during extension at non-volcanic margins: the effect of initial lithospheric structure. 551-576 in *Non-volcanic rifting of continental margins: a comparison of evidence from land and sea*. WILSON, R C L, WHITMARSH, R B, TAYLOR, B, and FROITZHEIM, N (editors). *Geological Society, London, Special Publications*, No. 187.
- PESGB (PETROLEUM EXPLORATION SOCIETY OF GREAT BRITAIN), 2005. *Structural Framework of the North Sea and Atlantic Margin (2005 Edition)*. (London: Petroleum Exploration Society of Great Britain.)
- PHARAOH, T C. 1999. Palaeozoic terranes and their lithospheric boundaries within the Trans-European Suture Zones (TESZ): a review. *Tectonophysics*, Vol. 314, 17-41.
- PHILLIPS, W E A, STILLMAN, C J, and MURPHY, T. 1976. A Caledonian plate tectonic model. *Journal of the Geological Society, London*. Vol. 132, 579-609.
- PLANKE, S. 1994. Geophysical response of flood basalts from analysis of wire line logs: Ocean Drilling Program Site 642, Voring volcanic margin. *Geophysics*, Vol. 99, 9279-9296.
- PLANKE, S, and CAMBRAY, H. 1998. Seismic properties of flood basalts from Hole 917A downhole data, southeast Greenland. *Proceedings of the Ocean Drilling Program, Scientific Results*, Vol. 152, 453-462.
- READMAN, P W, O'REILLY, B M, SHANNON, P M, and NAYLOR, D. 2005. The deep structure of the Porcupine Basin, offshore Ireland, from gravity and magnetic studies. 1047-1056 in *Petroleum Geology: North-West Europe and Global Perspectives - Proceedings of the 6th Petroleum Geology Conference*. DORÉ, A G and VINING, B (editors). (London: The Geological Society.)
- RESTON, T J, GAW, V, PENNELL, J, KLAESCHEN, D, STUBENRAUCH, A, and WALKER, I. 2004. Extreme crustal thinning in the south Porcupine Basin and the nature of the Porcupine Median High: implications for the formation of non-volcanic rifted margins. *Journal of the Geological Society, London*, Vol. 161, 783-798.
- ROBERTS, D G. 1975. Marine geology of the Rockall Plateau and Trough. *Philosophical Transactions of the Royal Society of London, Series A*, Vol. 278, 447-509.
- ROBERTS, D G, MONTADERT, L, and SEARLE, R C. 1979. The western Rockall plateau: stratigraphy and structural evolution. *Initial Reports of the Deep Sea Drilling Programme*, Vol. 48, 1061-1088.
- ROBERTS, D G, BACKMAN, J, MORTON, A C, MURRAY, J W and KEANE, J. B. 1984. Evolution of volcanic rifted margins: synthesis of Leg 81 results on the west margin of Rockall Plateau. *Initial Reports of the Deep Sea Drilling Programme*, Vol. 81, 883-911.
- ROBERTS, D G, GINZBERG, A, NUNN, K, and MCQUILLIN, R. 1988. The structure of the Rockall Trough from seismic refraction and wide-angle reflection measurements. *Nature*, Vol. 332, 632-635.
- SANDWELL, D T, and SMITH, W H F. 1997. Marine gravity anomaly from Geosat and ERS 1 satellite altimetry. *Journal of Geophysical Research*, Vol. 102, 10039-10054.
- SCHLUMBERGER, 1991. *Log Interpretation Principles/Applications*. (Houston, Texas: Schlumberger Educational Services).
- SCLATER, J G, and CHRISTIE, P A F. 1980. Continental stretching: an explanation of the post-mid-Cretaceous subsidence of the central North Sea basin. *Journal of Geophysical Research*, Vol. 85, 3711-3739.
- SCRUTTON, R A. 1970. Results of a seismic refraction experiment on Rockall Bank. *Nature*, Vol. 227, 826-827.
- SCRUTTON, R A. 1972. The crustal structure of the Rockall Plateau microcontinent. *Geophysical Journal of the Royal Astronomical Society*, Vol. 27, 259-275.
- SCRUTTON, R A, and BENTLEY, P A D. 1988. Major Cretaceous volcanic province in the southern Rockall Trough. *Earth and Planetary Science Letters*, Vol. 91, 198-204
- SHANNON, P M., JACOB, A W B, O'REILLY, B M, HAUSER, F, READMAN, P W, and MAKRIS, J. 1999. Structural setting, geological development and basin modelling in the Rockall Trough. 421-431 in *Petroleum Geology of Northwest Europe: Proceedings of the 5th Conference*. FLEET, A J, and BOLDY, S A R (editors). (London: The Geological Society.)
- SHIPBOARD SCIENTIFIC PARTY, 1979. Sites 405 and 406. *Initial Reports of the Deep Sea Drilling Programme*, Vol. 48, 1061-1088.

- SMITH, C. 1995. Evolution of the Cockburn Basin: implications for the structural development of the Celtic Sea basins. 279-295 in *The Petroleum Geology of Ireland's Offshore Basins*. CROKER, P F, and SHANNON, P M (editors). *Special Publication of the Geological Society, London*, No. 93.
- SMITH, L K, WHITE, R S, KUSZNIR, N J, and the iSIMM TEAM. 2005. Structure of the Hatton Basin and adjacent continental margin. 947-956 in *Petroleum Geology: North-West Europe and Global Perspectives - Proceedings of the 6th Petroleum Geology Conference*. DORÉ, A G and VINING, B (editors). (London: The Geological Society.)
- SRIVASTAVA, S P, VOPPEL, D, and TUCHOLKE, B. 1988. *Geophysical Atlas of the North Atlantic 50° to 72°N and 0° to 65° W*. (Hamburg: Deutsches Hydrographisches Institut.)
- TATE, M P. 1992. The Clare Lineament: a relic transform fault west of Ireland. 375-384 in *Basins on the Atlantic Seaboard: Petroleum Geology, Sedimentology and Basin Evolution*. PARNELL, J (Editor). *Geological Society, London, Special Publications*, No.62.
- TATE, M P. 1993. Structural framework and tectonostratigraphic evolution of the Porcupine Seabight Basin, offshore western Ireland. *Marine and Petroleum Geology*, Vol. 10, 95-123.
- TATE, M P, and DOBSON, M R. 1988. Syn- and post-rift igneous activity in the Porcupine Seabight Basin and adjacent continental margin W of Ireland. 309-334 in *Early Tertiary Volcanism and the Opening of the NE Atlantic*. MORTON, A C and PARSON, L M (editors). *Geological Society, London, Special Publications*, No. 39.
- THINON, I, MATIAS, L, RÉHAULT, J P, HIRN, A, FIDALGO-GONZÁLEZ, L, and AVEDIK, F. 2003. Deep structure of the Armorican Basin (Bay of Biscay): a review of Norgasis seismic reflection and refraction data. *Journal of the Geological Society, London*, Vol. 160, 99-116.
- TUCKER, R M and ARTER, G. 1987. The tectonic evolution of the North Celtic Sea and Cardigan Bay basins with special reference to basin inversion. *Tectonophysics*, Vol. 137, 291-307.
- VERHOEF, J, ROEST, W R, MACNAB, R, ARKANI-HAMED, J, ET AL. 1996. Magnetic anomalies of the Arctic and North Atlantic Oceans and adjacent land areas. *Geological Survey of Canada Open File Report*, No. 3125a.
- VOGT, U, MAKRIS, J, O'REILLY, B M, HAUSER, F, READMAN, P W, JACOB, A W B, and SHANNON, P M. 1998. The Hatton Basin and continental margin: crustal structure from wide-angle seismic and gravity data. *Journal of Geophysical Research*, Vol. 103, 12545-12566.
- WEISSEL, J K, AND KARNER, G D. 1989. Flexural uplift of rift flanks due to mechanical unloading of the lithosphere during extension. *Journal of Geophysical Research*, Vol. 94, 13919-13950.
- WESSEL, P, and SMITH, W H F. 1991. Free software helps map and display data. *EOS Transactions of the American Geophysical Union*, Vol. 72, 441, 445-446.
- WHITE, R S. 1992. Crustal structure and magmatism of North Atlantic continental margins. *Journal of the geological Society, London*, Vol. 149, 841-854.
- WHITE, R S, and MCKENZIE, D. 1989. Magmatism at rift zones: The generation of volcanic continental margins and flood basalts. *Journal of Geophysical Research*, Vol. 94, 7685-7729.
- WHITMARSH, R B, LANGFORD, J J, BUCKLEY, J S, BAILEY, R J, and BLUNDELL, D J. 1974. The crustal structure beneath Porcupine Ridge as determined by explosion seismology. *Earth and Planetary Science Letters*, Vol. 22, 197-204.
- WYLLIE, M R J, GREGORY, A R and GARDNER, G H F. 1956. Elastic wave velocities in heterogeneous and porous media. *Geophysics*, Vol. 21, 41-70.
- WYLLIE, M R J, GREGORY, A R and GARDNER, G H F. 1958. An experimental investigation of factors affecting elastic wave velocities in porous media. *Geophysics*, Vol. 23, 459-493.

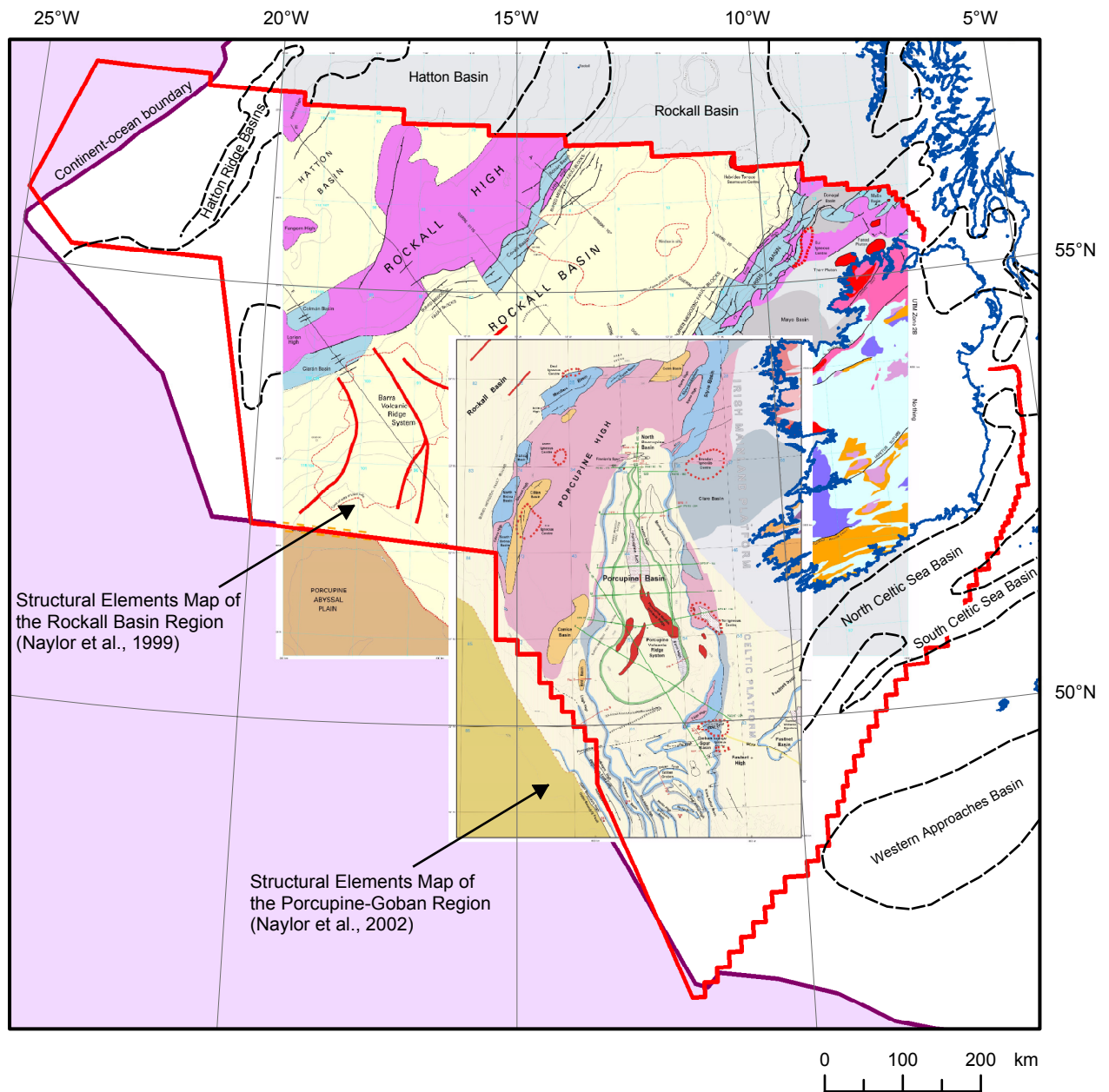


Figure 1 The Irish Passive Margin Modelling Project (IPmmP) study area, showing the locations of the structural element maps of Naylor et al. (1999, 2002), and the approximate extensions of the main basins outside the areas covered by these maps (black dashed lines). Red line indicates the Irish Designated Area.

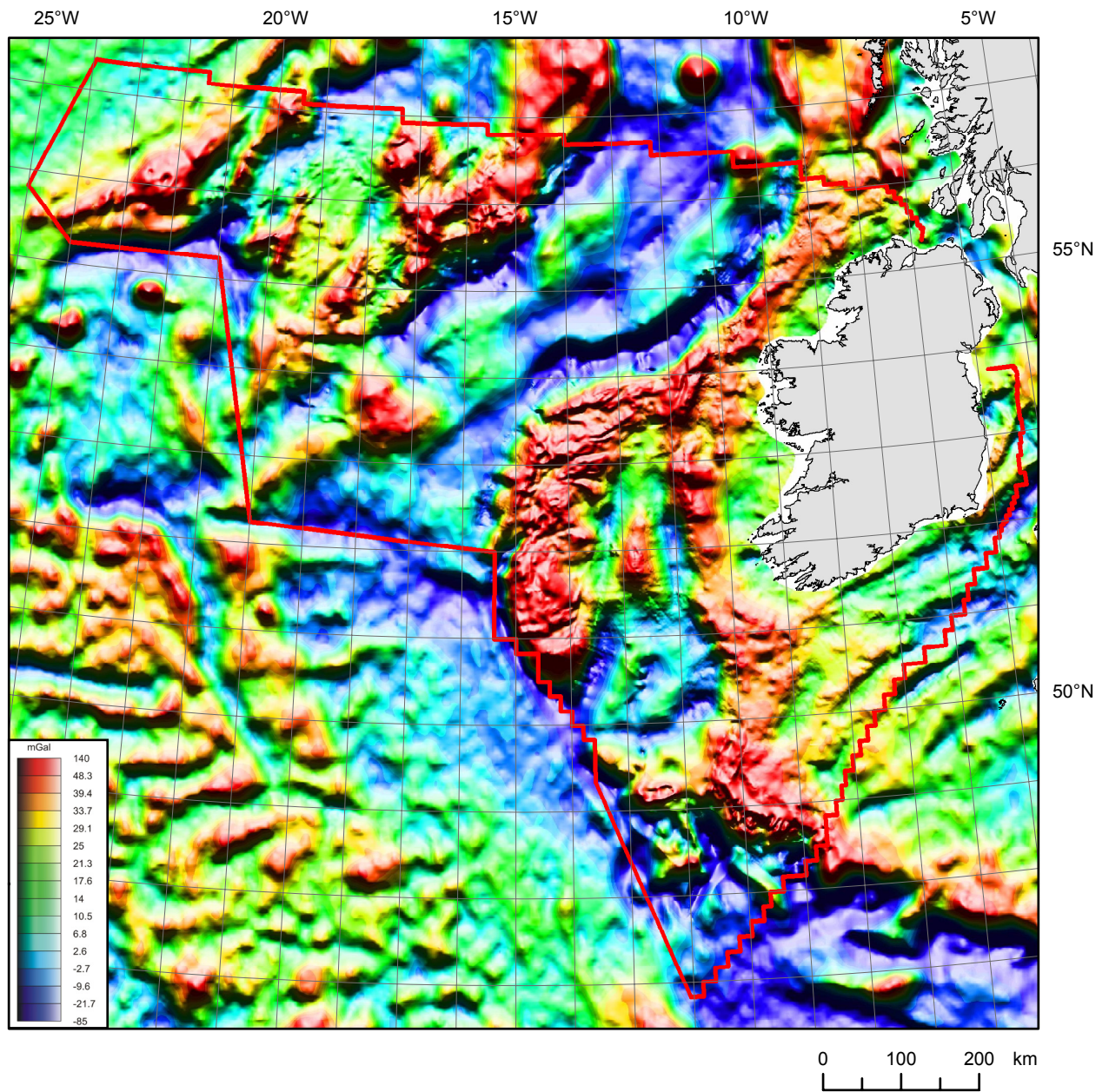


Figure 2 Colour shaded-relief image of the free-air gravity anomaly. Equal colour area; illumination from the north.

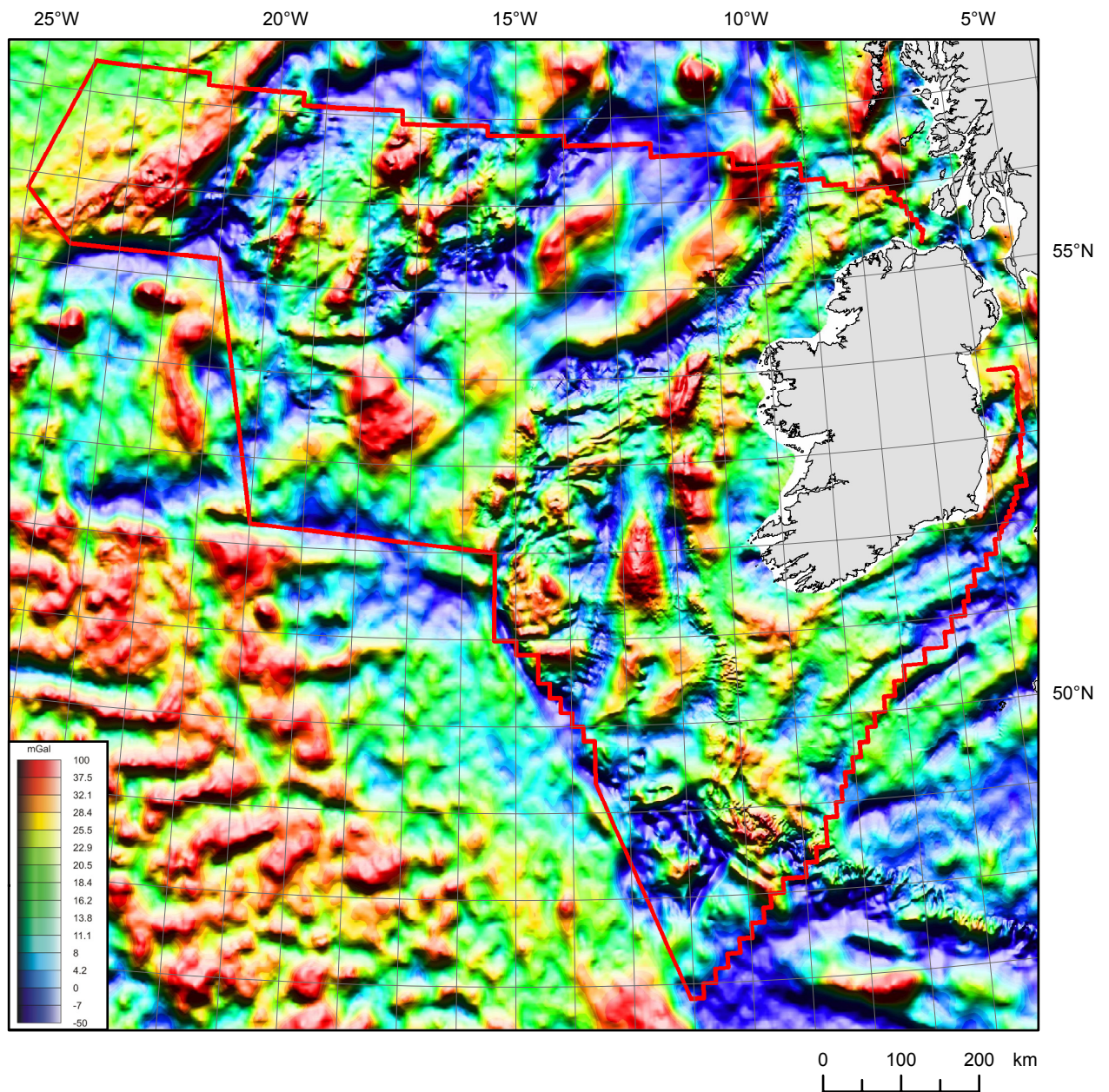


Figure 3 Colour shaded-relief image of the isostatically-corrected Bouguer gravity anomaly. Equal colour area; illumination from the north.

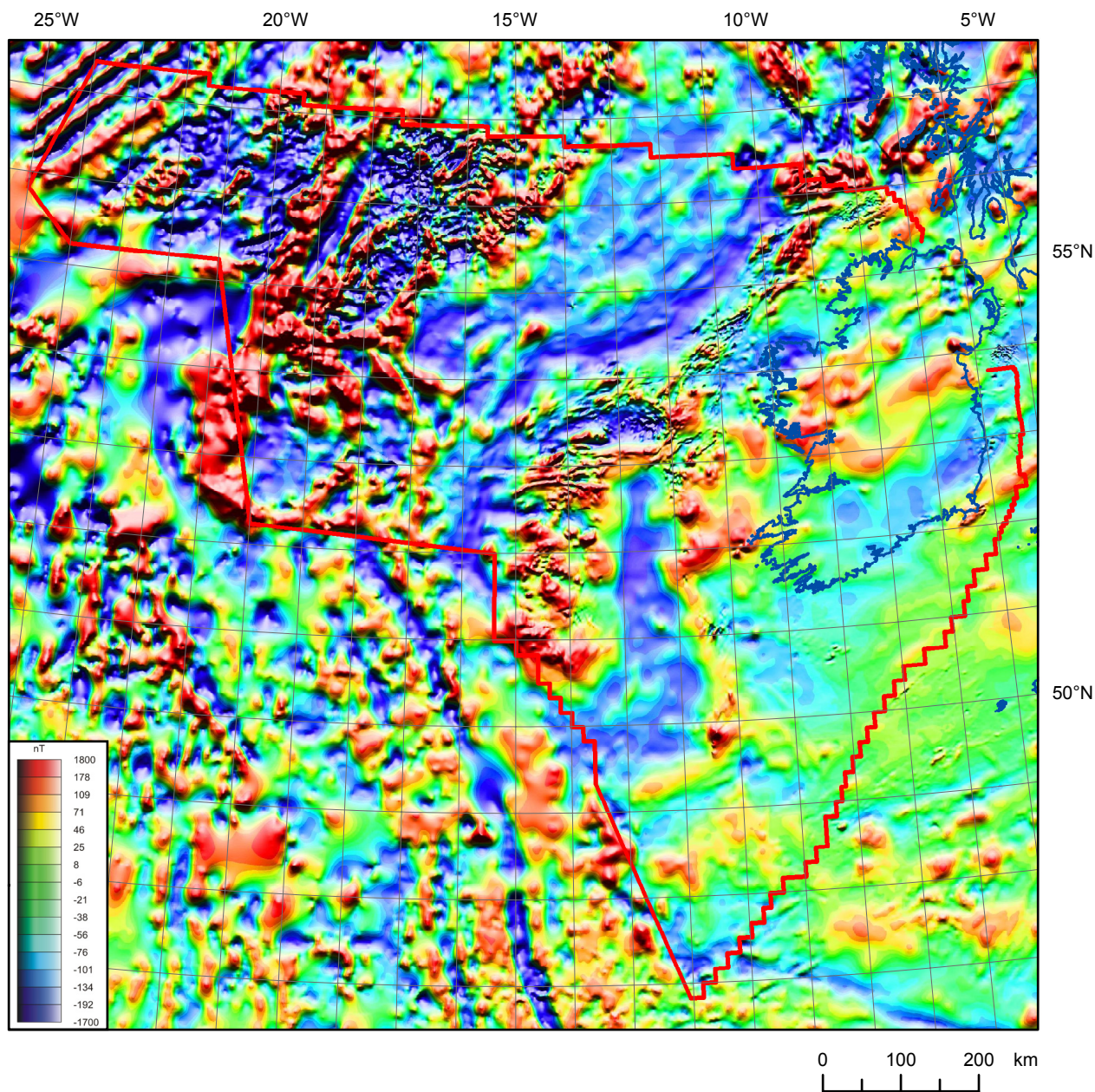


Figure 4 Colour shaded-relief image of the total magnetic field. Equal colour area; illumination from the north.

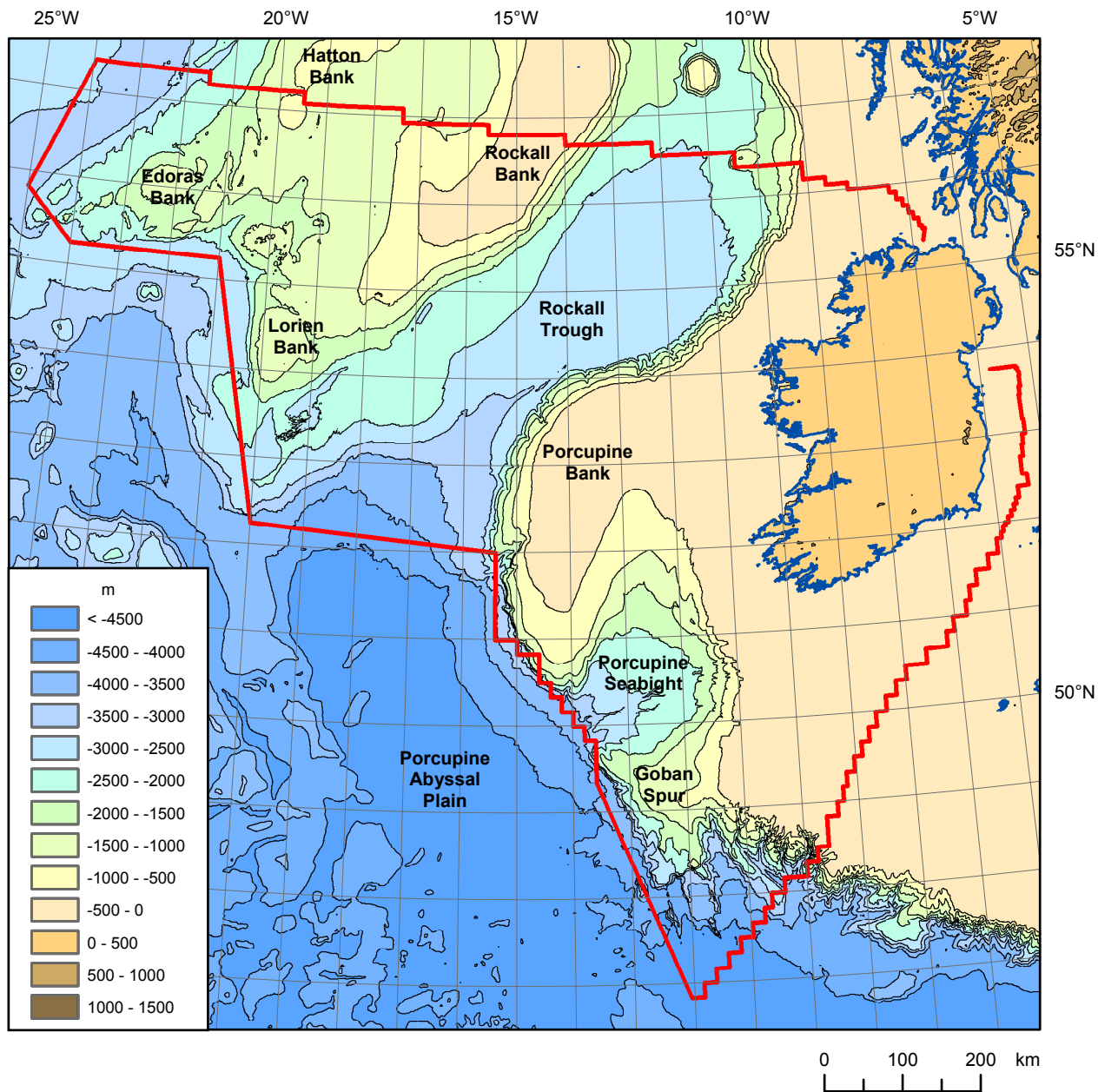


Figure 5 Topographic map of the IPmmP study area.

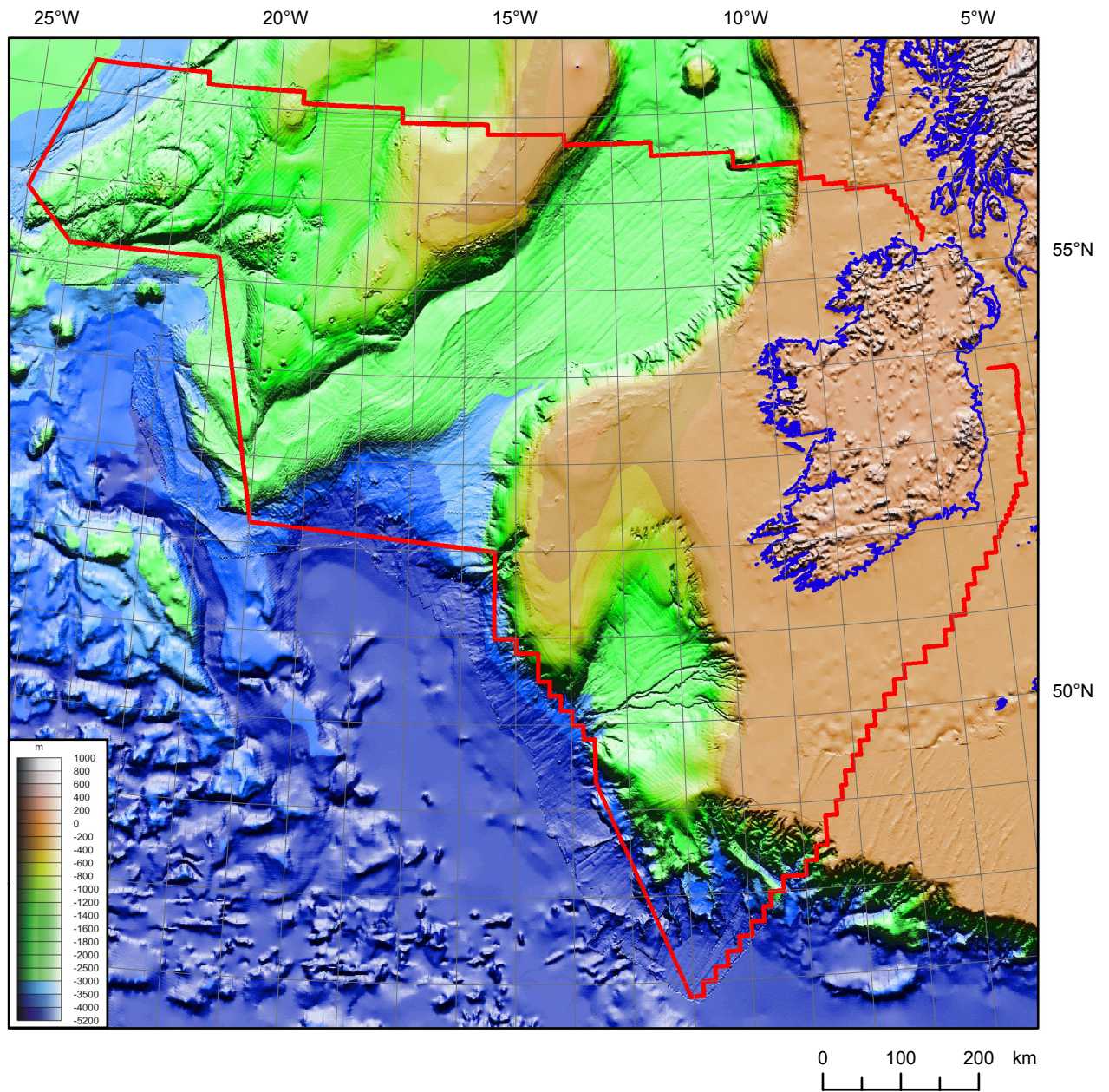


Figure 6 Colour shaded-relief topographic image. Illumination is from the north.

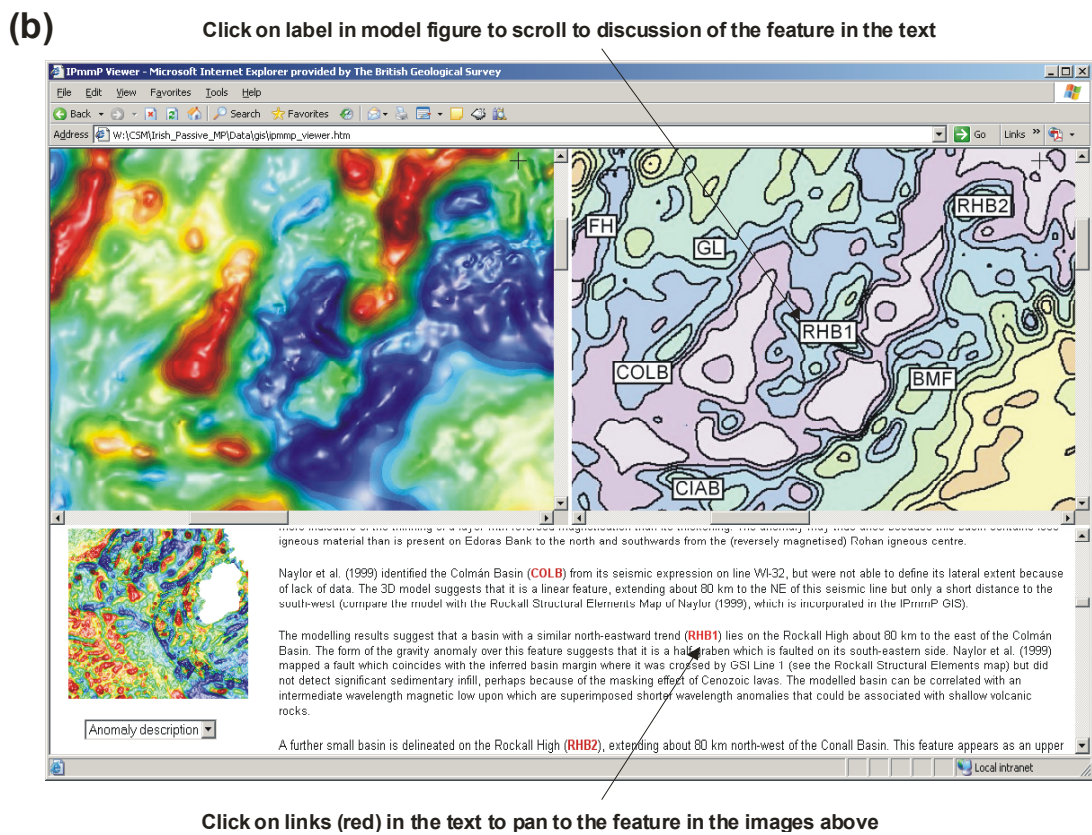
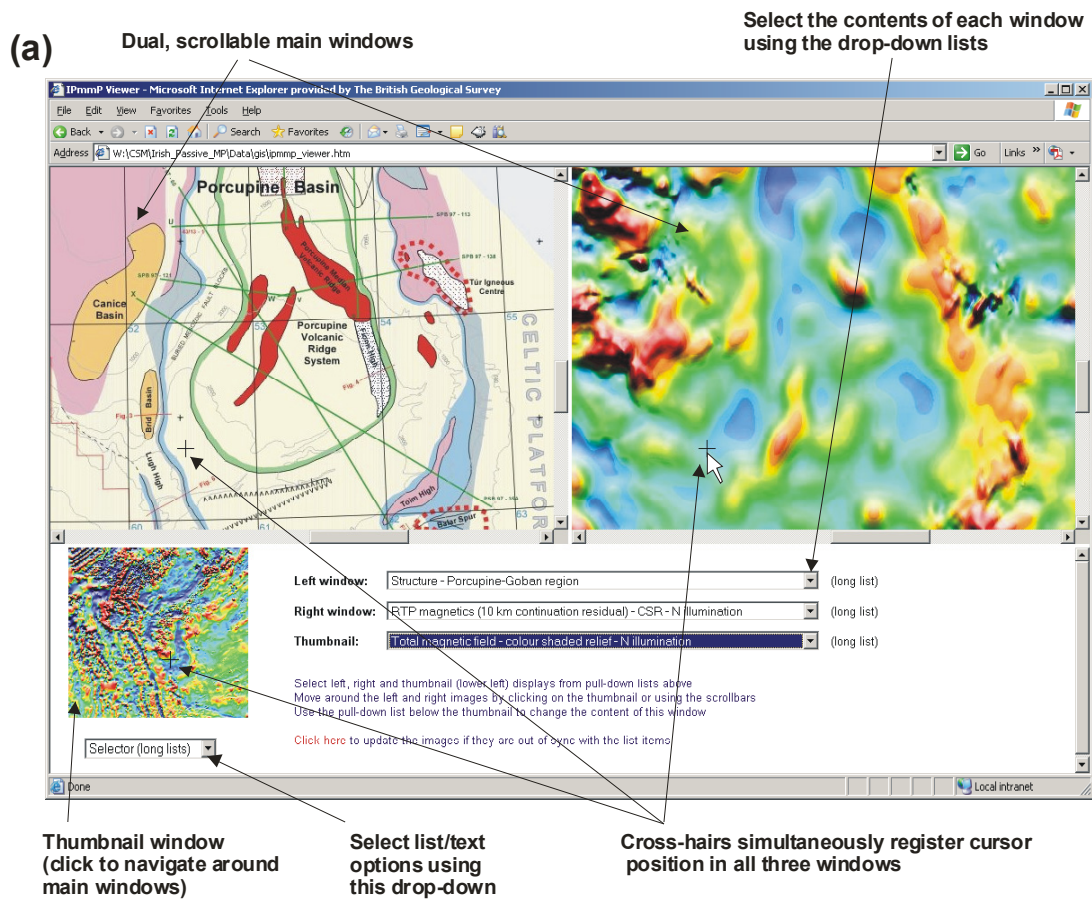


Figure 7 The IPmmP Viewer in (a) list mode, and (b) text mode.

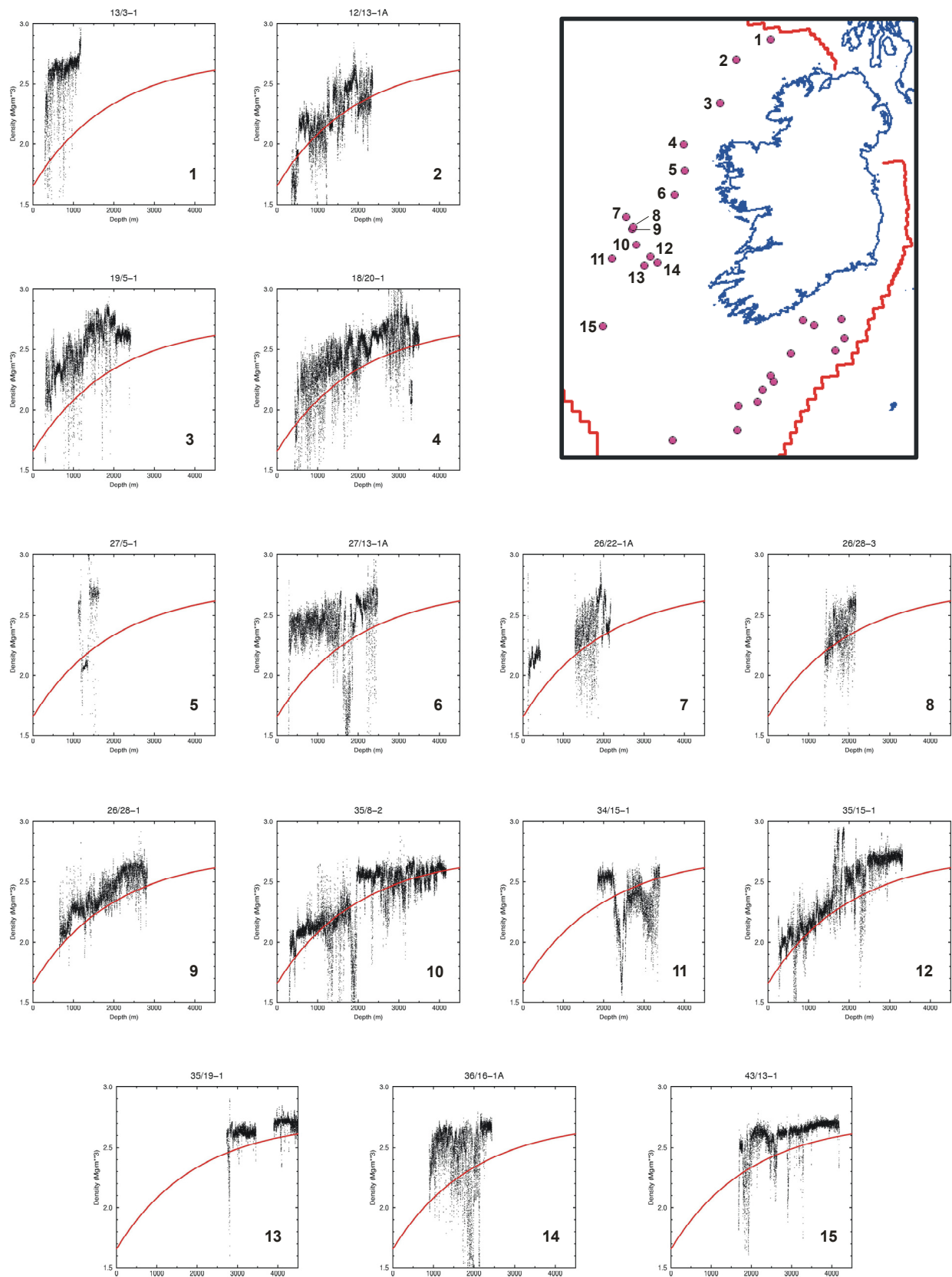


Figure 8 Density logs from wells west of Ireland. The red curve is the normal compaction curve for shale of Sclater and Christie (1980). Depths are relative to sea bed.

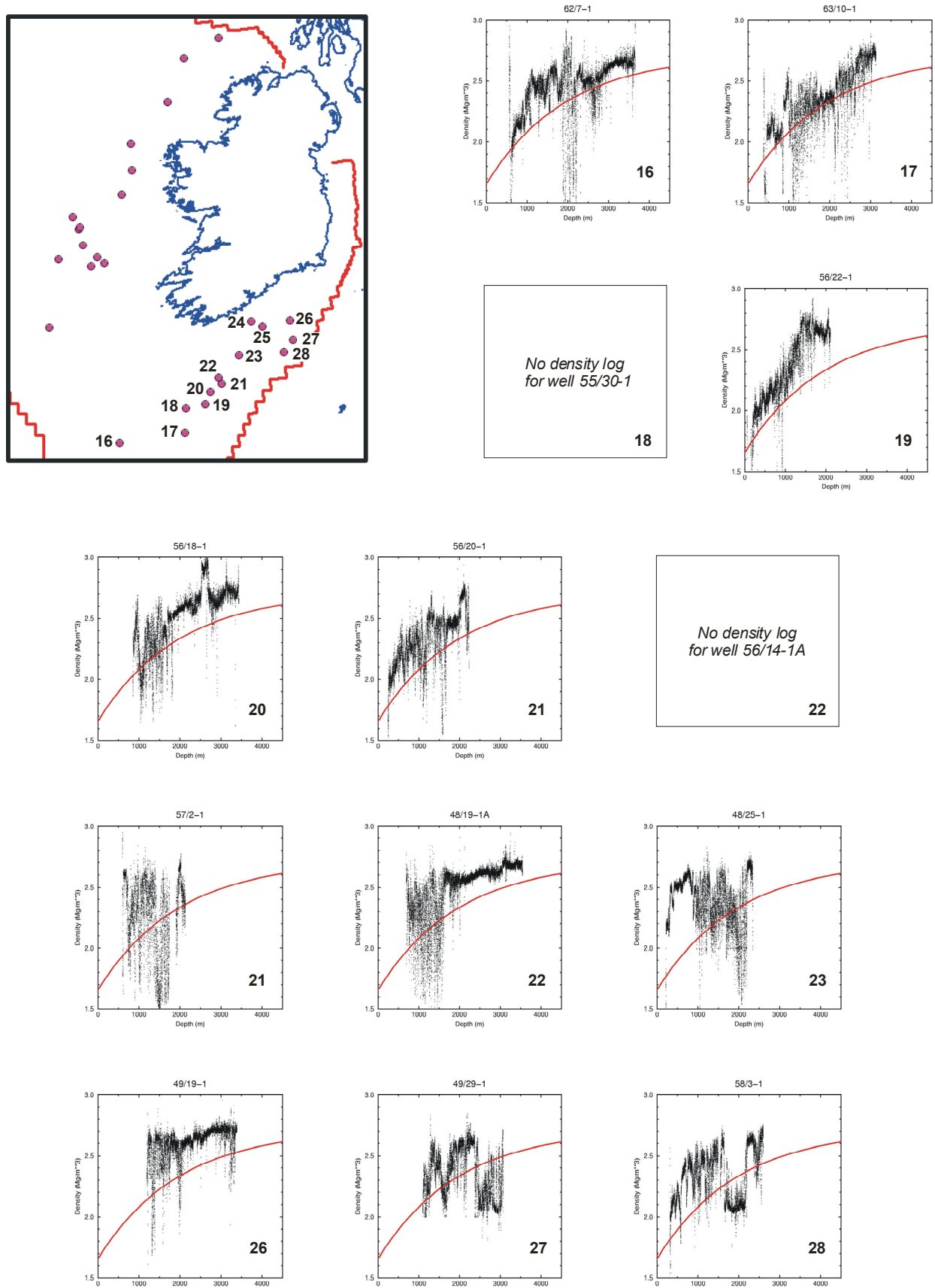


Figure 9 Density logs from wells south of Ireland. The red curve is the normal compaction curve for shale of Sclater and Christie (1980). Depths are relative to sea bed.

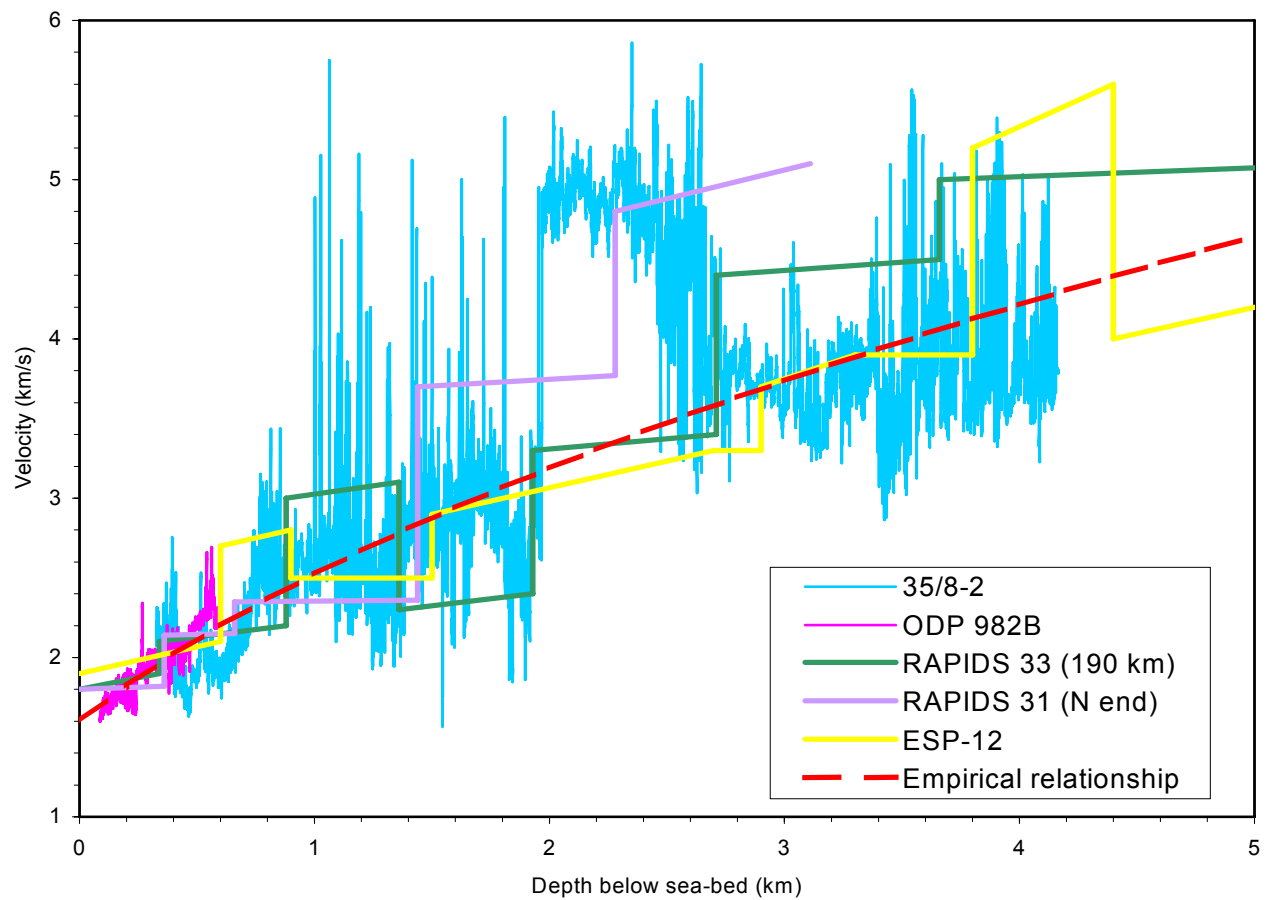


Figure 10 Comparison of an empirical velocity depth curve with wireline density logs and velocity models from wide-angle experiments in the Rockall Basin.

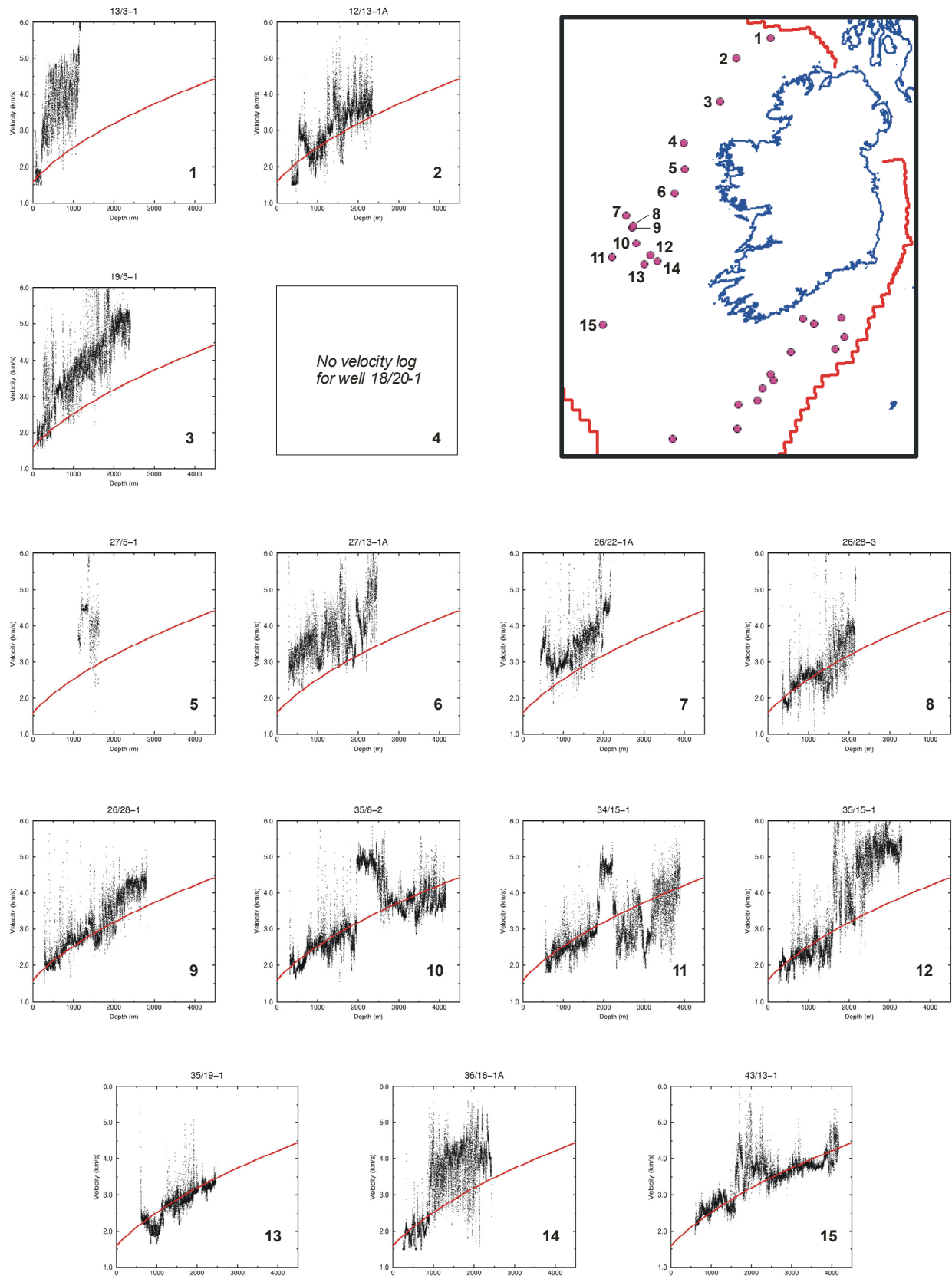


Figure 11 Velocity logs from wells west of Ireland. The red curve is the empirical (normal compaction) curve shown in Figure 10 and discussed in the text. Depths are relative to sea bed.

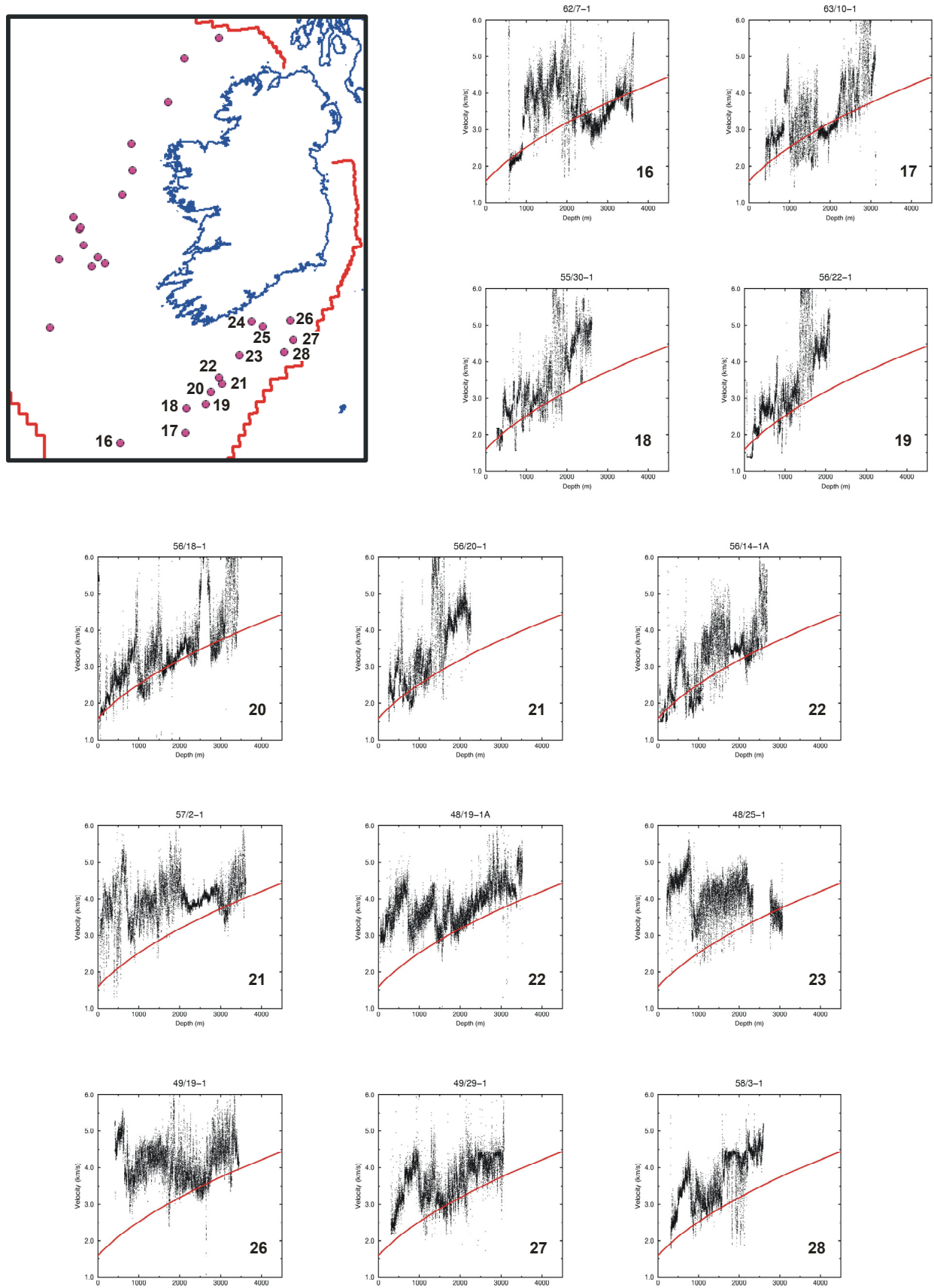


Figure 12 Velocity logs from wells south of Ireland. The red curve is the empirical (normal compaction) curve shown in Figure 8 and discussed in the text. Depths are relative to sea bed.

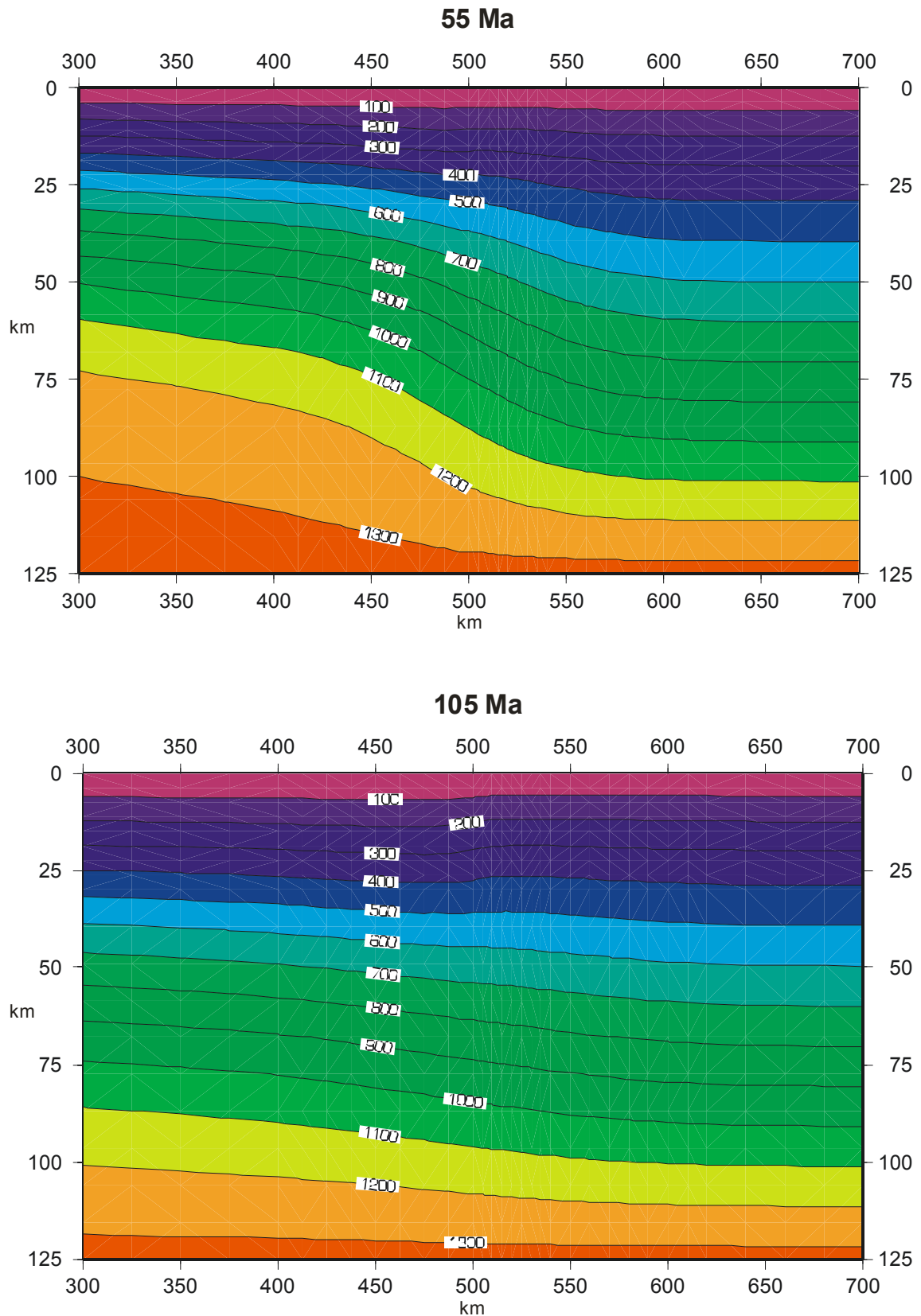


Figure 13 Simple model of thermal contrasts across a continent-ocean boundary 55 Ma and 105 Ma after ocean opening. Temperature contours at 100°C intervals. The continent-ocean boundary is at 500 km and the oceanic lithosphere lies to the left of this.

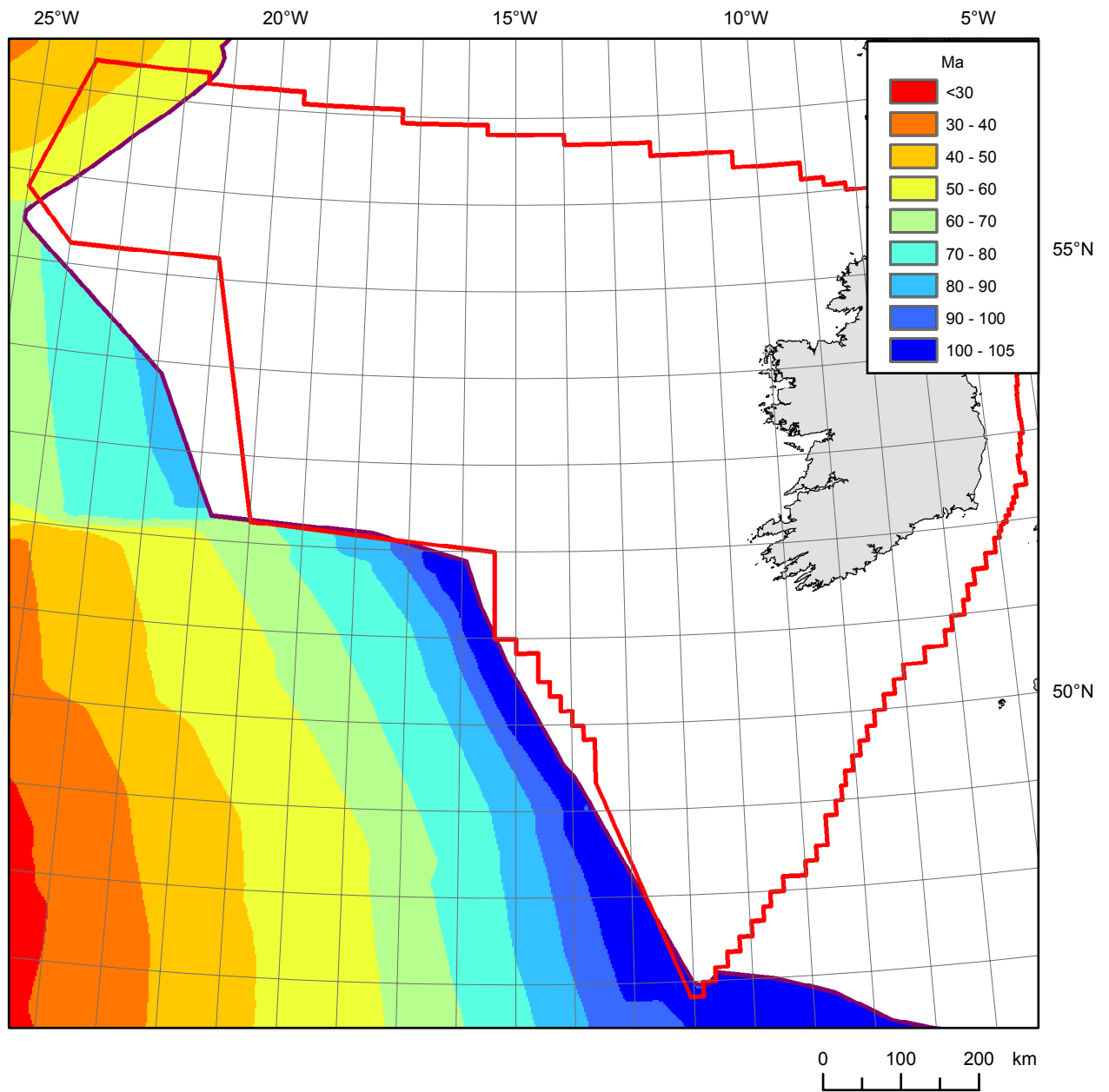


Figure 14 Age of ocean crust assumed in the thermal modelling (after Müller et al. 1997). Thick purple line is the interpreted continent-ocean boundary.

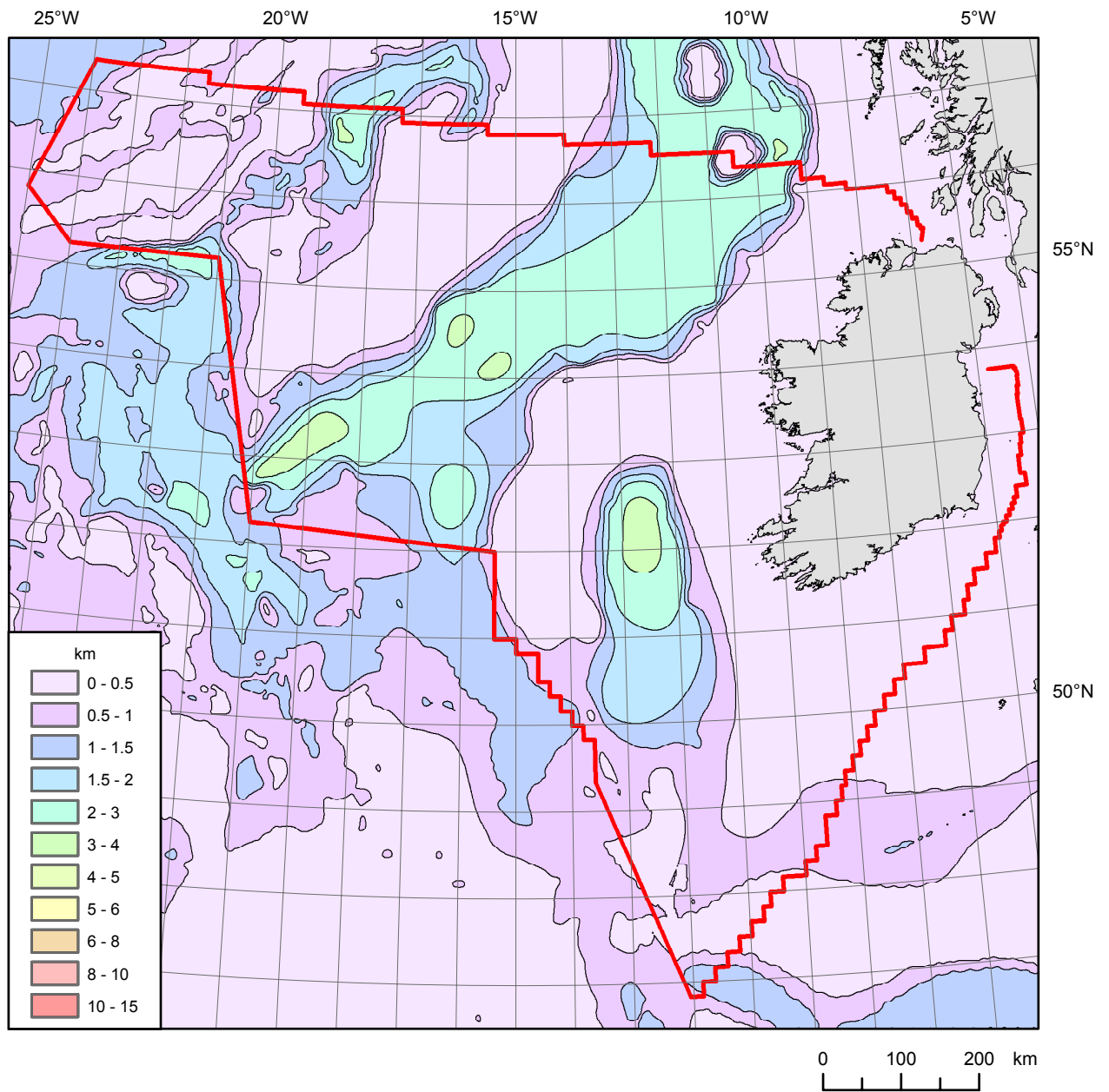


Figure 15 Thickness of Cenozoic (post-lava) sedimentary rocks assumed in the initial model.

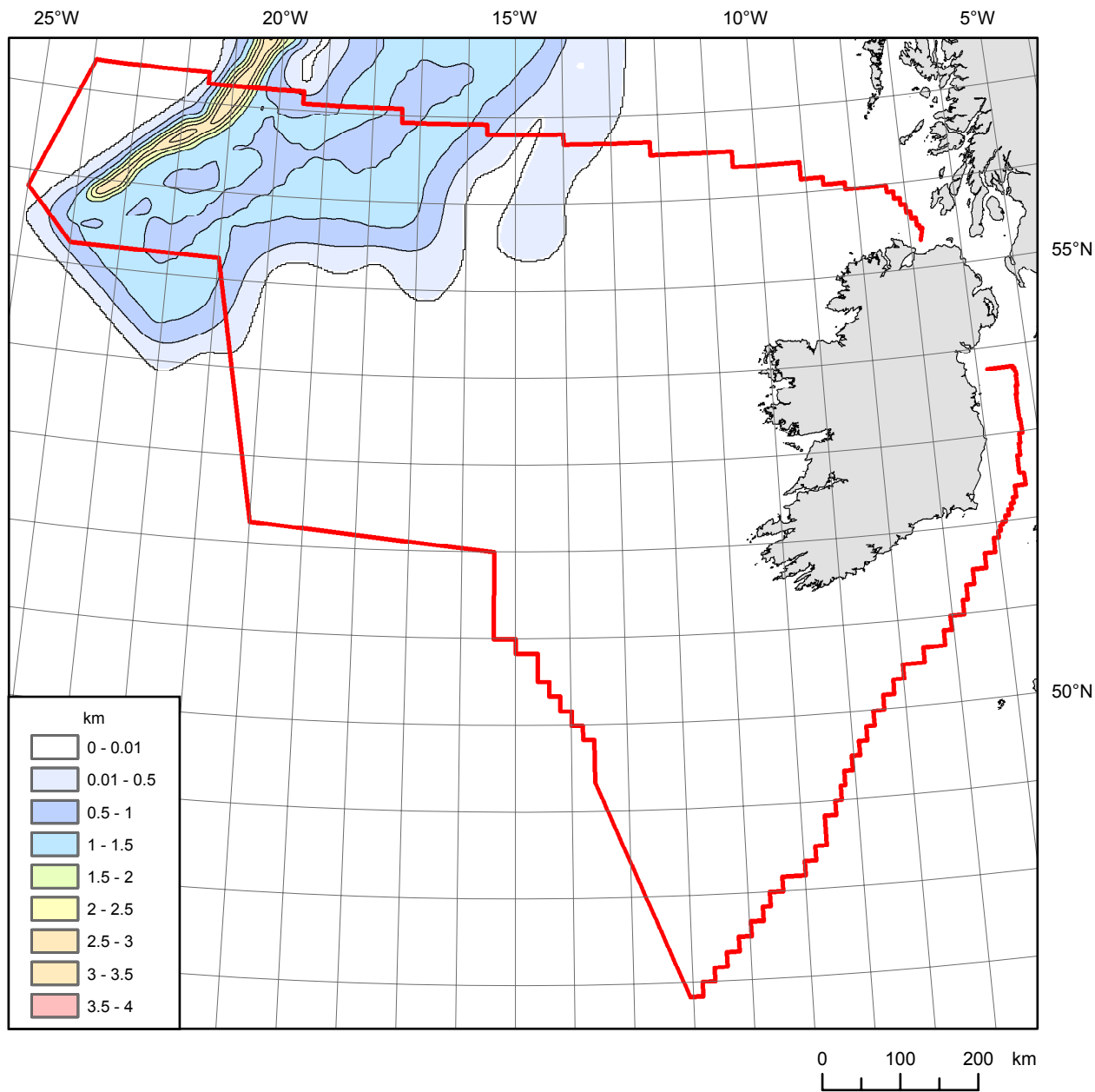


Figure 16 Thickness of lava in the Hatton-Rockall area assumed in the initial model.

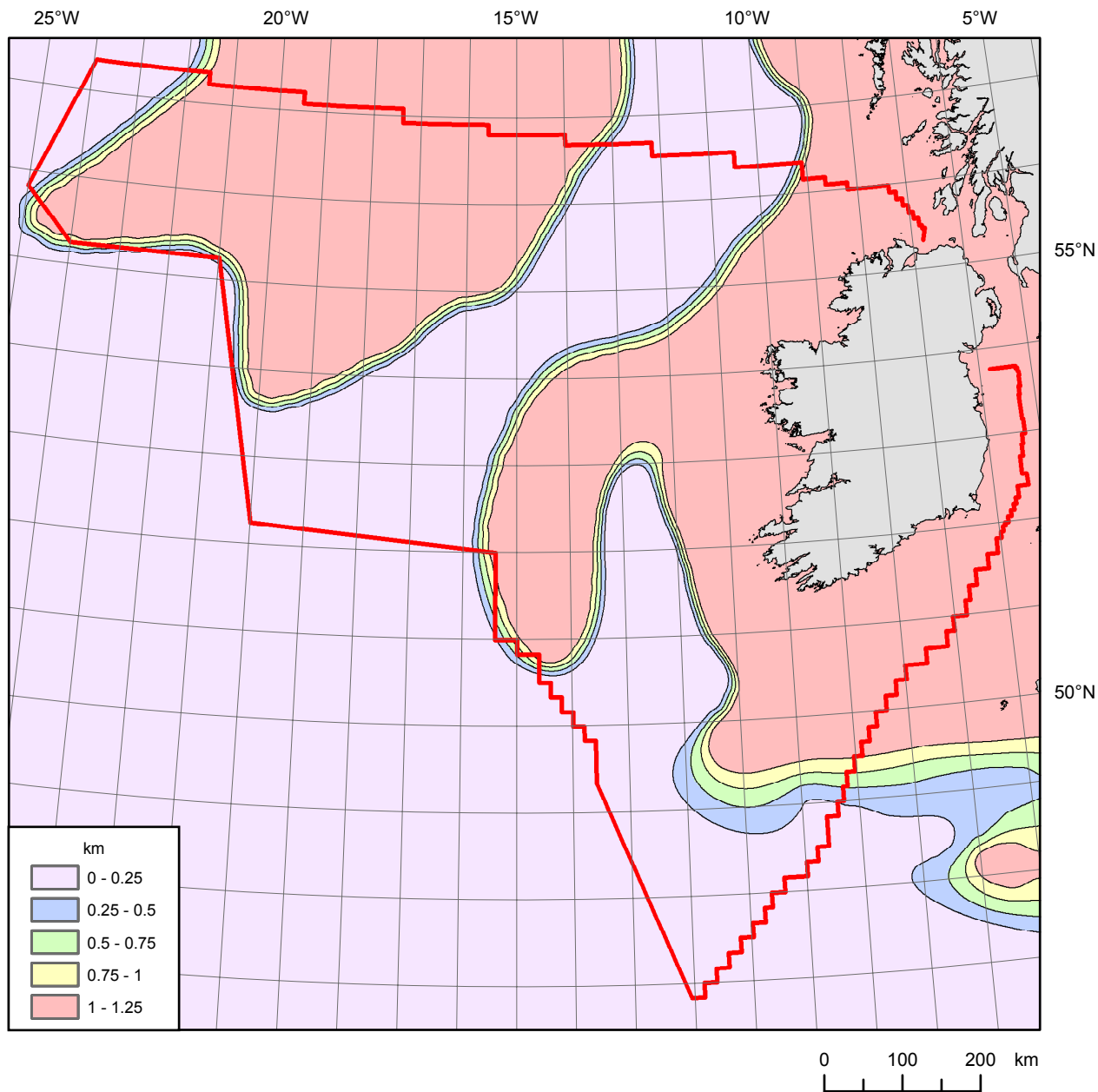


Figure 17 Variation in the denudation of pre-Cenozoic sedimentary rocks assumed when calculating the effect of overcompaction on the density of these rocks.

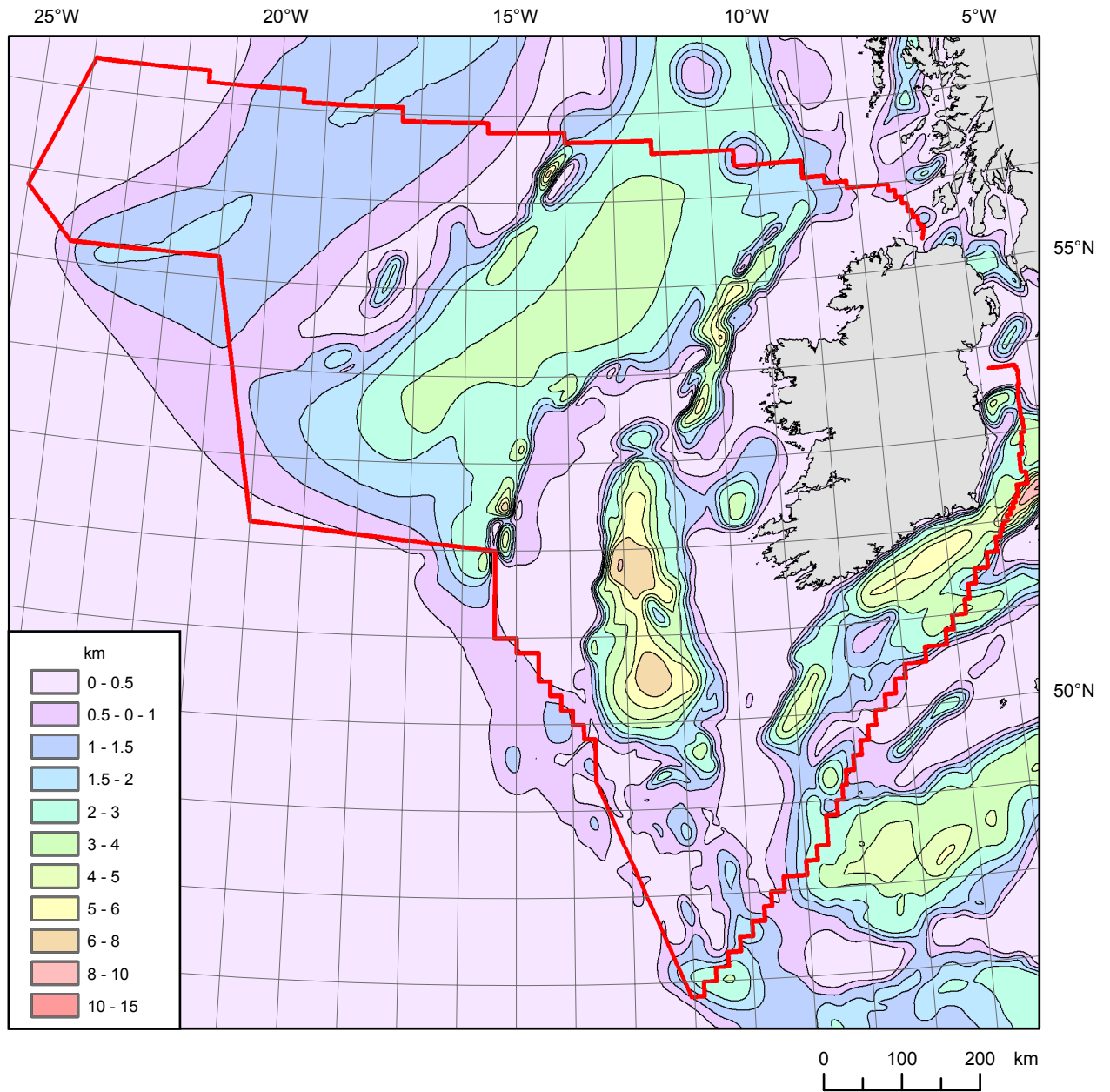


Figure 18 Thickness of pre-Cenozoic sedimentary rocks assumed in the initial model.

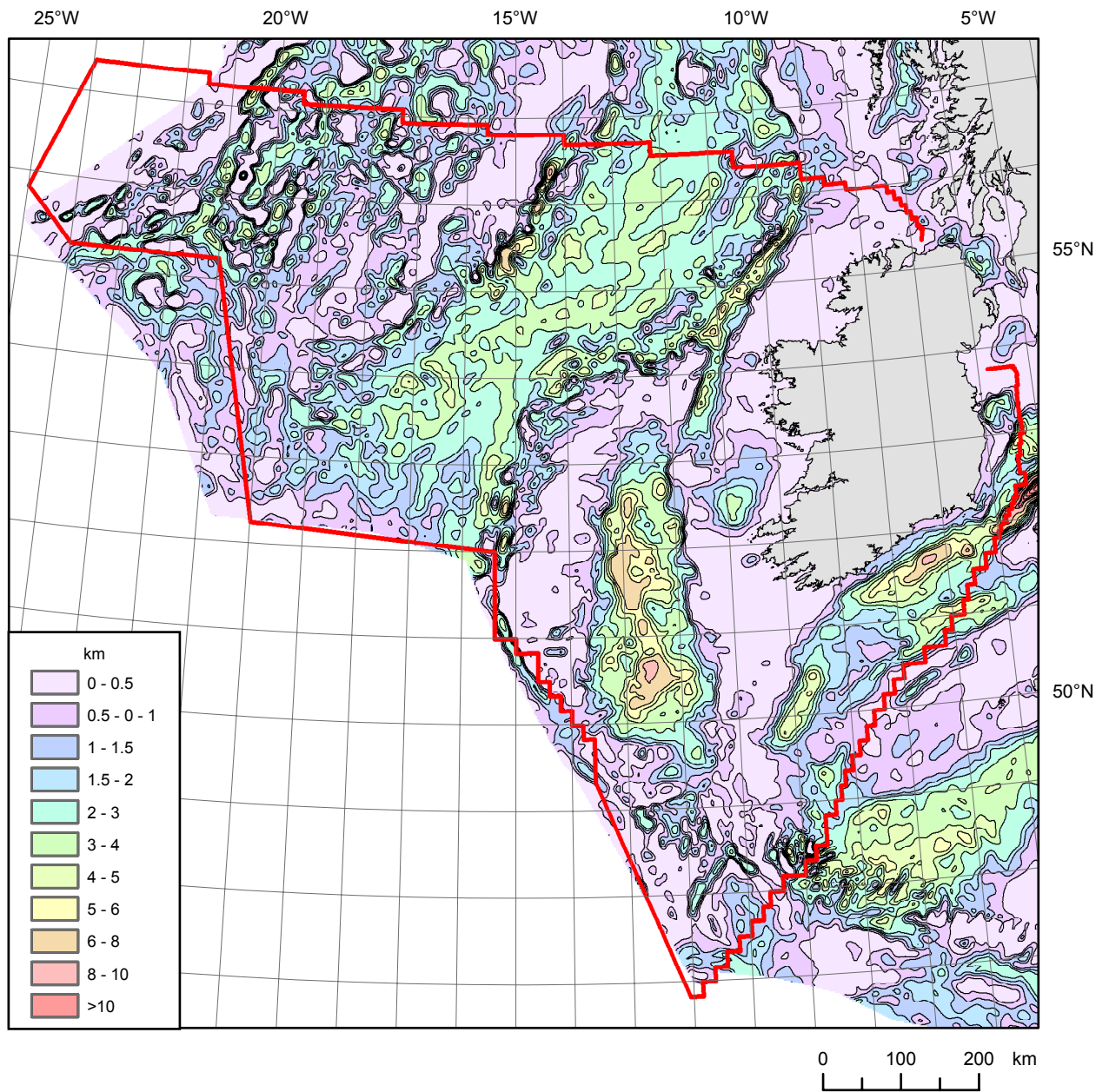


Figure 19 Thickness of pre-Cenozoic sedimentary rocks after model optimisation (continental areas).

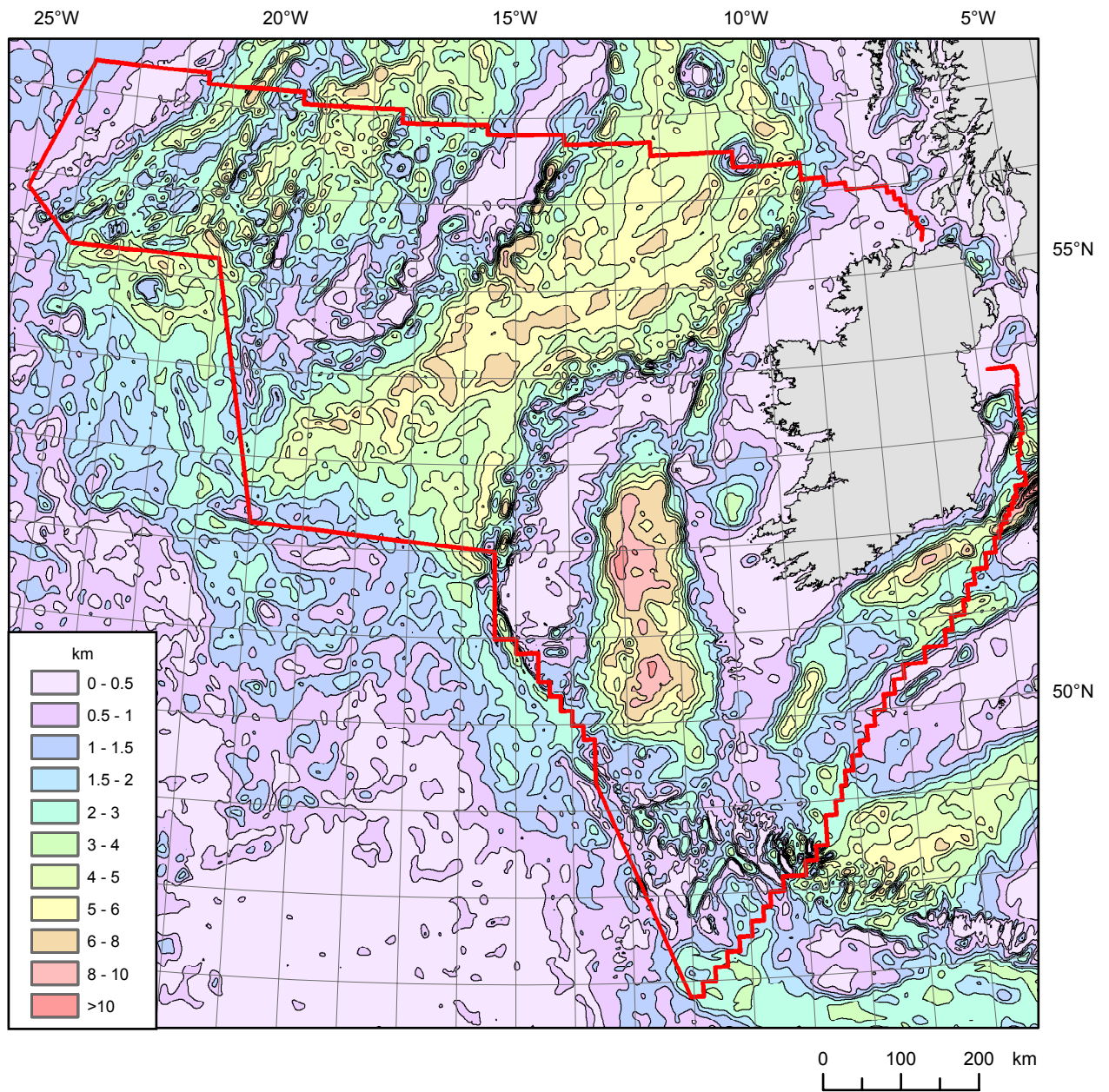


Figure 20 Total cover sequence thickness in the optimised model.

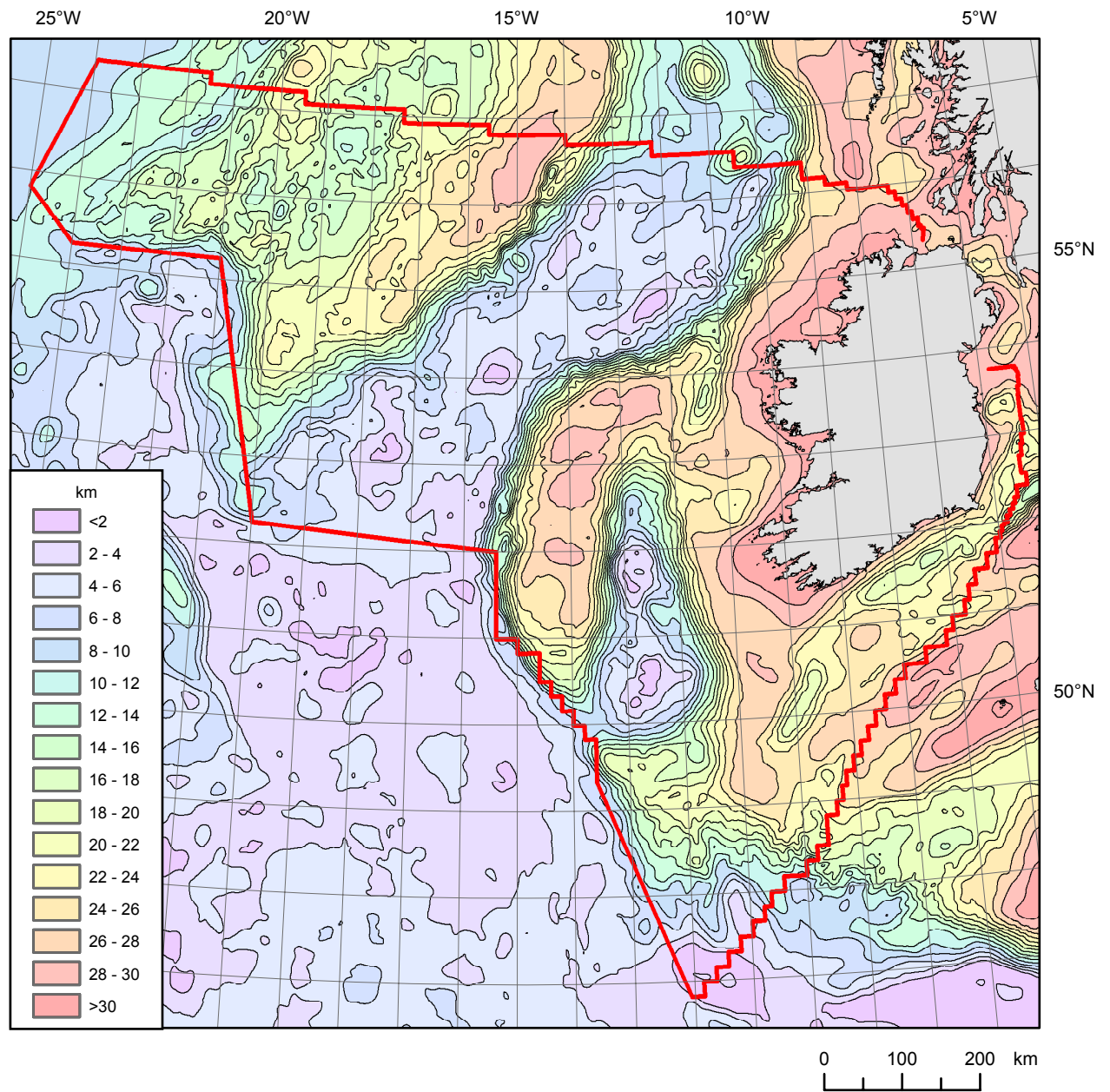


Figure 21 Thickness of crystalline crust in the optimised model.

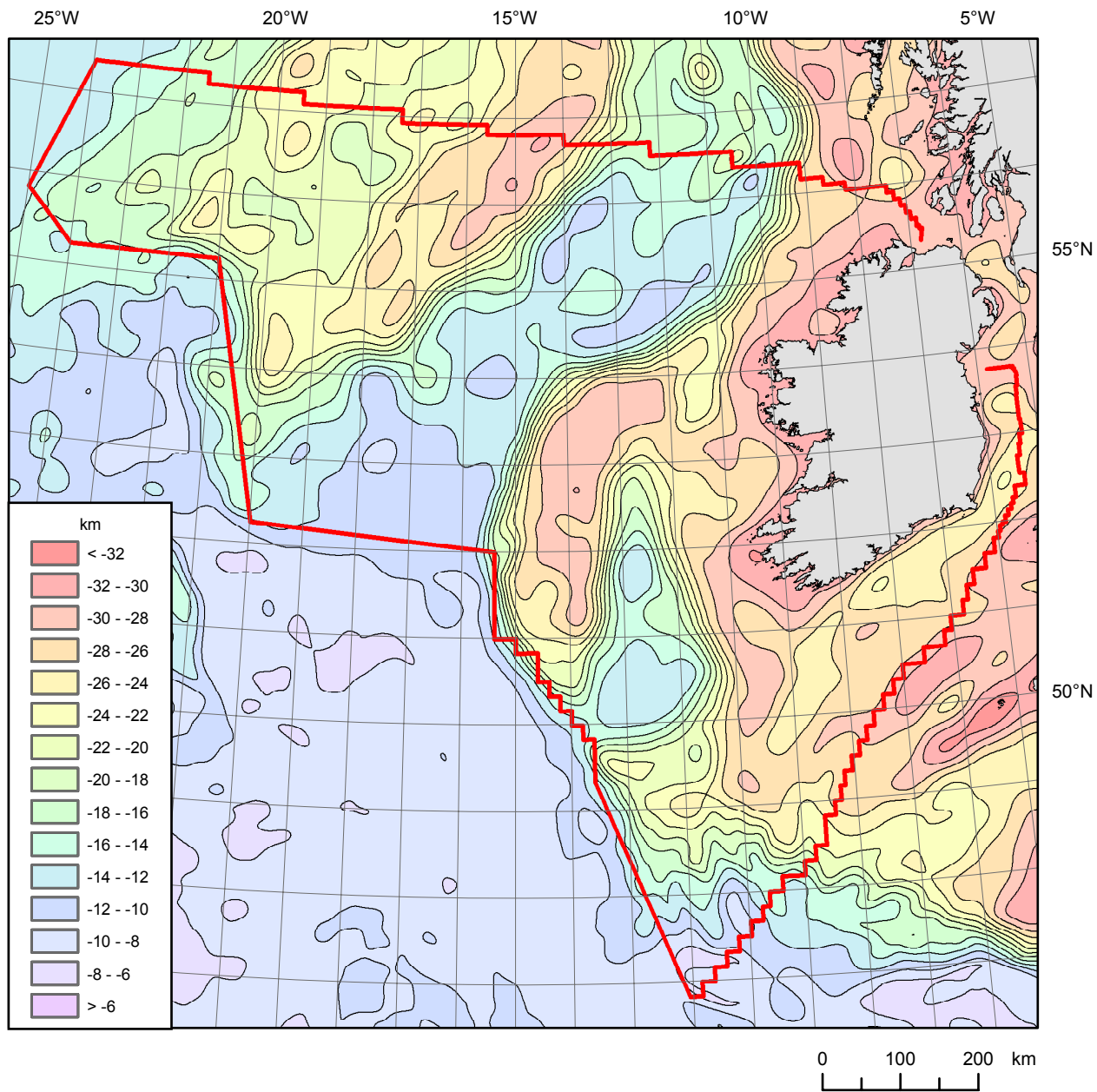


Figure 22 Depth to Moho in the optimised model.

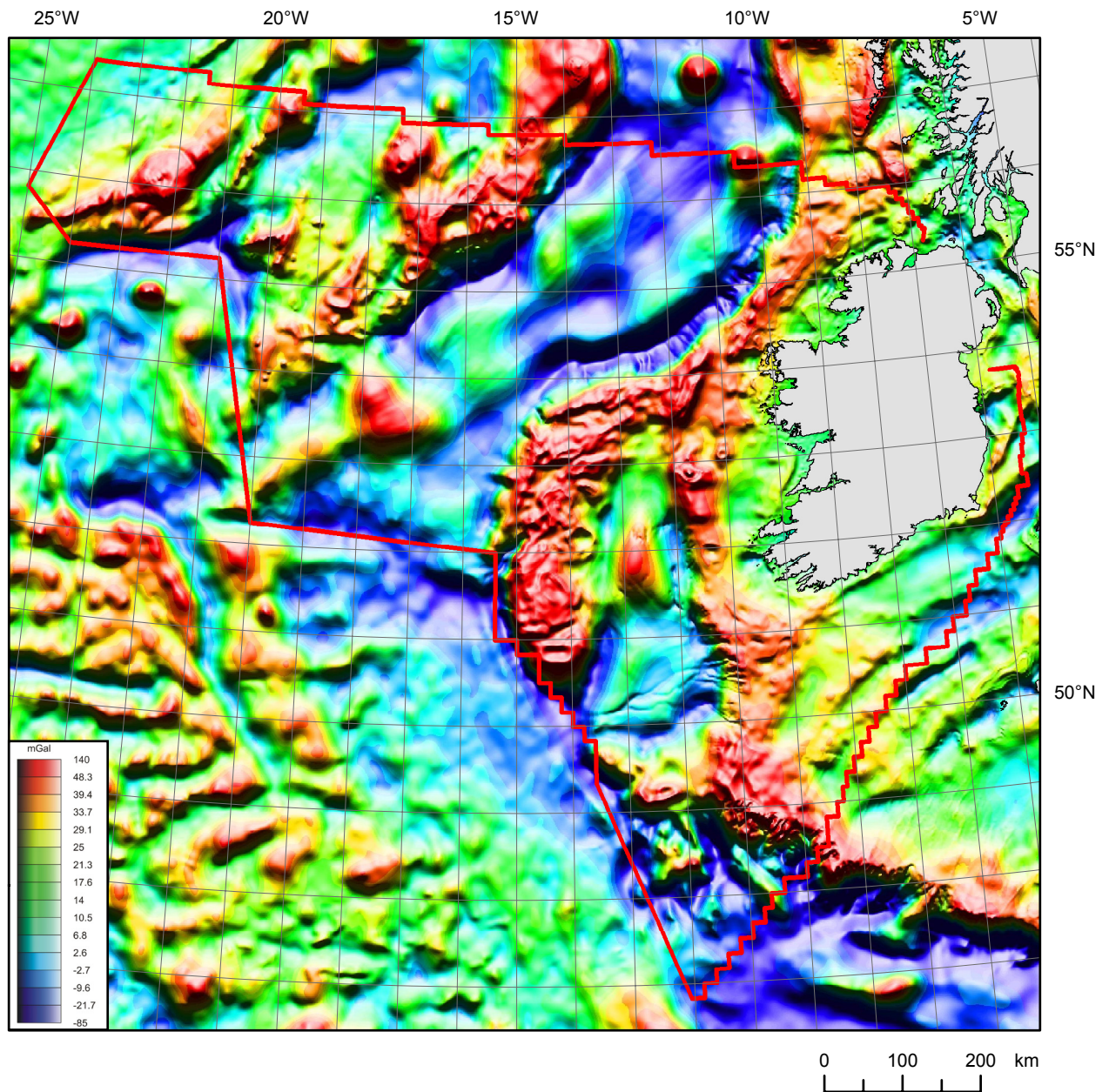


Figure 23 Colour shaded-relief image of the computed free-air gravity anomaly over the optimised model. The imaging parameters are identical to those used in the display of the observed field in Figure 2. Computed values have been shifted by +15 mGal to allow for background field assumed during model optimisation.

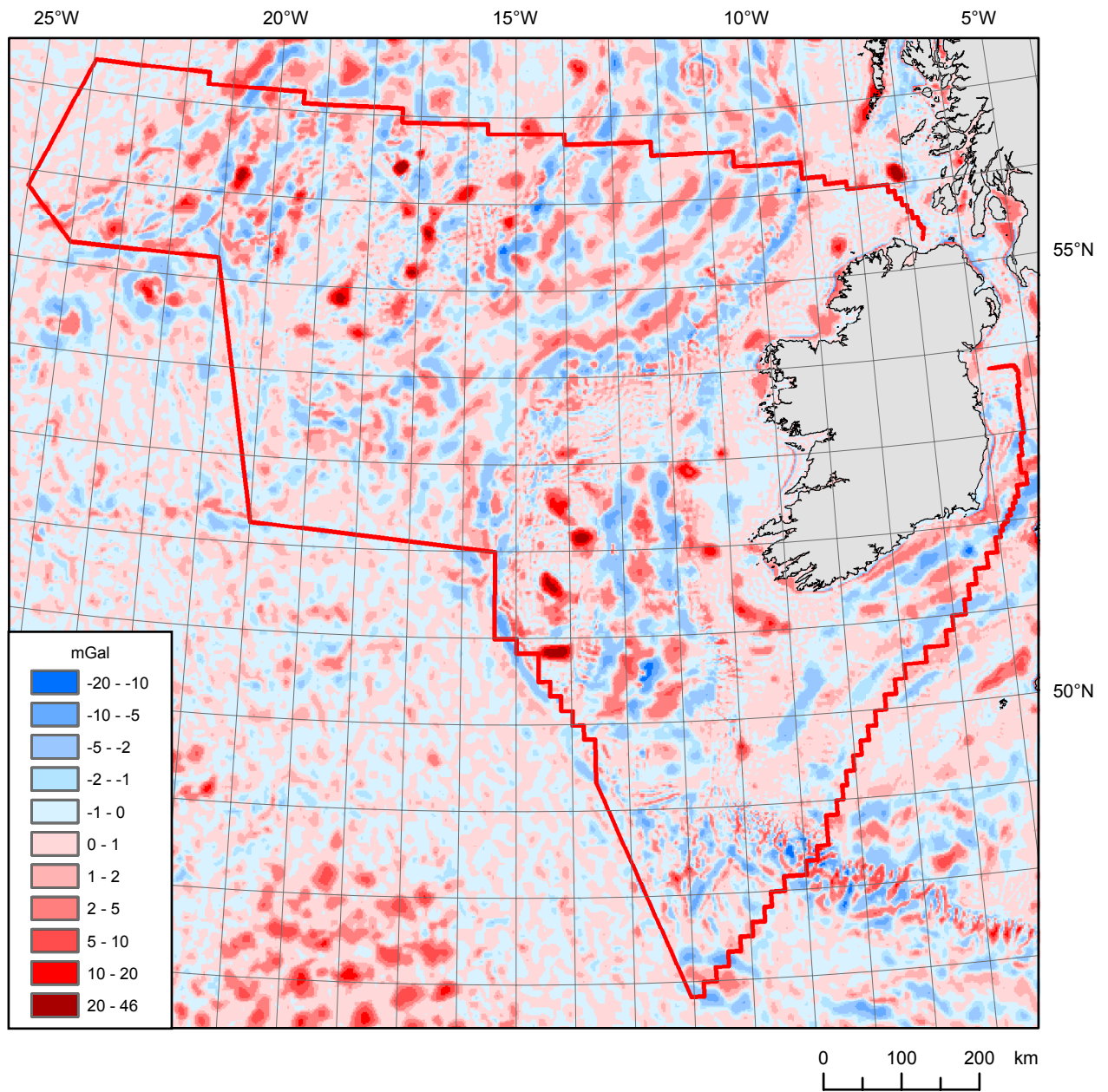


Figure 24 Residual gravity anomaly over the optimised model.

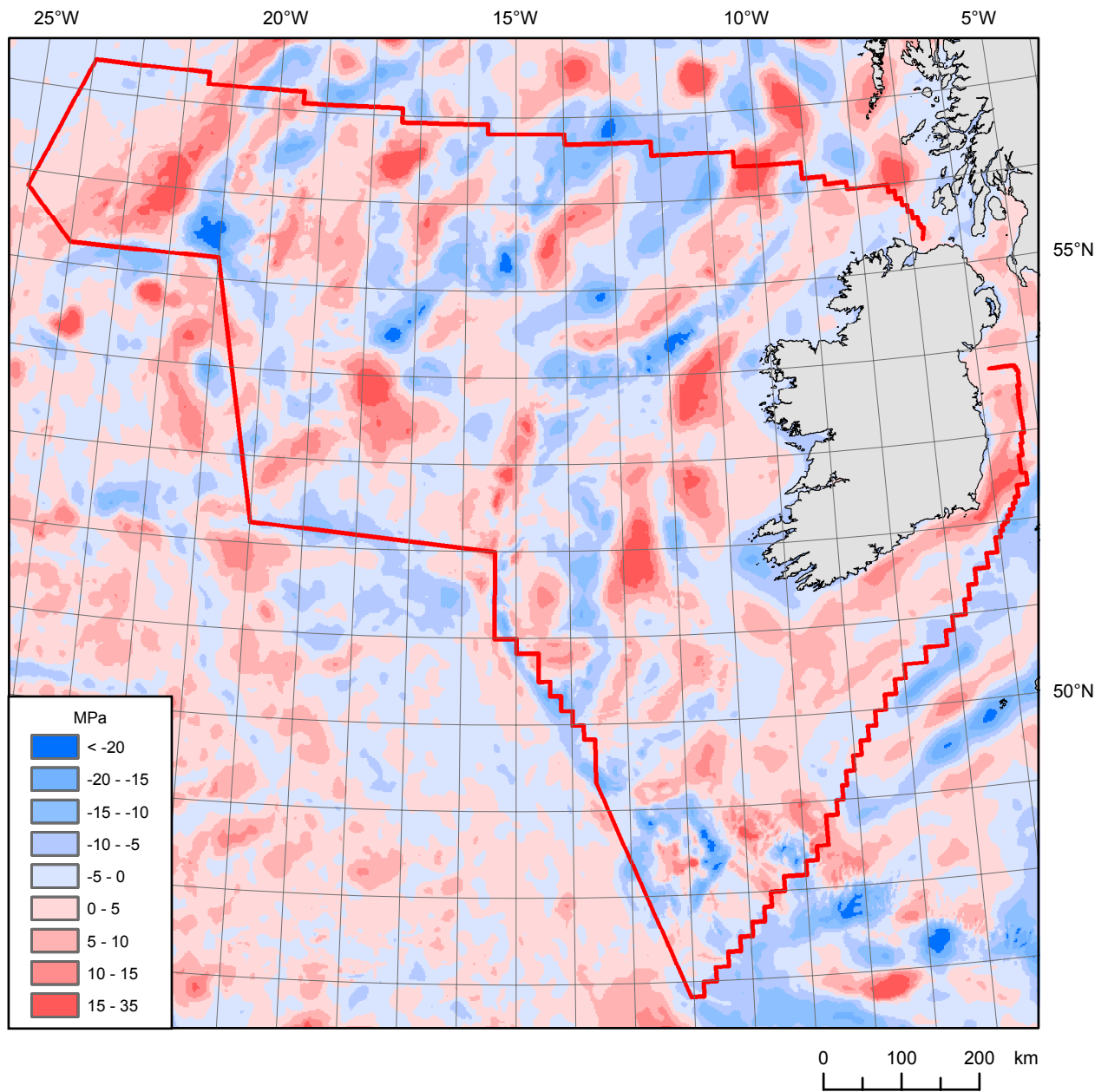


Figure 25 Load anomaly of the optimised model.

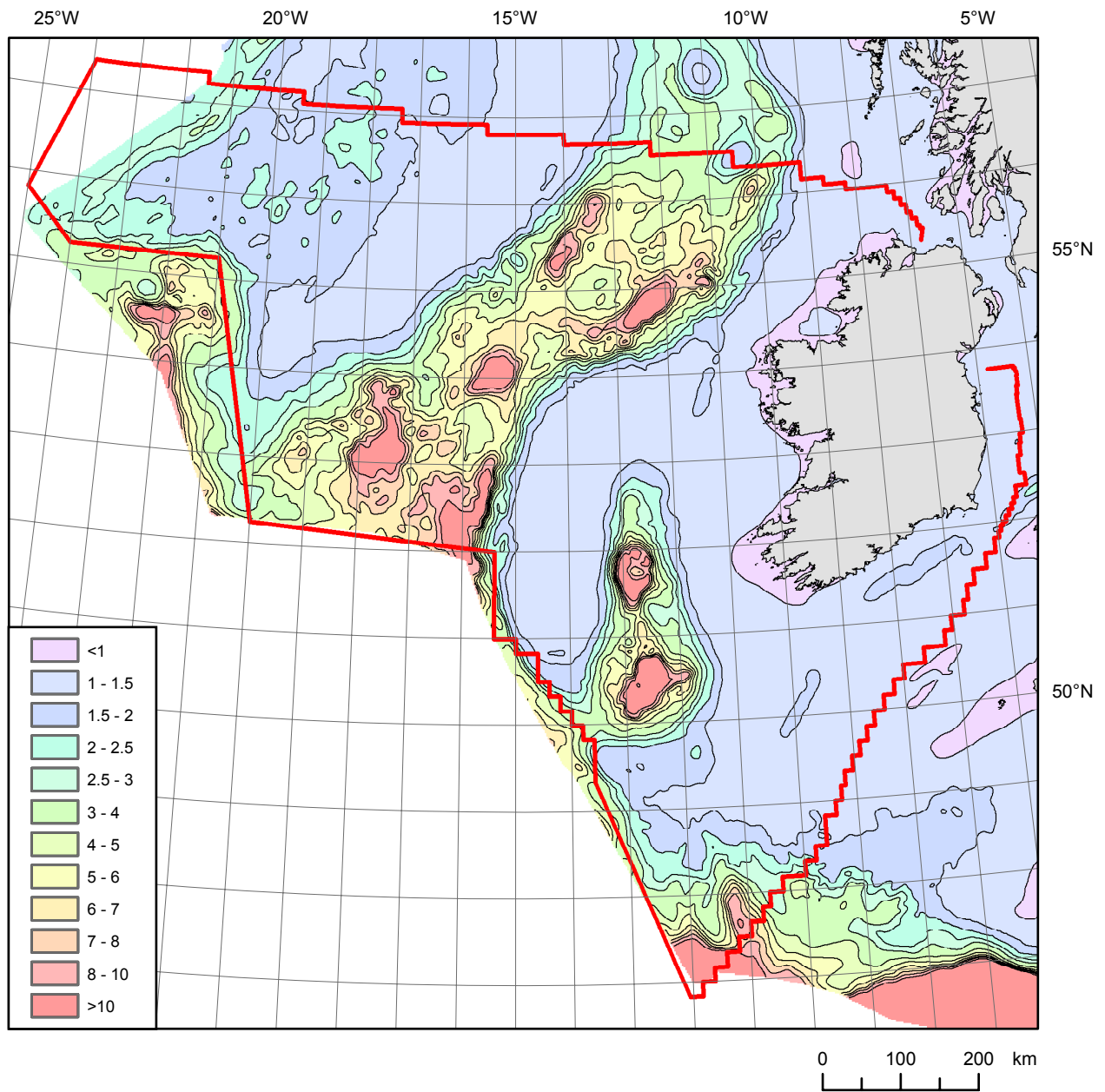


Figure 26 Apparent extension factor of the optimised model. Note that extreme values can arise because of instability in the gravity inversion (see Section 8.2.2 and Figure 30).

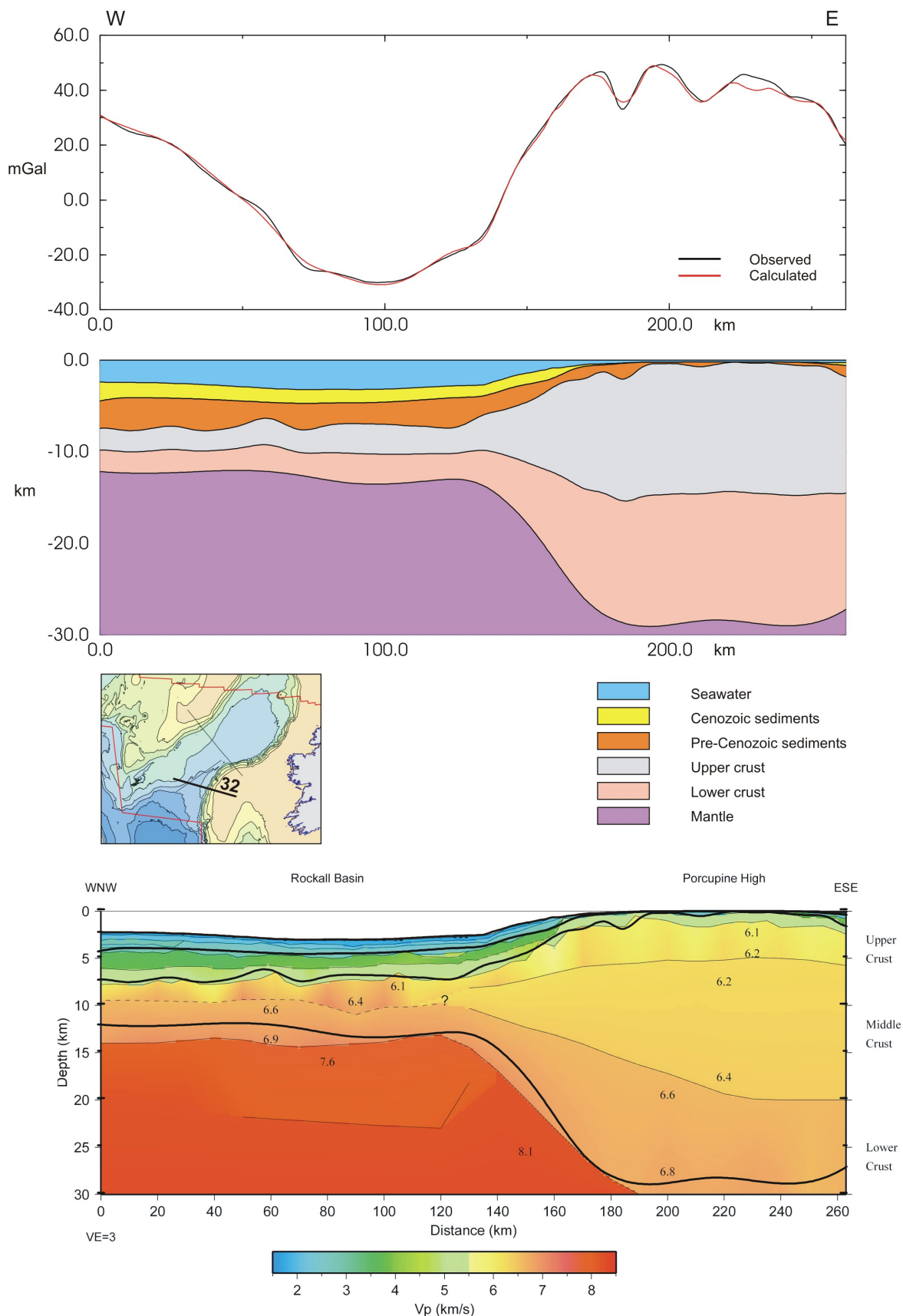


Figure 27 Cross-section through the optimised model along the RAPIDS 32 profile (upper panel). The lower panel shows the main interfaces from the 3D model (sedimentary and Moho) superimposed on the velocity model for this profile of Mackenzie et al. (2002a).

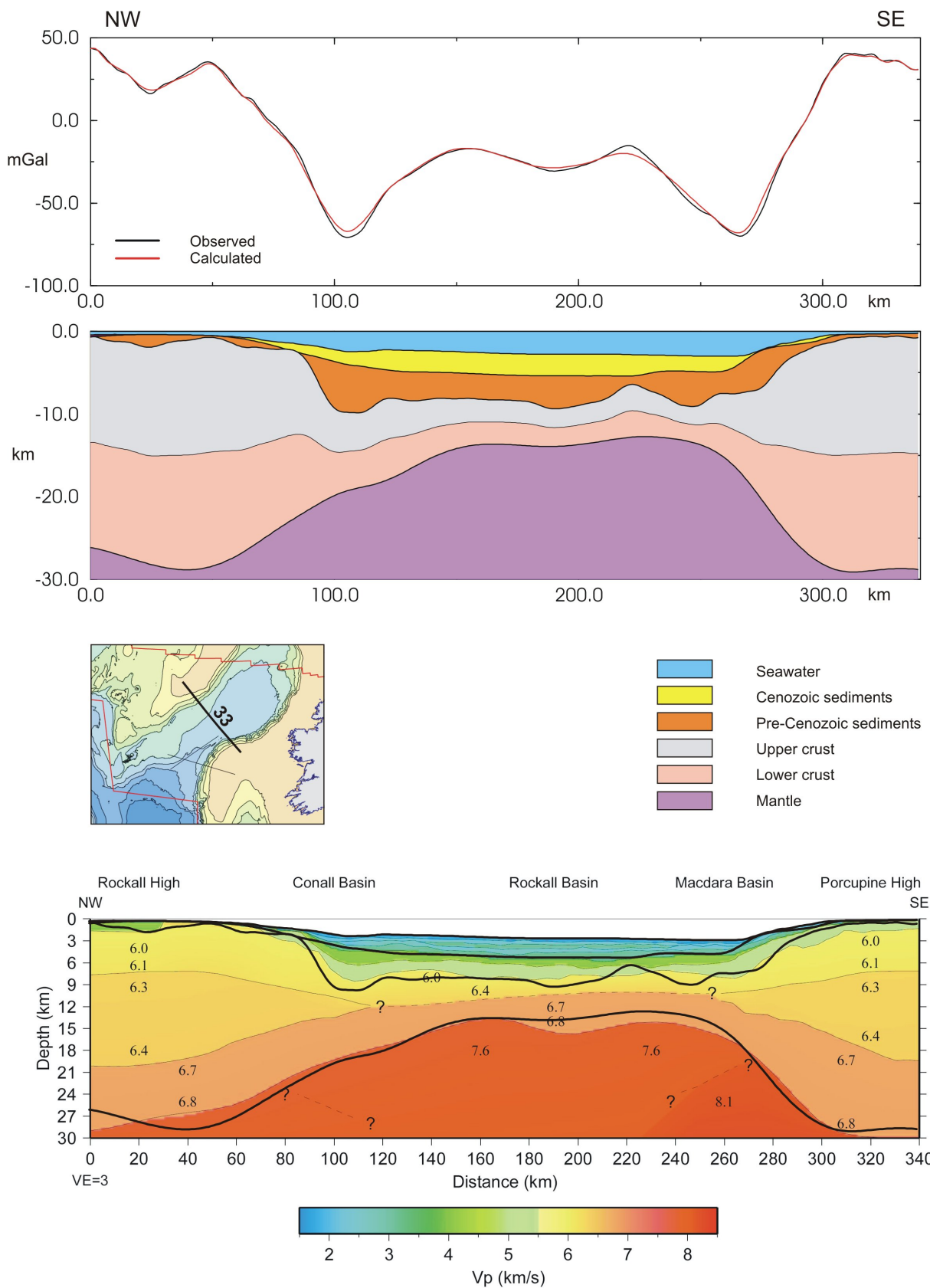


Figure 28 Cross-section through the optimised model along the RAPIDS 33 profile (upper panel). The lower panel shows the main interfaces from the 3D model (sedimentary and Moho) superimposed on the velocity model for this profile of Mackenzie et al. (2002a).

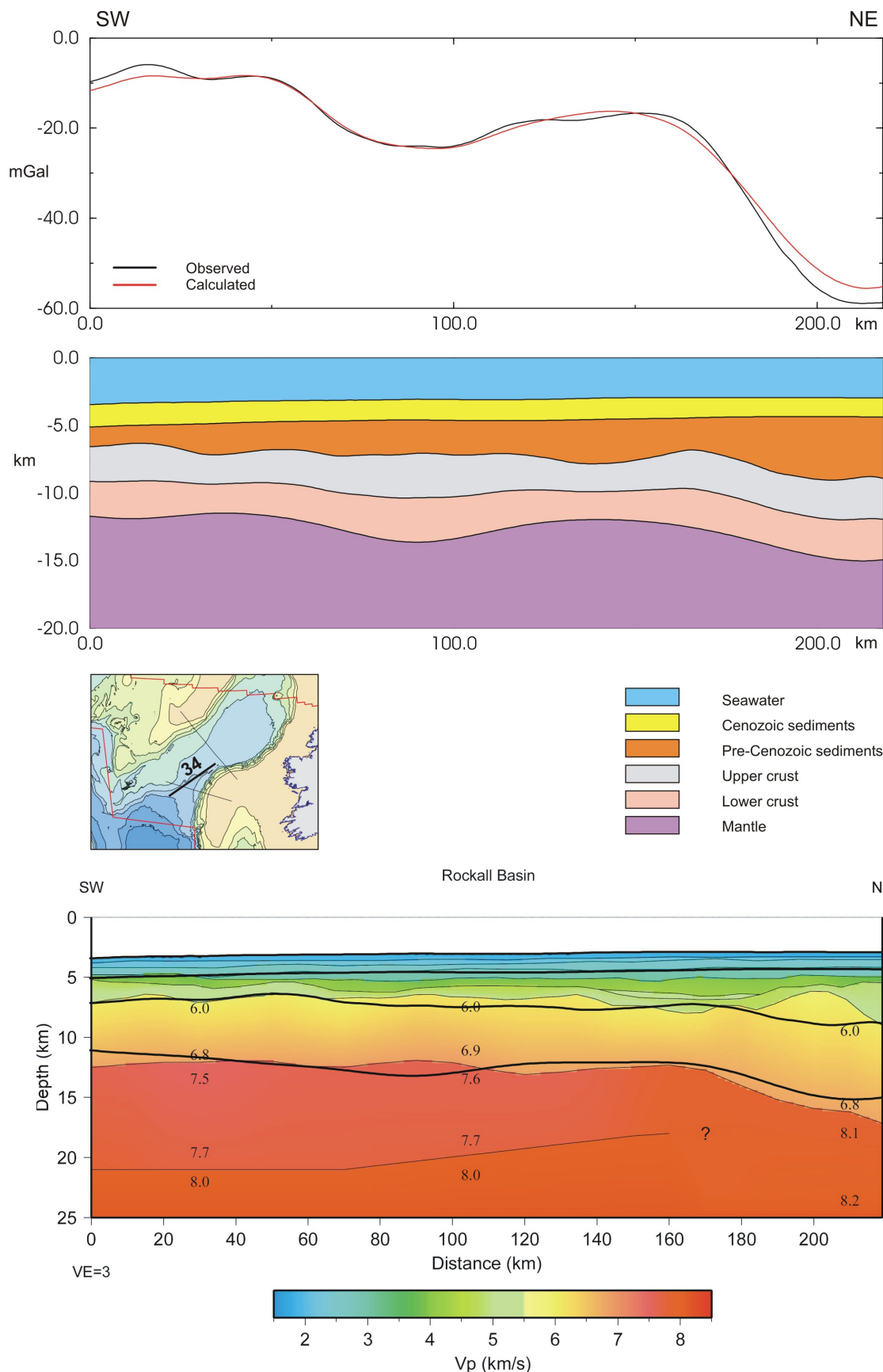


Figure 29 Cross-section through the optimised model along the RAPIDS 34 profile (upper panel). The lower panel shows the main interfaces from the 3D model (sedimentary and Moho) superimposed on the velocity model for this profile of Mackenzie et al. (2002a).

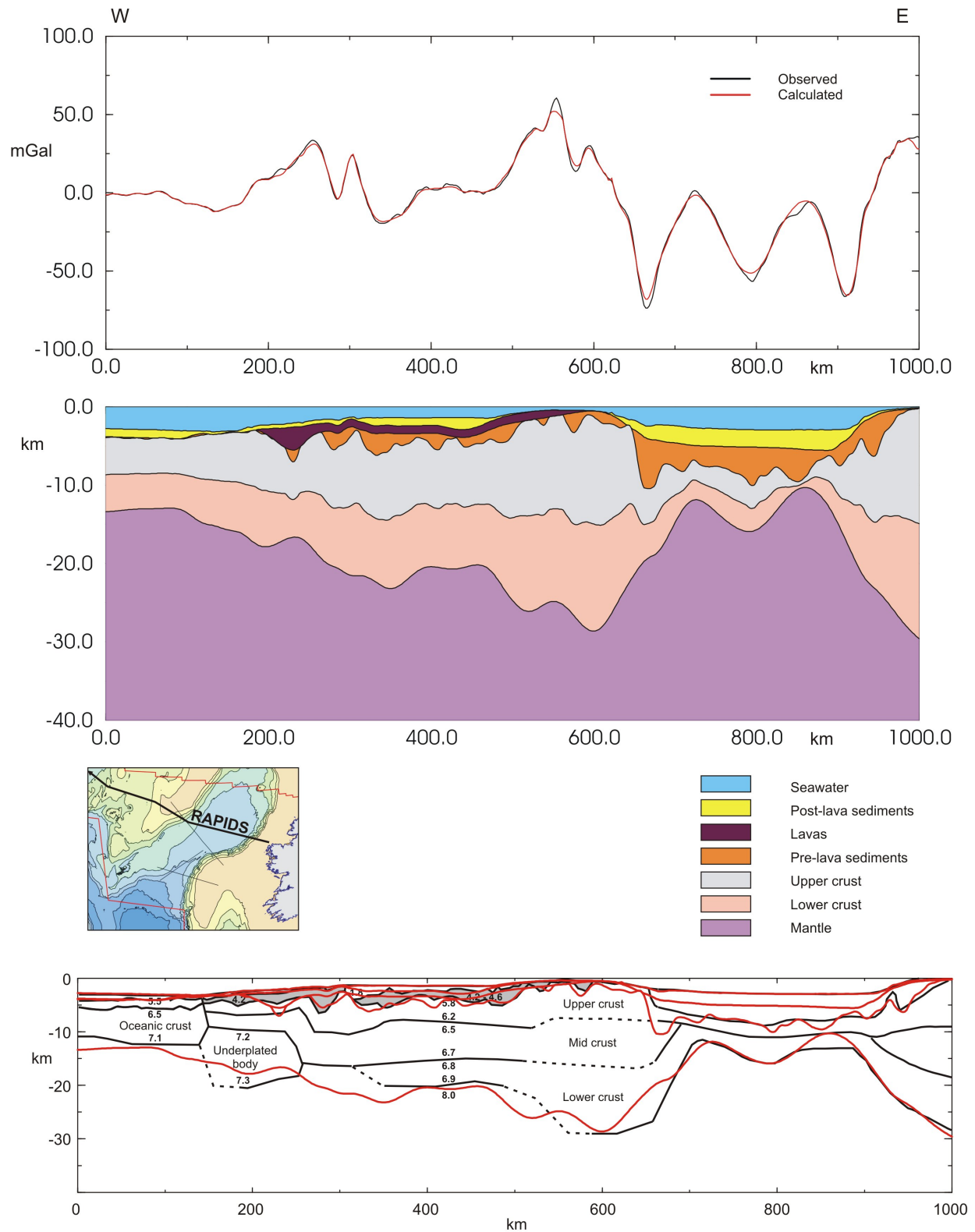


Figure 30 Cross-section through the optimised model along the RAPIDS 1/2 (Transverse) profile (upper panel). The lower panel shows the main interfaces from the 3D model (cover sequence and Moho) in red superimposed on the RAPIDS interpretation of Vogt et al. (1998; western part) and O’Reilly et al (1998; eastern part). The lower sedimentary layer of O’Reilly et al. (1998) is shaded.

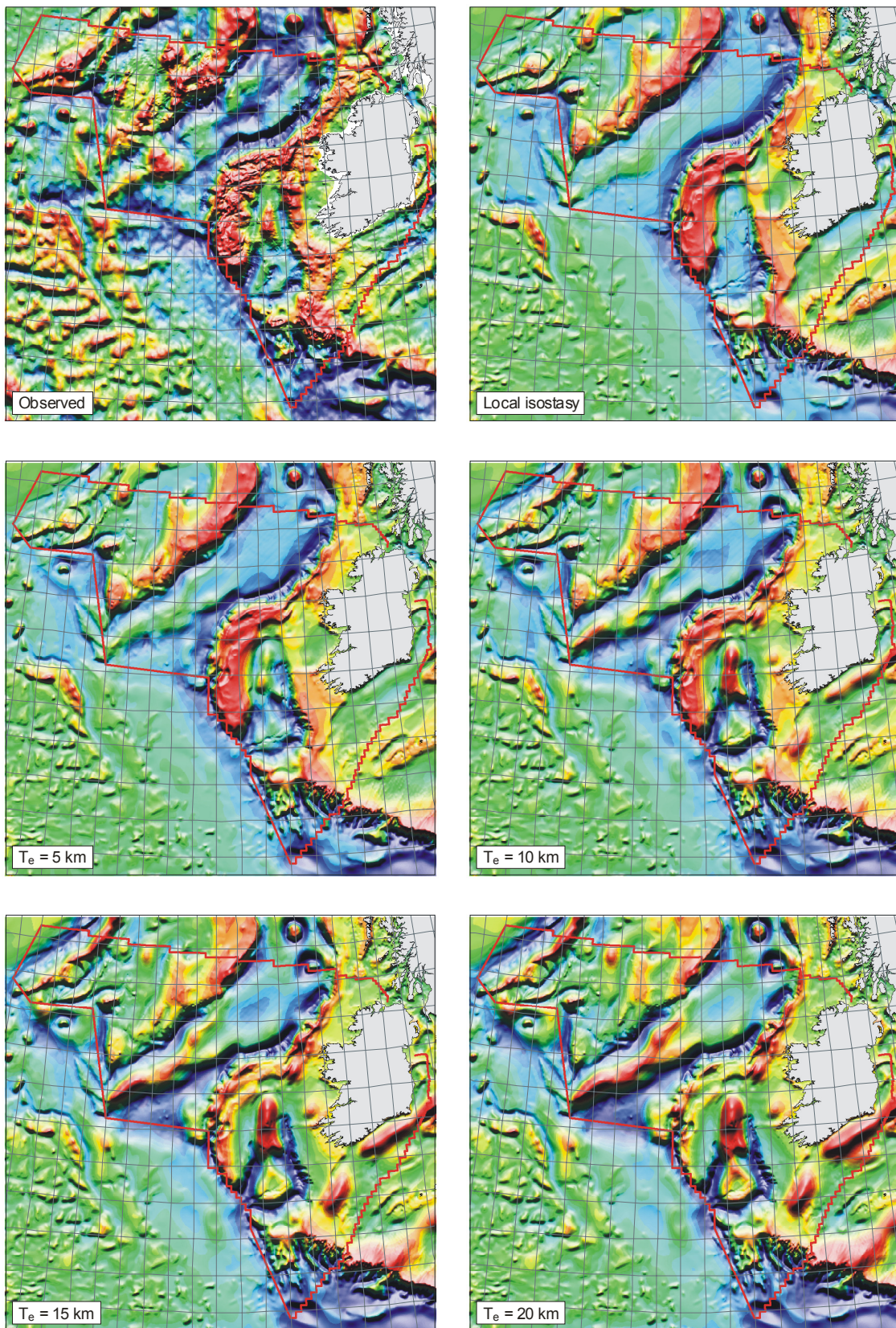


Figure 31 Comparison of computed gravity field over flexural models based on the initial cover sequence model and different assumptions about the strength of the lithosphere. Indicated values of effective elastic thickness are assumed throughout the deposition of the cover sequence.

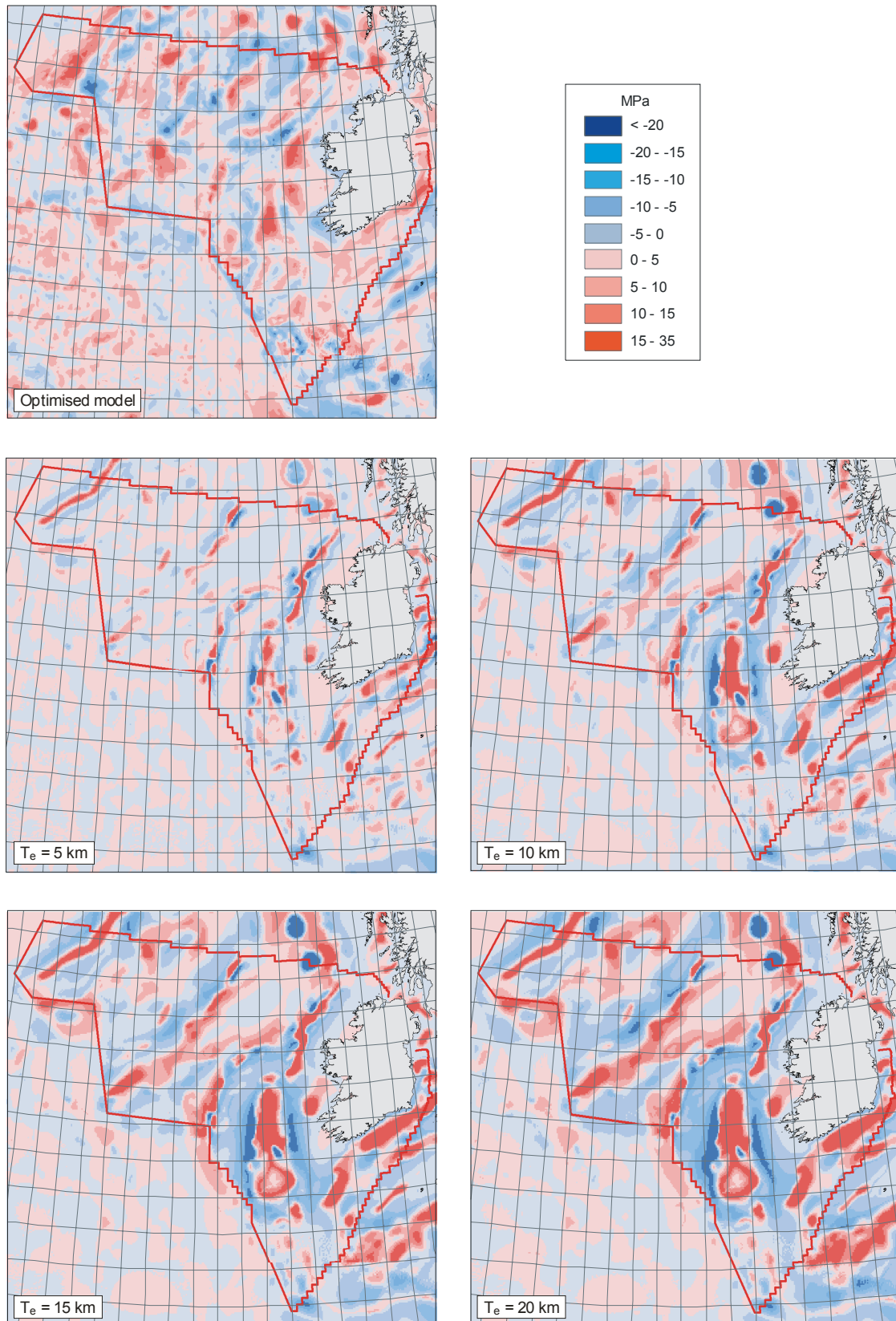


Figure 32 Load anomalies over the optimised model compared with those over the flexural models testing the influence of lithospheric strength during deposition of the cover sequence (Figure 31).

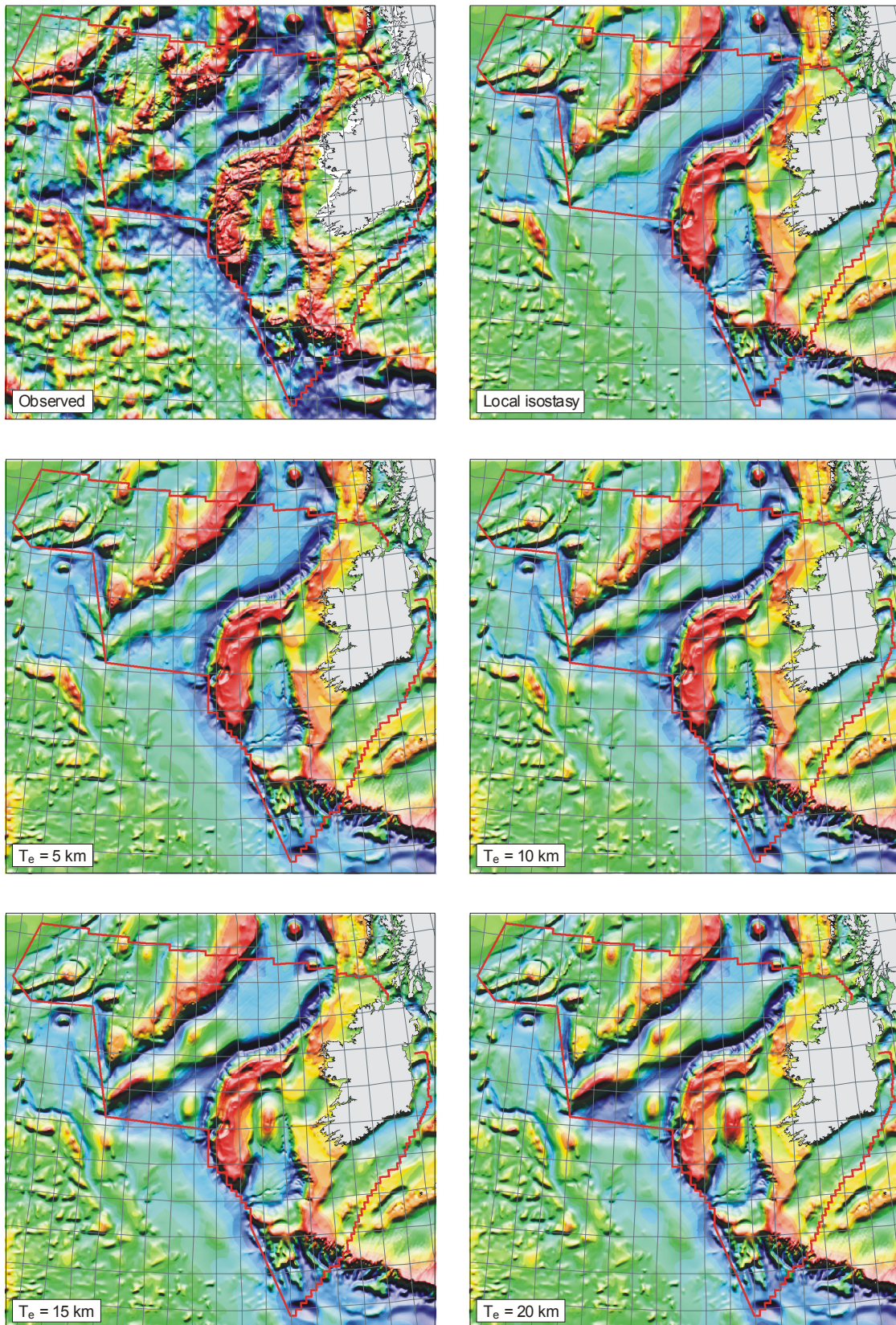


Figure 33 Comparison of observed free-air gravity anomalies with computed fields over flexural models based on the initial cover sequence model. The effective elastic thickness indicated was assumed to apply during deposition of the Cenozoic (post-lava) sedimentary rocks, and the lithosphere was assumed to be weak prior to this. Display parameters as in Figure 2.

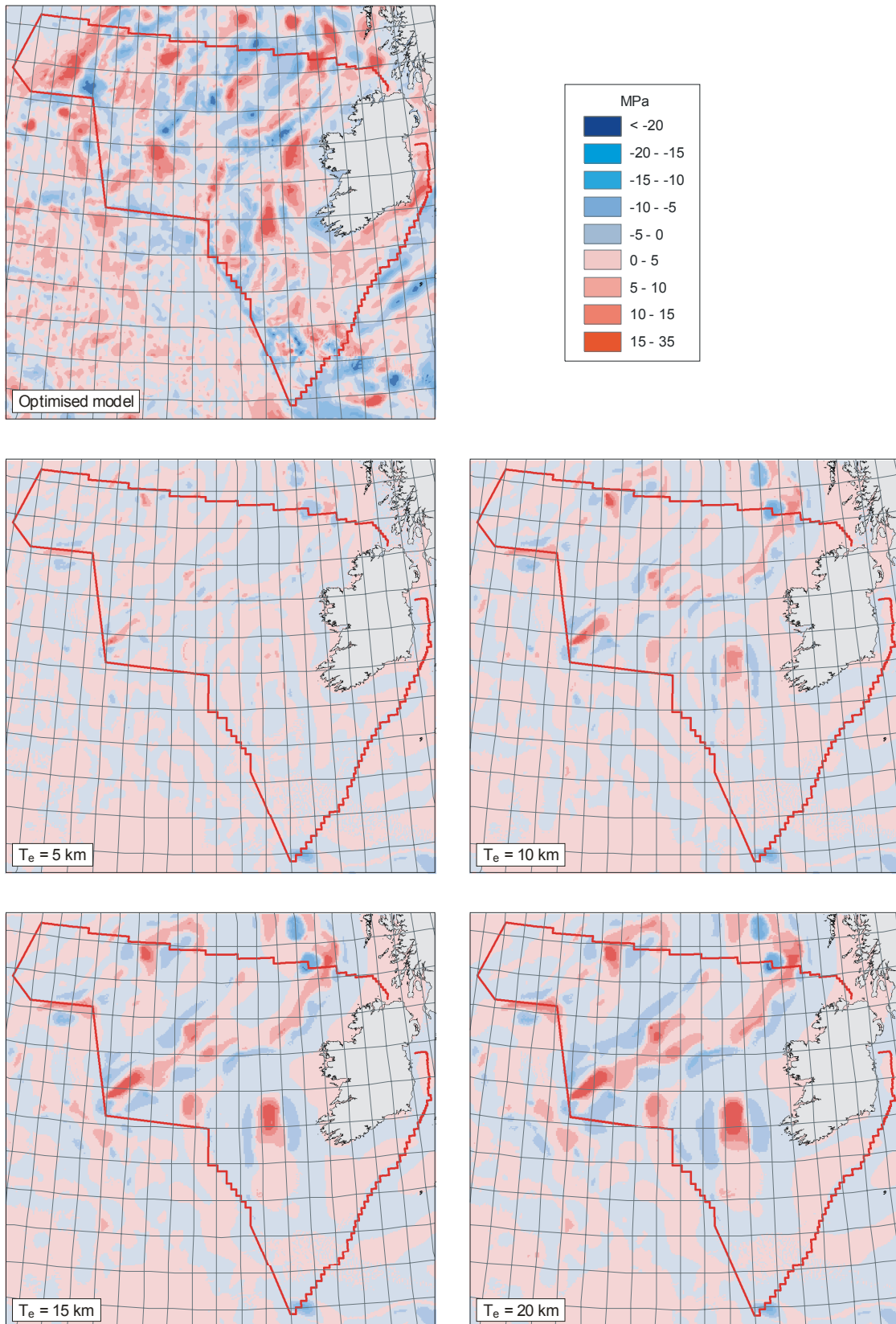


Figure 34 Load anomalies over the optimised model compared with those over the flexural models testing the influence of lithospheric strength during Cenozoic sedimentary loading (Figure 33).

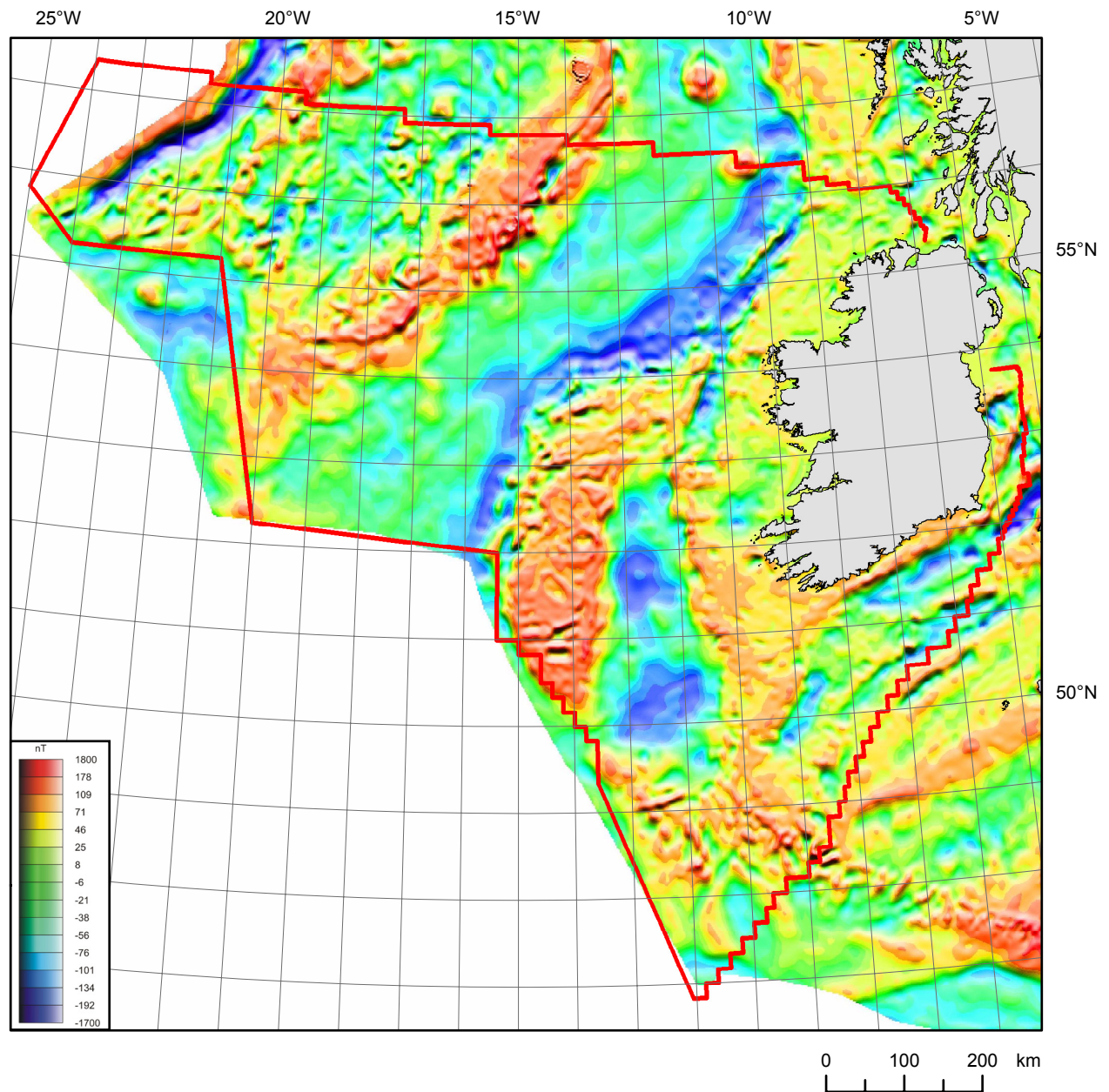


Figure 35 Computed magnetic field over the optimised model assuming the crystalline basement has a uniform induced magnetisation of 1 A/m and the lavas in the Hatton-Rockall area a reversed magnetisation of 3 A/m. The imaging parameters are identical to those used in the display of the observed field in Figure 4.

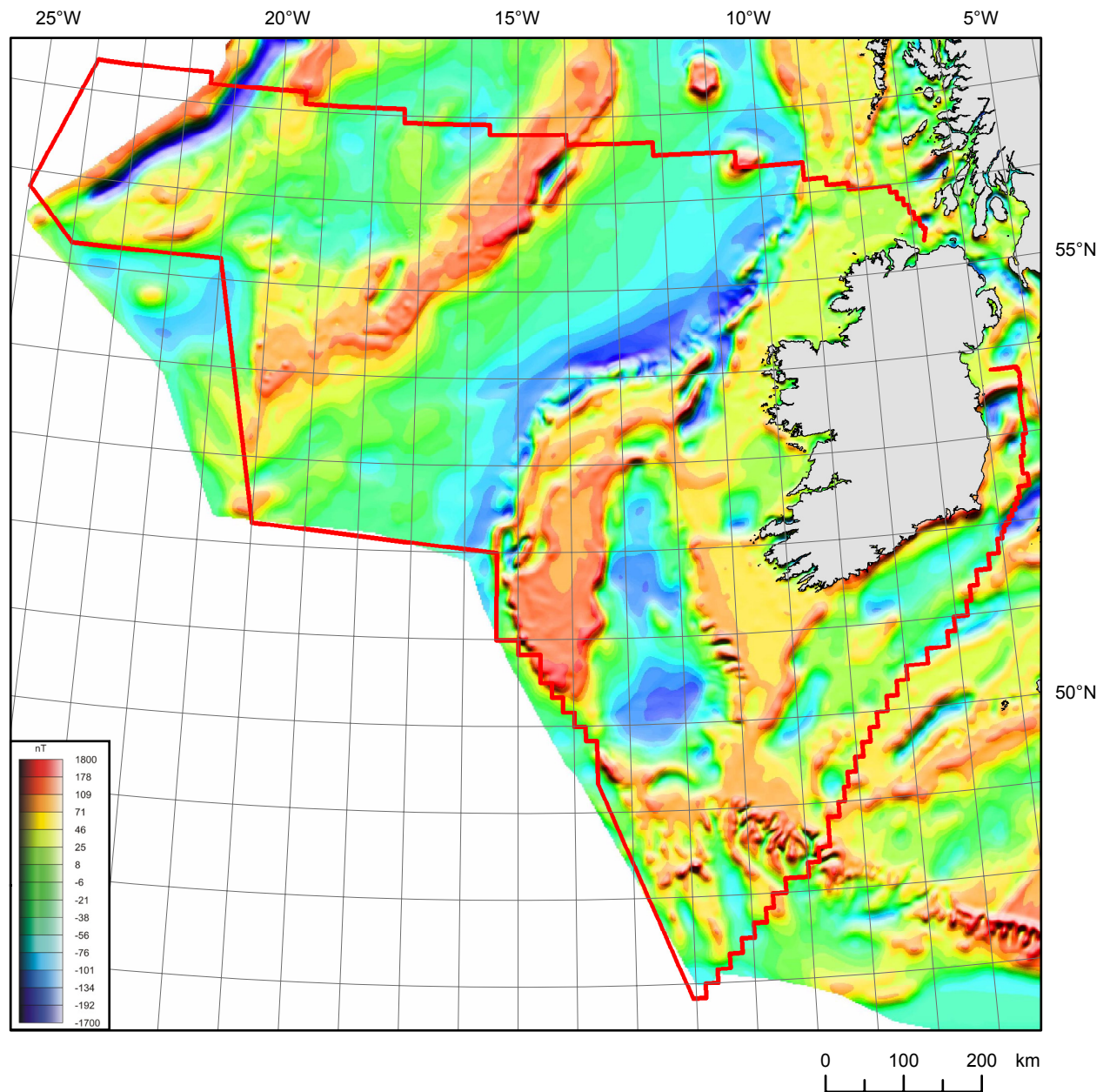


Figure 36 Computed magnetic field over the initial model assuming the crystalline basement has a uniform induced magnetisation of 1 A/m and the lavas in the Hatton-Rockall area a reversed magnetisation of 3 A/m. Model based on initial cover sequence model and crustal thickness based on local isostasy. The imaging parameters are identical to those used in the display of the observed field in Figure 4.

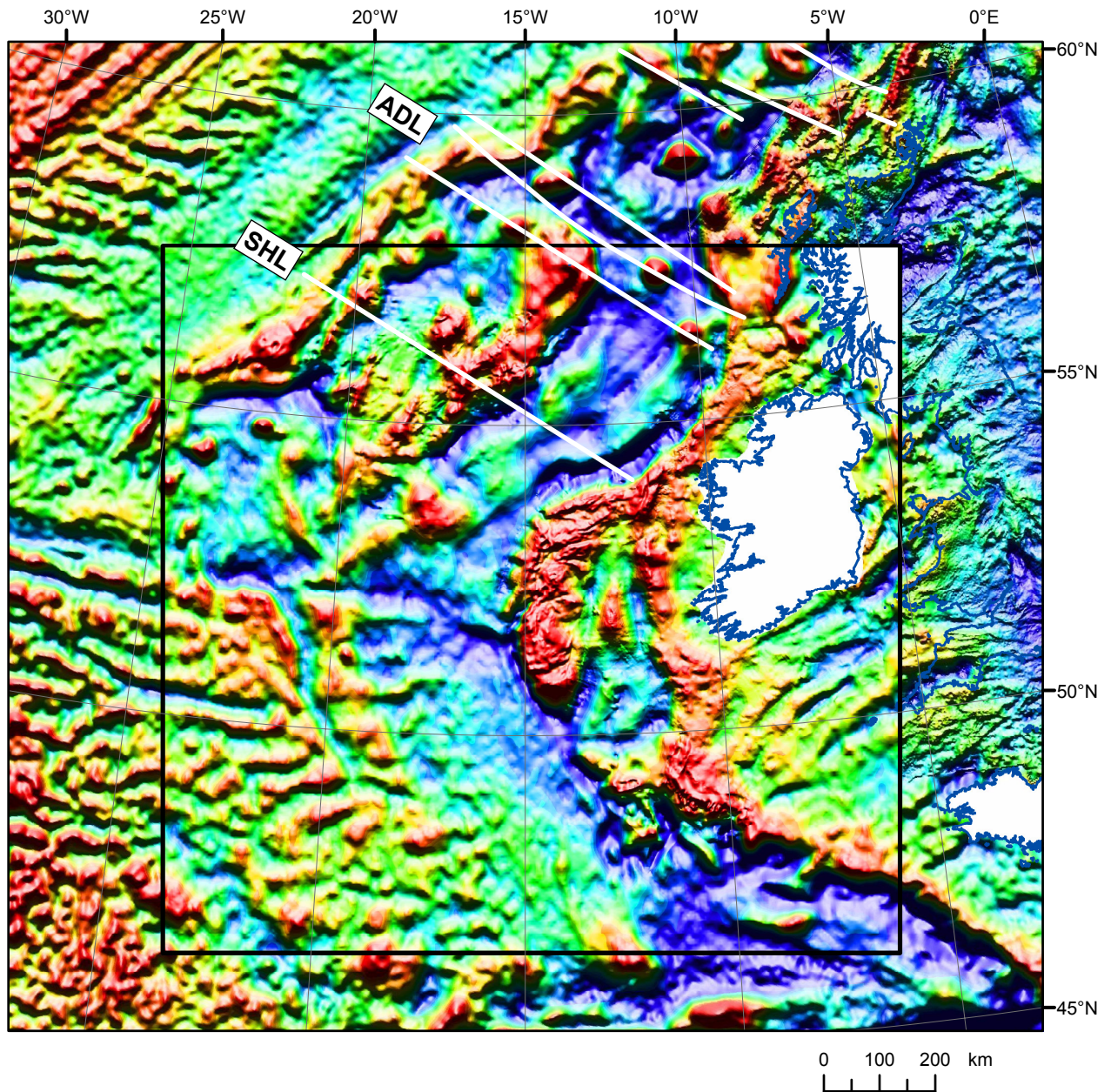


Figure 37 Colour shaded-relief image of free-air gravity anomalies over the north-east Atlantic region. The black rectangle is the IPmmP study area. An IPmmP image has been superimposed on an image based on BGS and open-file data (colour scales differ). Illumination is from the north. White lines are the lineaments of Kimbell et al. (2005): ADL = Anton Dohrn lineament zone; SHL = South Hatton Lineament.

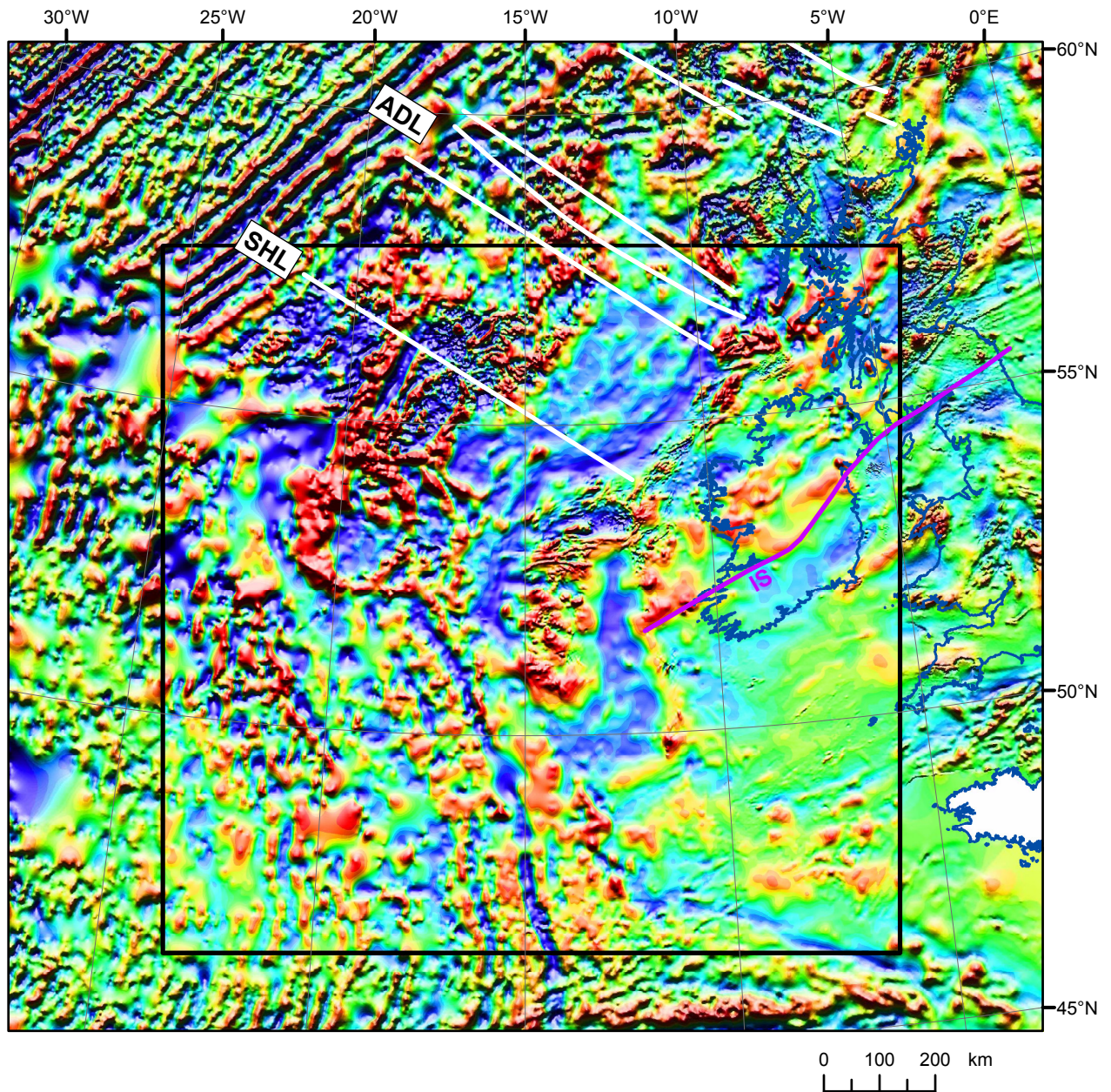


Figure 38 Colour shaded-relief image of total field magnetic anomalies over the north-east Atlantic region. An IPmmP image has been superimposed on an image based on BGS and open-file data (colour scales differ). Illumination is from the north. The black rectangle is the IPmmP study area. White lines are the lineaments of Kimbell et al. (2005): ADL = Anton Dohrn lineament zone; SHL = South Hatton Lineament. The purple line (IS) is the Iapetus Suture, based on the interpretation of Kimbell and Quirk (1999) in the east, and extended westwards on the basis of the magnetic anomaly pattern.

